Single Dissociative Diffraction of Protons in $\sqrt{s} = 8$ TeV Collisions with the ATLAS Experiment

Andrew Geoffrey Foster

Thesis submitted for the degree of Doctor of Philosophy

Particle Physics Group,
School of Physics and Astronomy,
University of Birmingham.

October 27, 2018

ABSTRACT

The first LHC-energy differential cross-sections of the single dissociative diffraction process $pp \to Xp$ are presented as a function of Mandelstam-t, fractional proton energy loss ξ and rapidity gaps within the ATLAS inner detector with a coverage of $|\eta| < 2.5$. The measurement is performed using a data sample collected with the ATLAS detector during a dedicated low luminosity run in 2012 with an integrated luminosity of $1.67\,\text{nb}^{-1}$ and a centre-of-mass energy of $8\,\text{TeV}$. Events are triggered and selected using the ALFA forward detectors, in combination with the ATLAS central detector components, enabling the detection of scattered protons.

The fiducial region is chosen to be $0.016 < |t| < 0.43\,\text{GeV}^2$ and $-4.0 < \log_{10}\xi < -1.6$. The cross-sections within this region are fitted within an interpretation based on Regge theory. The measured B slope within this region is $B = 7.60 \pm 0.31\,\text{GeV}^{-2}$. The ξ dependence of the cross-section is consistent with that expected from soft Pomeron exchange. The total measured cross-section within the fiducial region is $1.59 \pm 0.13\,\text{mb}$. The PYTHIA8 A3 Monte Carlo tune provides a very good description of the shape of the cross-sections but overestimates the integrated cross-section by approximately 60%.

DECLARATION OF AUTHOR'S CONTRIBUTION

The analysis performed within this thesis is built upon the work of thousands of people in the ATLAS and LHC communities who designed, built and continue to operate the experiments that are described in Chapters 2, 3 and 4. The author contributed to this effort by developing the tools and performing the energy calibration of the Level-1 calorimeter trigger, in collaboration with several others, for approximately two years. This work largely involved analysing data from the start of LHC-running in 2015 and 2016 to check that the trigger response was well calibrated to the calorimeter energy response. This is important for triggers that apply specific energy cuts. This work is not documented here, or elsewhere. However, it is built upon many of the principles described in the public document [1]. Additionally, the author was involved with trigger shift work while based at CERN, which entailed monitoring and managing the trigger performance during data-taking.

The introduction of the theoretical understanding of diffraction presented in Chapter 5 represents the author's description of previous work carried out by others, the origins of which are referenced where applicable.

The analysis presented in chapters 6, 7, 8, 9 and 10 is the product of the author's own work except where explicitly specified otherwise. The analysis was performed under the guidance and supervision of Paul Newman. The construction of the analysis framework as well as the early understanding of the data, Monte Carlo sample production and definition of analysis variables was performed in collaboration with two colleagues from McGill and AGH Krakow universities.

ACKNOWLEDGEMENTS

Looking back on my four years as a PhD student, I realise just how much it has provided me. I have spent time living in Geneva (pre-Brexit); attended meetings, schools and conferences in seven countries; made many great friends; made one great girlfriend; satisfied the cliché of having my mind expanded and believe that I have genuinely made a small contribution to the advancement of scientific knowledge. This was only possible with the support and guidance Paul Newman, who has always managed to remain calm and assure me that everything would be ok, even when I was certain it would not be. I have really enjoyed working with you, Paul. In addition, I would like to thank Paul Thompson, Juraj Bracinik and John Wilson for their help along the course of my journey.

The first half of analysis I present was performed in collaboration with Grzegorz and Ana from Krakow and McGill, respectively. Your help was crucial to the success of this analysis and it was always fun to bounce around ideas with you. I am highly impressed that our long-distance collaboration worked so well, but I particularly enjoyed our meet-ups at CERN. A special thanks to Grzegorz for inviting me to Krakow and showing me good Pierogi.

I owe a great deal to my fellow students at Birmingham who have made coming into the office every day an enjoyable experience even when the going was at its toughest. In particular I would like to thank Andy C, Richard, Alasdair, Jamés and Tim for putting in a full four year shift and still being friends with me after the disrespectfully good fantasy football season that I had in 16/17. I will miss our weekly Dilshad and Goose trips and our seemingly annual Stag Dos[1]. I look forward to cashing in on the many premium beers and hooches that you all owe me. I would also like to thank all the other students for the in-jokes such as danger juice, a-kneeling and Playmobil®. Going into my PhD, I couldn't have known that I would

[1]Made possible by Sam, Zebra and the city of Manchester.

be part of a ‘golden-generation’ football team twice crowned national champions for particle physics 5-a-side. To future students, I remind them that you’re only as good as your latest Bubble Chambers tournament.

I am lucky enough to still be close friends with many of the people that I met during my undergraduate degree, including the wonderfully named ‘Pints Ahoy’ and the ‘Loose Boys’. You know me better that I know myself - you knew what I needed in Ios when I informed you that I didn’t actually want to go out. The equally grandiosely named ‘La Clique’ made the year living in Geneva, which frequently involved cycling round picturesque vineyards then coming home and sampling some delightful box-wine, one of my best.

I would like to thank Abby for putting up with me even when I request ‘just one more’ explanation of unfolding at 23:55 on a Sunday. I wasn’t the easiest to be around when PhD stress was peaking and you always managed to make me feel better. I love you.

Lastly, it need not be said, but I owe so much to my family. You have always supported and inspired me to be the best me I can be. Mum and Dad, thank you for all the Saturday morning drives to swimming club, for the 4pm hot cross buns and for tolerating my pointless games. Mark, you are the kindest person I know. From showing me how to get out of the starting room on Pokemon Blue when I was eight years old to adding at least one new questionable rule to ‘goal’ every time I see you, you have always helped guide me. Grandad, thank you for always encouraging me to make the most out of every opportunity and to keep on exploring. Without you all there is no thesis.

Vaya con Dios - Johnny Utah, 1991.

Contents

List of Figures

DEFINITIONS OF ACRONYMS

AFP 'ATLAS Forward Proton' 30

ALFA 'Absolute Luminosity For ATLAS' 28

ALICE 'A Large Ion Collider Experiment' 9

ATLAS 'A Toroidal LHC ApparatuS' 9

BSM Beyond the Standard Model 9

CD Central Diffraction 47

CERN 'the European Organization for Nuclear Research' 2

CMS 'Compact Muon Solenoid' 9

CNI Coulomb Nuclear Interference 46

CP Charge-Parity 10

CSC Cathode Strip Chamber 21

CTP Central Trigger Processor . . . 23

CT-PPS CMS-TOTEM Precision Proton Spectrometer . . . 34

DD Double dissociative Diffraction . . . 47

DL Donnachie and Landshoff . . . 55

DPDF Diffractive Parton Density Function . . . 56

DPE Double Pomeron Exchange . . . 47

EC End-Cap . . . 11

EF 'Event Filter' . . . 23

EW Electro-Weak . . . 37

GEM Gas Electron Multiplier . . . 35

ID 'Inner Detector' . . . 14

IP Interaction Point . . . 6

ISR 'Intersecting Storage Rings' . . . 29

L1 'Level-1' . . . 23

L2 'Level-2' . . . 23

LO Leading Order . . . 56

LAr Liquid Argon . . . 19

LEIR 'Low Energy Ion Ring' . . . 6

LEP 'Large Electron Positron collider' . . . 6

LHC 'Large Hadron Collider' . . . 2

LHCb 'LHC beauty' . . . 10

LS 'Long Shutdown' . . . 8

LUCID 'LUminosity measurement using Cherenkov Integrating Detector' . . . 28

MAPMT Multi-Anode Photo-Multiplier Tube . . . 29

MB Minimum Bias . . . 62

MBTS 'Minimum-Bias Trigger Scintillator' . . . 22

MC Monte Carlo . . . 27

MD 'Main Detector' . . . 29

MDT Monitored Drift Tube . . . 21

MET Missing Transverse Momentum . . . 11

ND Non-Diffractive . . . 47

OB 'Overlay Background' . . . 57

OD 'Overlap Detector' . . . 29

PDF Parton Distribution Function . . . 53

PMT Photo-Multiplier Tube 22

PS 'Proton Synchrotron' 5

PSB 'Proton Synchrotron Booster' 5

PV Primary Vertex 75

QCD Quantum Chromodynamics 26

QFT Quantum Field Theory 1

RF Radio Frequency 5

ROD ReadOut Driver 24

RP Roman Pot 29

RPC Resistive Plate Chamber 21

SCT 'SemiConductor Tracker' 15

SD Single dissociative Diffraction 47

SM Standard Model 11

SPS 'Super Proton Synchrotron' 6

SS Schuler and Sjöstrand 55

TGC Thin Gap Chamber 21

ToE Theory of Everything 1

TOTEM 'TOTal Elastic and diffractive cross section Measurement' 28

TRT Transition Radiation Tracker 15

UE Underlying Event 63

vdM van der Meer 7

ZDC 'Zero-Degree Calorimeter' 28

CHAPTER 1

INTRODUCTION

Physics is often compartmentalised into different fields, implying some nature of discreetness. Far from being fundamental, this separation of physics stems from the sensitivity of different machines used to perform measurements at varying length scales combined with mankind's inability to reconcile the understanding of the very large with the very small. At the large end of the length scale, astrophysics and cosmology reign supreme, providing an understanding of the universe using telescopes and explaining observations in the language of general relativity. Conversely, at very small scales, particle physics is the relevant field, with particle colliders being our 'telescopes' and Quantum Field Theories (QFTs) providing the theoretical description. Both physics branches offer clues towards a greater, more complete, understanding that has thus far evaded us. The ability to describe the big, the small, and the in-between, in one theoretical framework is often referred to as a Theory of Everything (ToE). Without a ToE, it is the responsibility of physicists operating at all length scales to provide measurements and probe theoretical predictions, as

guided by the scientific method.

Situated at 'the European Organization for Nuclear Research' (CERN), the 'Large Hadron Collider' (LHC) is the world's largest and highest energy particle physics accelerator. The LHC predominantly collides beams of protons. Approximately half of proton-proton collisions at current LHC energies are understood as interactions between the constituent particles of the non-fundamental protons (quarks and gluons). Such interactions are typically understood to a very high precision within QFTs. The other half of collisions, termed 'elastic' and 'diffractive', are best understood as interactions between protons rather than between their constituents. Approximately a quarter of proton-proton collisions are diffractive although this fraction is not well known and could easily be anywhere between 20% and 30%, motivating a better understanding of such processes at a fundamental level. A more physical motivation for the study of such collisions is to improve the understanding of the total rate at which protons interact with each other, which has wide ranging implications from the understanding of cosmic ray showering to understanding the rate of background interactions in other physics analyses. The analysis presented within this thesis investigates the single diffractive dissociation process, $pp \to pX$, that constitutes approximately half of all these diffractive interactions.

This document is structured as follows:

- Chapters 2, 3 and 4 provide details on the experimental setup used in the analysis that forms the bulk of this thesis. Chapter 2 describes the LHC: the accelerator used to produce the proton-proton collisions. Chapters 3 and 4 provide overviews of the ATLAS detector and the ALFA subdetectors used to select and collect data.

- Chapter 5 places diffraction within the Standard Model of particle physics and introduces the theoretical framework of Regge theory, within which diffraction is best described.

- Chapters 6, 7, 8, 9 and 10 describe the analysis presented in this thesis. Chap-

ter 6 details the analysis strategy and the collection and selection of the data. Chapter 7 explains the efficiency corrections applied to account for the detection process. Chapter 8 discribes how the background sources still present after analysis selection are constrained. Chapter 9 explains how the data are corrected back to a cross-section and the evaluation of the sources of systematic uncertainty on the measurements. In chapter 10, the cross-sections are presented and fits are performed to the data.

- A summary of the work presented in this thesis is provided in Chapter 11. The outlook and impact of the measurement is also discussed.

CHAPTER 2

CERN and the Large Hadron Collider

The 'Large Hadron Collider' (LHC) is located at 'the European Organization for Nuclear Research' (CERN), an international scientific organisation promoting worldwide collaboration on the study of the fundamental questions in physics. Founded in 1954 and located in a suburb of Geneva, Switzerland, CERN has played a vital role in the advancement of our understanding of particle physics and lists the discovery of the W, Z and Higgs bosons among its many achievements [2, 3, 4, 5, 6].

2.1 CERN Accelerator Complex

CERN's current flagship facility is the LHC and the detectors situated at its interaction points. Several of the previous accelerators at CERN, once responsible for producing collisions at the forefront of high-energy physics, have been re-purposed as the pre-accelerators for the LHC. These are displayed in Figure 2.1.

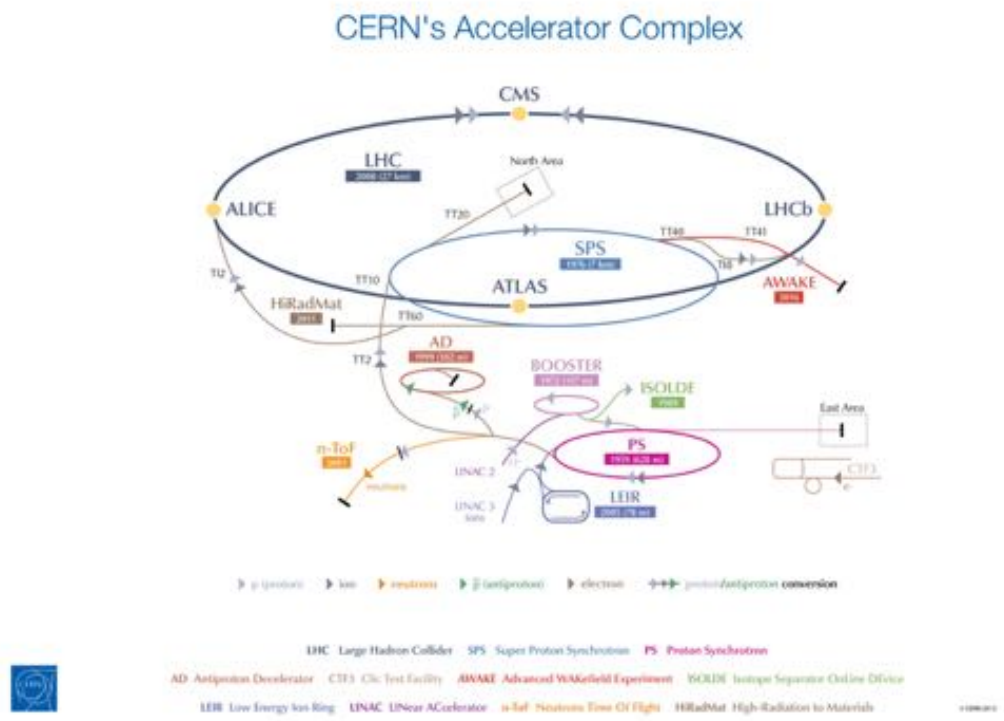

Figure 2.1: The LHC accelerator chain from a hydrogen gas bottle to the LHC. Taken from [7].

At the LHC, proton-proton, proton-lead and lead-lead collisions are performed. The protons for these collisions are sourced from bottles of hydrogen gas. The electrons are removed from the hydrogen atoms to produce the protons that will undergo collision in the LHC.

To achieve the required injection energy for the LHC, the protons are passed through the accelerator chain, starting with Linac 2. Linac 2 uses Radio Frequency (RF) cavities to alternatively charge cylindrical conductors positively and negatively behind and in front of the protons, resulting in attraction from the forward direction and repulsion from behind the protons causing an acceleration; this is the principal means of forward acceleration used in all of the CERN accellerator complex. The protons exit Linac 2 with an energy of 50 MeV. The proton beam is then passed into the 'Proton Synchrotron' (PS) via the 'Proton Synchrotron Booster' (PSB), which accelerates the protons to an energy of 1.4 GeV, increasing the rate at which the PS can accept protons by a factor of 100 [8]. The PS has a circumference of

628 metres and increases the energy of the proton beam to 25 GeV by continually passing it through RF cavities using 100 dipole magnets to confine the protons to the ring using the same principles as those used in the LHC. In 1959 the PS was the world's highest energy particle accelerator. The PS injects into the 'Super Proton Synchrotron' (SPS) which is a 7 km circumference ring responsible for the discovery of the W and Z bosons in 1983 while colliding protons with anti-protons. The SPS accelerates protons up to an energy of 450 GeV which can then be injected into the LHC. Beams from the SPS are also used to provide beams for several of CERN's fixed target experiments such as NA61 and NA62. When lead ions are required for collisions, these are produced by accelerating vaporised lead in Linac 3 and the 'Low Energy Ion Ring' (LEIR) before entering the PS and following the acceleration chain described above.

2.2 Large Hadron Collider

The LHC is a 27 km circumference particle accelerator currently capable of colliding protons with an energy of 6.5 TeV to provide a centre of mass energy, $\sqrt{s} = 13$ TeV [9]. The LHC is housed in the approximately 100 m deep tunnel previously occupied by the 'Large Electron Positron collider' (LEP), which provided collisions that enabled detailed studies of the electroweak interaction to be performed between 1989 and 2000 [10].

The LHC consists of eight straight sections and eight curved sections, in which dipole magnets bend the trajectory of the particles to enable them to continue to circulate around the LHC ring. The straight sections contain the systems for injecting, cleaning, accelerating, colliding and dumping the beams. Quadrupole magnets are used to focus the beams as they circulate. The dipole and quadrupole magnets are superconducting electromagnets that operate at a temperature of -271.3 °C, which is maintained by a liquid helium supply.

The LHC circulates two proton beams in opposite directions. At four Interaction

Points (IPs) spread around the LHC ring, quadrupole magnets are used to focus the beams into a very small cross-sectional area to increase the likelihood of many collisions occurring each time the beams are brought to pass through each other. The beams are then defocused to their normal size after passing through the IP.

Due to the rapid switching of the polarities of the RF cavities between positive and negative, the protons within the LHC beams are separated into bunches, rather than a continuous stream of protons. The design bunch spacing is 25 ns, although 50 ns was used during the first LHC running period, known as 'Run-1'. The number of bunches, n_b and the number of protons in each bunch, n_1 and n_2, can be used to provide a description of the instantaneous luminosity provided by the LHC, $\mathcal{L}$, entirely in accelerator parameters,

$$\mathcal{L} = \frac{n_b f_r n_1 n_2}{2\pi \Sigma_x \Sigma_y} \,. \tag{2.1}$$

Here, f_r is the revolution frequency of the bunches and Σ_x and Σ_y are the horizontal and vertical convolved beam widths respectively. Σ_x and Σ_y are measured by van der Meer (vdM) scans, which are performed by measuring the interaction rate as the beams are passed through each other in x and y [11]. This method results in a bell-shaped distribution of the rate of interactions with its maximum at the point of maximum beam overlap.

The instantaneous luminosity can also be expressed in terms of the proton-proton inelastic cross-section[1], σ_{inel} and the pile-up, μ, as in Equation 2.2. Pile-up is the mean number of inelastic proton-proton interactions in a single bunch crossing, denoted μ.

$$\mathcal{L} = \frac{\mu n_b f_r}{\sigma_{\text{inel}}} \,. \tag{2.2}$$

In reality, not all inelastic interactions are visible due to incomplete detector coverage. Thus, corrections must be made to account for $\sigma_{\text{inel}} \neq \sigma_{\text{vis}}$ and $\mu \neq \mu_{\text{vis}}$, where σ_{vis} and μ_{vis} correspond to the visible part of the cross-section and pile-up, respec-

[1]The rate at which protons interact where at least one of the protons does not remain intact.

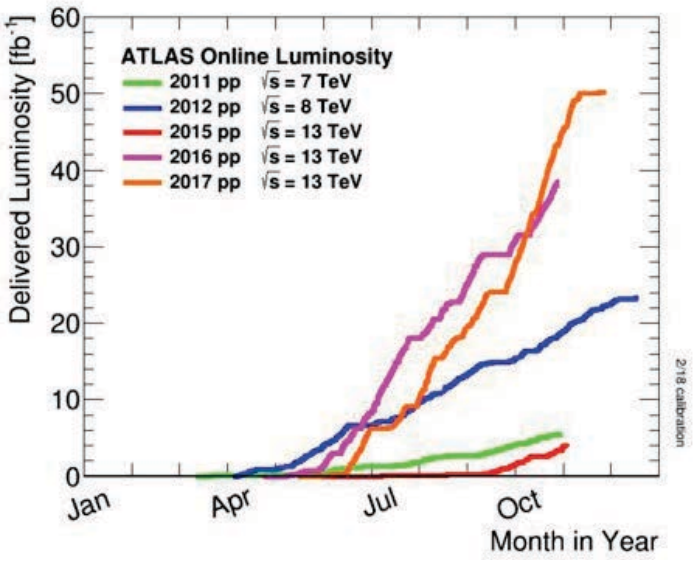

Figure 2.2: The integrated LHC delivered luminosity to ATLAS for each year of data-taking as a function of time in that year. Taken from [12].

tively. This difference is typically accounted for by measuring interacting rates with several detectors that cover different regions and thus have different sensitivities to μ_{vis}.

2.2.1 LHC Running Programme

The vast majority of LHC data taking is performed with both beams consisting of protons. This running is largely performed between Spring and late Autumn due to the high cost and demand for electricity in the colder periods of the year[2], as displayed in Figure 2.2.

No data was recorded during 2013 and 2014 as the LHC alternates between several years of producing collisions and allowing for detector upgrades. This on-off data-taking can be seen in Figure 2.3, where the LHC oscillates between the running and 'Long Shutdown' (LS) phases. The analysis described in this document concerns data collected during 'Run-1'.

[2] With the exception of late 2011 where the LHC continued operation into Winter motivated by the collection of enough data to enable the discovery of the Higgs boson.

Figure 2.3: LHC projected running schedule. Taken from [13].

2.3 LHC Experiments

A brief overview of the main LHC detectors' physics goals follows. As it is the detector used in the analysis detailed in this thesis, the 'A Toroidal LHC ApparatuS' (ATLAS) detector and its main physics goals are described in more detail in Section 3.

2.3.1 The ALICE Detector

'A Large Ion Collider Experiment' (ALICE) primarily studies the collisions of lead ions with each other [14]. One of the collaboration's research goals is to study the quark-gluon plasma, a state of matter formed when quarks and gluons are subjected to extreme densities or temperatures [15, 16].

2.3.2 The CMS Detector

The 'Compact Muon Solenoid' (CMS) detector is complementary to ATLAS, both being general-purpose detectors with a wide ranging physics programme [17]. Both detectors utilise a strong magnetic field to enable the measurement of high p_T particles and have hermetic coverage as many Beyond the Standard Model (BSM) signatures are visible via missing transverse energy.

2.3.3 The LHCb Detector

'LHC beauty' (LHCb) is an experiment looking at Charge-Parity (CP) violation [18] in the b-physics sector, among other research goals [19]. This involves the measuring of rare decay branching ratios and looking for various asymmetries with the grand motivation of explaining the matter-antimatter asymmetry observed in the universe [20]. In addition, fixed target collisions are performed by injecting noble gasses into the LHCb vertex detector region and passing proton and heavy ion beams through this region.

CHAPTER 3

The ATLAS Detector

The 'A Toroidal LHC ApparatuS' (ATLAS) detector is a general purpose detector with a wide ranging physics programme, including precision measurements of the Standard Model (SM), searches for particles to provide tests of various theories, including the discovery of the Higgs boson and the subsequent studying of its properties. The ATLAS detector, indicated in Figure 2.1, is located approximately 90m underground at the LHC and is of cylindrical shape with a diameter of 25m and a length of 44m, weighing around 7000 tonnes. This position on the LHC ring is referred to as 'IP1'.

The ATLAS detector is constructed from multiple concentric cylindrical sub-detectors which are situated around the IP with an End-Cap (EC) found at either end of this barrel region. This configuration provides near-hermetic coverage which is necessary as many BSM signatures are identifiable through inference of the presence of a non-interacting particle by observing a significant amount of Missing Transverse

Momentum (MET)[1]. These detector components are contained within a strong magnetic field to enable the measurement of charged particles with a high transverse momentum. A cross-section of the ATLAS detector is provided in Figure 3.1.

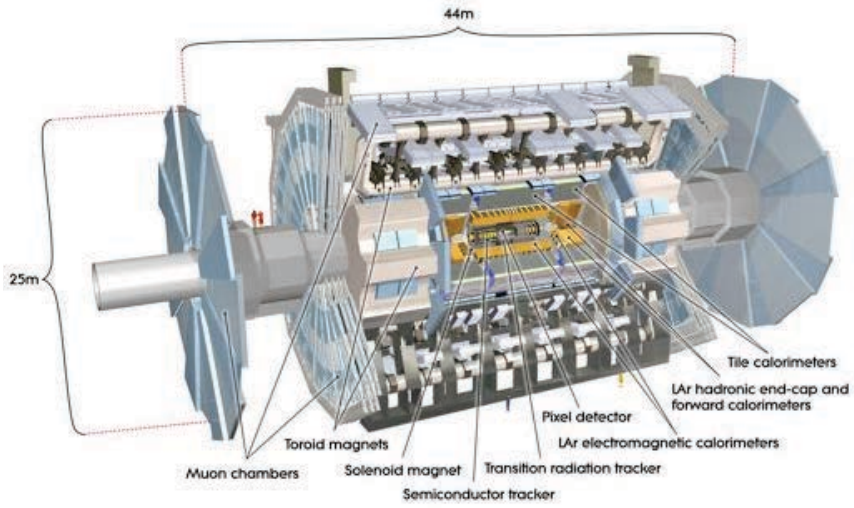

Figure 3.1: Overview of the ATLAS detector, with labelled components. Taken from [21].

Figure 3.2 displays the path of various particles through the detector in cross-section to aid in the visualisation of the layout of the detector and understand the detection responsibilities of each sub-detector.

This section provides an overview of each of the separate components that form the ATLAS detector. A more detailed description can be found in [23].[2]

[1]Due to the conservation of momentum, the sum of all momentum in the direction perpendicular to the beam should equal zero; the same as that in the incoming beams. If a BSM particle is produced with some transverse momentum but does not interact with the detector, it results in an MET signature.

[2]The detector described in this document is the 'Run-1' ATLAS detector, which is as the detector was during the collection of the data for the analysis that constitutes the bulk of this thesis. A summary of the various stages of ATLAS upgrades that will change the layout relative to that presented in this document can be found in [24].

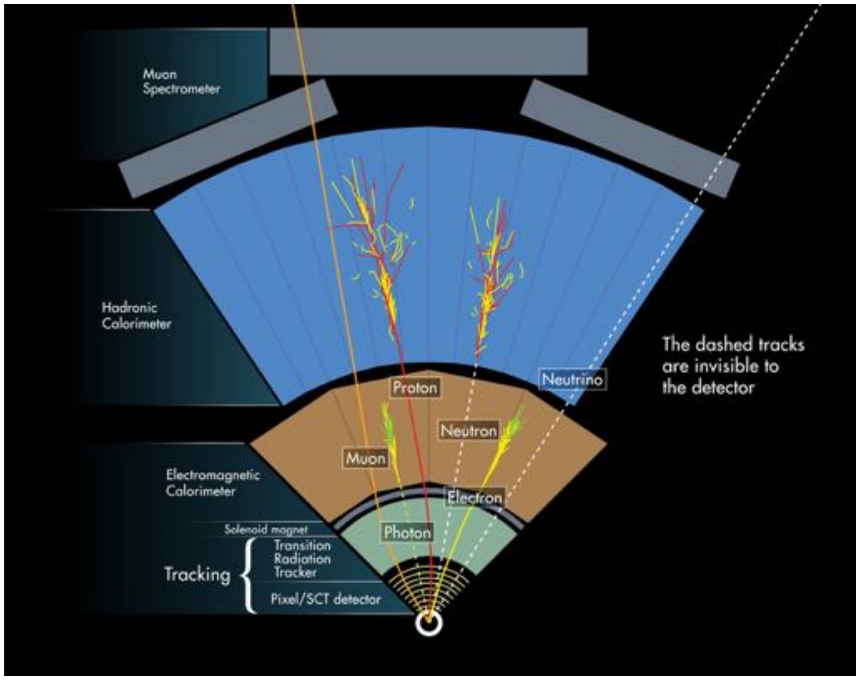

Figure 3.2: A graphic representation of where various particles are detected in ATLAS, displayed in the azimuthal plane. Taken from [22].

3.1 ATLAS Coordinate System

The ATLAS detector and its subdetectors share a common coordinate system. This system defines the IP as the origin with the positive z-axis as parallel to the beam travelling from right to left as viewed from the centre of the LHC ring. The polar angle, θ, is defined such that $\theta = 0$ points along the positive z-axis. The angle between the beam and a particle is typically expressed as a pseudorapidity, η, where,

$$\eta = -\ln\left(\tan\left(\frac{\theta}{2}\right)\right) \ . \tag{3.1}$$

η is preferred to θ as the difference between two values of pseudorapidity, $\Delta\eta$, is Lorentz invariant under boosts in the z direction if particle masses are ignored. Under this assumption that particles' masses are negligible in comparison to their momenta, η is equivalent to rapidity, y, which is defined as,

$$y = \frac{1}{2}\ln\left(\frac{E + p_z}{E - p_z}\right) \ , \tag{3.2}$$

where E is the energy of the particle and p_Z is the component of the particle's momentum in the z-plane. The half of the detector at $\eta > 0$ is labeled the 'A-side', whereas the region $\eta < 0$ is labeled the 'C-side'.

To enable a complete description of the direction of a particle, it is necessary to introduce an azimuthal angle, ϕ, centred around the z-axis with $\phi = 0$ corresponding to vertically upwards in the detector.

3.2 Magnet System

A charged particle passing though a magnetic field experiences a Lorentz force that causes the particle's trajectory to bend. This effect is utilised in most particle physics detectors by placing the detector within a magnetic field and tracking the particle as it passes through the detectors. Measuring this trajectory enables the momentum of the particle to be calculated. As the momentum resolution is inversely proportional to the strength of the magnetic field, very high field strengths are typically used.

The ATLAS detector employs a thin, superconducting NbTi-based solenoid, located outside of the 'Inner Detector' (ID). This solenoid provides a constant 2T magnetic field within the ID region, enabling momentum measurements and designed to have a very low material budget to minimise disruption to measurements by the outer detector components.

To facilitate the bending of charged particles in the muon spectrometers, located at the extremities of the main detector, eight large air-cored superconducting toroids and two EC toroids are used. These toroids provide a non-constant magnetic field in the barrel and ECs of approximately 0.5T and 1.0T respectively, enabling the tracking of muons; the only detectable particle to usually reach these detector extremities. A far better momentum resolution for high-p_{T} muons can be achieved by measuring the bending of their trajectories over this larger range than is possible within the ID, in which high-p_{T} charged particles' trajectories appear as almost

straight lines.

3.3 Inner Detector

The ATLAS 'Inner Detector' (ID) performs the detection and momentum measurement of charged particles, also enabling vertex reconstruction. There are three sections of the ID, the pixel detector; the 'SemiConductor Tracker' (SCT) and the Transition Radiation Tracker (TRT), as shown in Figure 3.3.

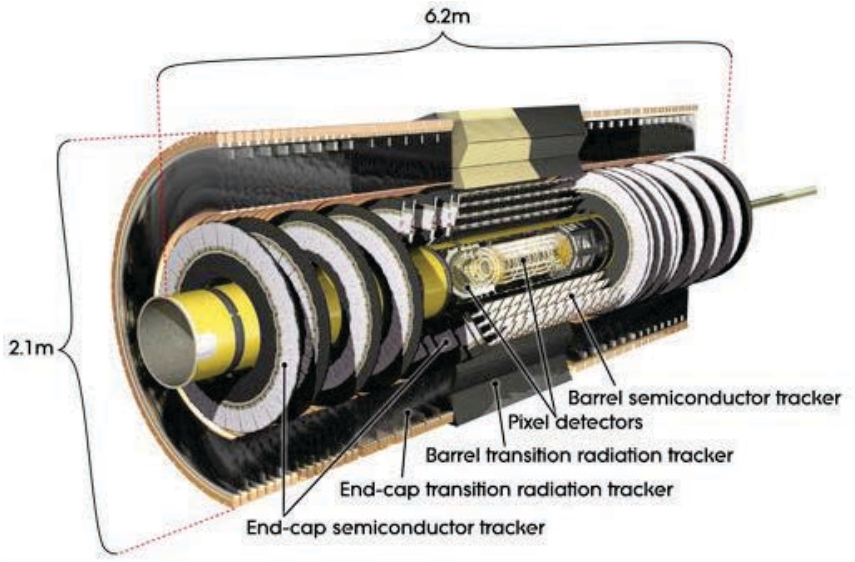

Figure 3.3: Layout of the ATLAS inner detector. Taken from [23].

These complementary sections of the ID operate within the 2T magnetic field produced by the solenoid, providing coverage in the range $|\eta| < 2.5$. This field bends the paths of charged particles passing through the ID, enabling the measurement of their momentum from the curvature of the tracks which are formed by combining multiple detections of the particle during its transition through the detector. The fractional momentum resolution of the ID is $\sigma_{p_\mathrm{T}}/p_\mathrm{T} = 0.05\% \cdot p_\mathrm{T} \oplus 1\%$.

Both the pixel detector and the SCT are silicon detectors, comprised of pixel sensors and micro-strip sensors respectively. They function by the separation towards electrodes of electron-hole pairs produced by an incident charged particle using an

electric field. The collection of this ionisation current results in one 'space point', and when many of these points are detected a track can be reconstructed. The pixel detector is arranged in three concentric cylinders and three EC disks, totalling approximately 80.4 million readout channels. The closest pixel layer is 50.5mm from the centre of the beam-pipe, see Figure 3.4. The spatial resolution provided by the pixel detector is 10 μm in the R-ϕ plane and 115 μm in z and R for the barrel and EC modules, respectively. The SCT is located radially outside of the pixel detector, consisting of four cylindrical layers and nine EC disks, totalling 768 silicon strips and approximately 6.3 million SCT readout channels. The spatial resolution provided by the SCT is 17 μm in the R-ϕ plane and 580 μm in z and R.

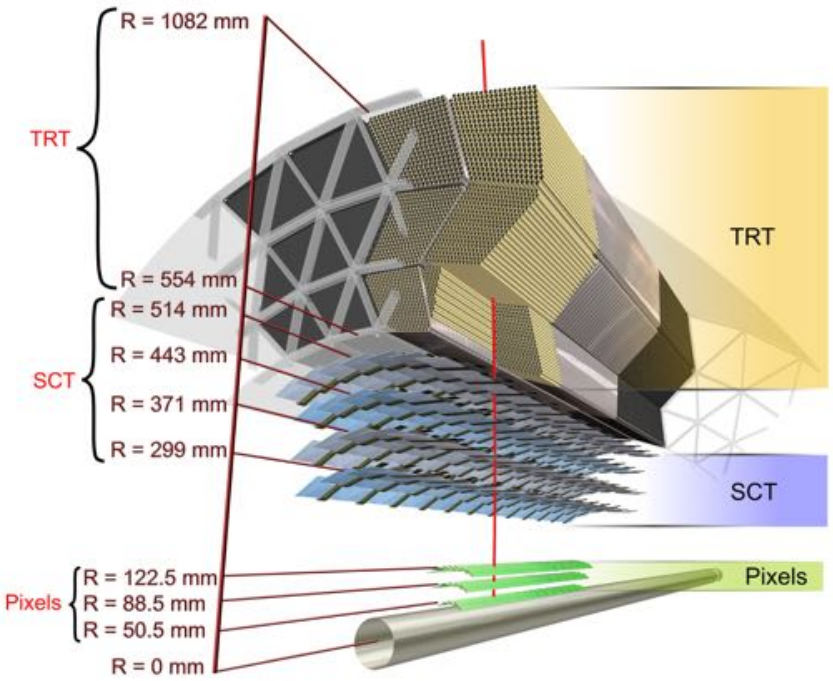

Figure 3.4: ATLAS ID layers and their distance from the IP. Taken from [25].

The outermost region of the ID is the TRT, which occupies most of the volume of the ID. The TRT is constructed of approximately 351,000 thin aluminium tubes, reinforced with a graphite polyamide, of diameter 4mm covering the region $|\eta| < 2.0$. The tubes are oriented parallel to the beam in the barrel region and radially in the

ECs. Within each of these tubes is a 31 μm diameter gold-plated tungsten wire in a xenon-based gas mixture. Charged particles passing through this gas result in ionisation, which is detected using an electric field to separate the ions and electrons between the walls and wire, forming a signal pulse. The aluminium tubes are surrounded by CO_2 gas, resulting in the emission of transition radiation when a charged particle traverses from inside to outside the tube, due to the different refractive indicies of xenon and CO_2. The amount of transition radiation produced is dependent on the velocity of the particle, enabling differentiation between electrons and charged hadrons, with electrons producing significantly more transition radiation [26]. The TRT provides a comparatively poor spatial resolution of 130 μm, limited by the maximum drift time measured in each channel. Despite the lower spatial resolution, the TRT contributes significantly to the momentum measurement as an average of 35 hits are provided per track from the TRT.

3.4 Calorimeters

The role of a calorimeter in a particle physics detector is to accurately measure the energy of particles by stopping the particle and measuring the energy deposited in this process. This quality is useful for many purposes but it is particularly important for reconstructing invariant masses of particles from their decay products and inferring the presence of missing energy due to neutrinos or BSM physics, which are both integral to ATLAS's primary physics goals. In ATLAS the calorimeter is the only subdetector that is able to detect photons.

The ATLAS detector employs two types of calorimeter, these are the electromagnetic calorimeter and hadronic calorimeter, as seen in Figure 3.5. The electromagnetic calorimeter is responsible for measuring electrons and photons, while the hadronic calorimeter is primarily responsible for detecting jets, hadronic τ decays and calculating Missing Transverse Momentum (MET) through the detection of everything else. This separation into two calorimeters aids in particle identification.

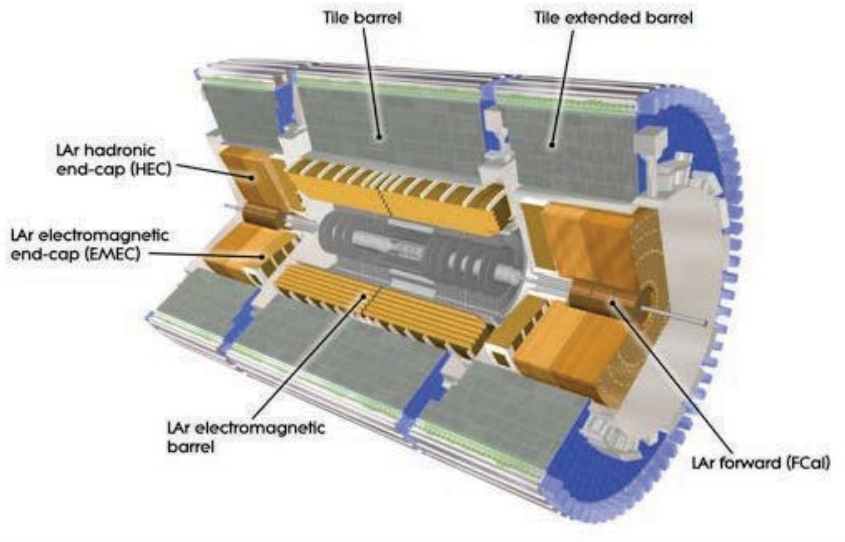

Figure 3.5: Schematic diagram of the ATLAS calorimeters displaying the electromagnetic and hadronic calorimeters. Taken from [23].

Both of ATLAS's calorimeters are sampling calorimeters. A sampling calorimeter uses alternating layers of an absorbing material, which is typically very dense, to create particle showers and a sampling material, which generates a detectable signal. The shower size and shape are then measured to determine the energy. Due to the high centre-of-mass energies produced by the LHC, the ATLAS calorimeter system is required to have a good performance over a large energy range, from the GeV-scale to the TeV-scale. The design energy resolutions of the different calorimeter regions are listed in Table 3.1. In test beams, the calorimeter regions were observed to satisfy the design requirements [27, 28]. An overview of each component is given in this section.

Calorimeter region	**Design resolution**
LAr EM calorimeter	$\sigma_E/E = 10\%/\sqrt{E} \oplus 1\%$
Hadronic calorimeter (barrel and EC)	$\sigma_E/E = 50\%/\sqrt{E} \oplus 3\%$
Hadronic calorimeter (forward)	$\sigma_E/E = 100\%/\sqrt{E} \oplus 10\%$

Table 3.1: Fractional energy resolution of the ATLAS calorimeter regions. Values from [23].

3.4.1 Electromagnetic Calorimeter

As implied by the name, an electromagnetic calorimeter is designed to measure particles that interact electromagnetically (i.e. electrons and photons). It is also required that it does not prevent the particles that interact hadronically from reaching the hadronic calorimeter and thus cannot be too deep. The ability to absorb electrons and photons typically determines the depth of an electromagnetic calorimeter.

The ATLAS electromagnetic calorimeter is separated into two sections, the main accordion region ($|\eta| < 3.2$) containing the barrel ($|\eta| < 1.5$) and ECs ($1.4 < |\eta| < 3.2$), and the forward calorimeter ($3.1 < |\eta| < 4.9$). The accordion region has a lead absorber and Liquid Argon (LAr) sampling material, with copper sheets in the LAr region collecting and reading out the signal. The accordion geometry ensures there are no azimuthal gaps in the coverage of the calorimeter, as seen in Figure 3.6, with the goal of reducing leakage of energy and thus improving the energy resolution. The forward region consists of beam-parallel copper wires surrounded by LAr inside copper tubes. All of the LAr electromagnetic calorimeters measure the electrical signal induced by drifting electrons in the LAr region produced by ionisation from shower components generated in the absorbers. The depth of the electromagnetic calorimeter varies between 20 and 38 radiation lengths across its different components[3].

3.4.2 Hadronic Calorimeter

ATLAS's hadronic calorimeter is located radially behind the electromagnetic calorimeter and comprises a tile barrel ($|\eta| < 1.7$), the hadronic end cap ($1.5 < |\eta| < 3.2$) and the forward calorimeter ($3.1 < |\eta| < 4.9$). The tile barrel region contains steel absorbing layers and scintillating tiles for sampling. The end caps are made from copper with LAr sampling and the hadronic forward calorimeter echoes

[3]The distance travelled after which a high energy electron is reduced to $1/e$ of its incident energy through bremsstrahlung radiation.

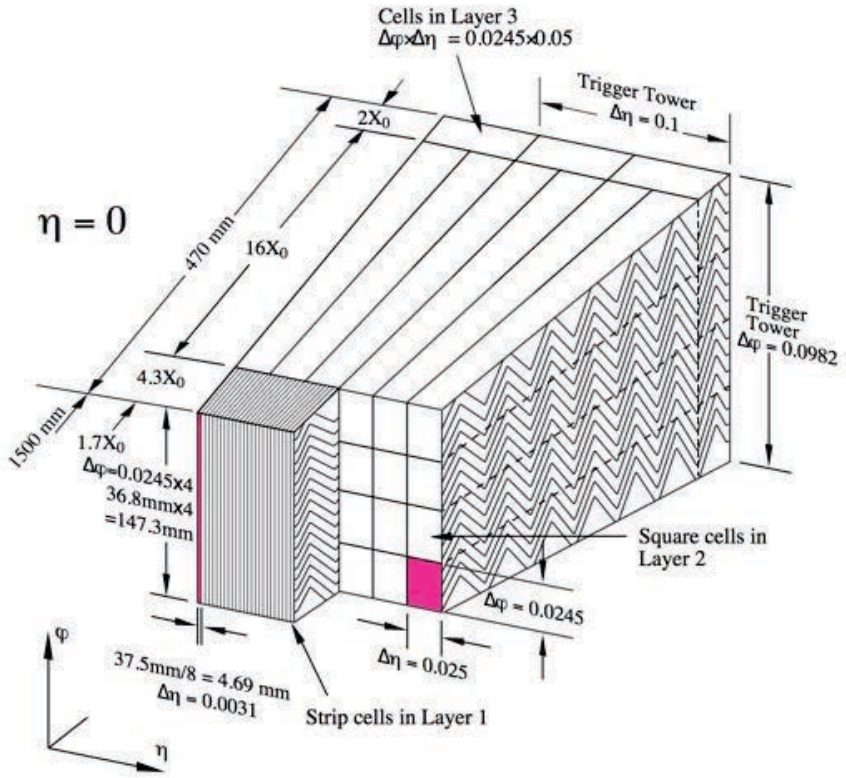

Figure 3.6: Segment of a barrel module in the electromagnetic calorimeter displaying the accordion geometry and the granularity in each layer of the module. Taken from [23].

the design of the electromagnetic forward calorimeter, but is deeper and utilises tungsten rods instead of copper. The hadronic calorimeter is designed to be deep and dense enough to stop all particles that interact hadronically, and thus muons and neutrinos are the only SM particles that should pass through all the calorimeter layers. The depth of the hadronic calorimeter system can be defined in interaction lengths[4] and is displayed in Figure 3.7 as a function of pseudorapidity.

3.5 Muon Spectrometers

The muon detectors, see Figure 3.8, are positioned around the edge of the detector, interleaved with the toroidal magnets. Like the ID, the muon spectrometer utilises

[4]The mean length after which only $1/e$ hadrons have not interacted and formed a hadronic shower.

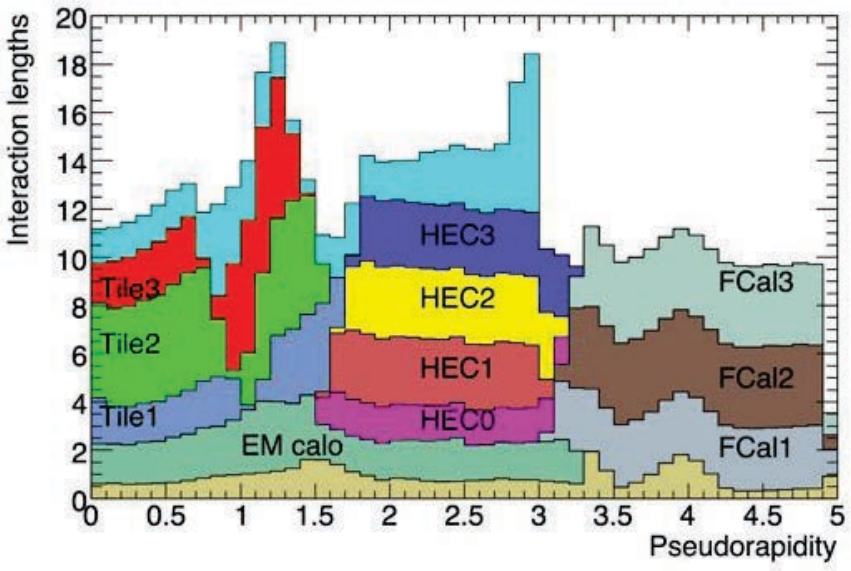

Figure 3.7: Cumulative depth in units of interaction length as a function of pseudorapidity. The individual calorimeter layers are labelled, with the first added contribution (khaki) being from the material radially inside the calorimeters and the uppermost contribution (turquoise) being the material outside the calorimeters before reaching the muon detectors. Taken from [23].

the bending of a charged particle in a magnetic field to calculate the momentum of muons. Four different types of muon detectors are used in the ATLAS detector, but all operate using gas filled regions under high-voltage that can be ionised by the muons and then these ions are detected as an electrical signal. The barrel region contains Monitored Drift Tubes (MDTs) and Resistive Plate Chambers (RPCs) whereas Cathode Strip Chambers (CSCs) and Thin Gap Chambers (TGCs) are used in the end caps, due to their ability to survive high particle fluences. RPCs and TGCs have much faster response times and thus are used for triggering. MDTs and CSCs have a better spatial resolution and thus are very important to the momentum resolution of the muon detectors. The muon spectrometer can measure momentum in the pseudorapidity region $|\eta| < 2.7$ and trigger on particles within the region $|\eta| < 2.4$. The design momentum resolution for muons with 1 TeV transverse momentum is 10%.

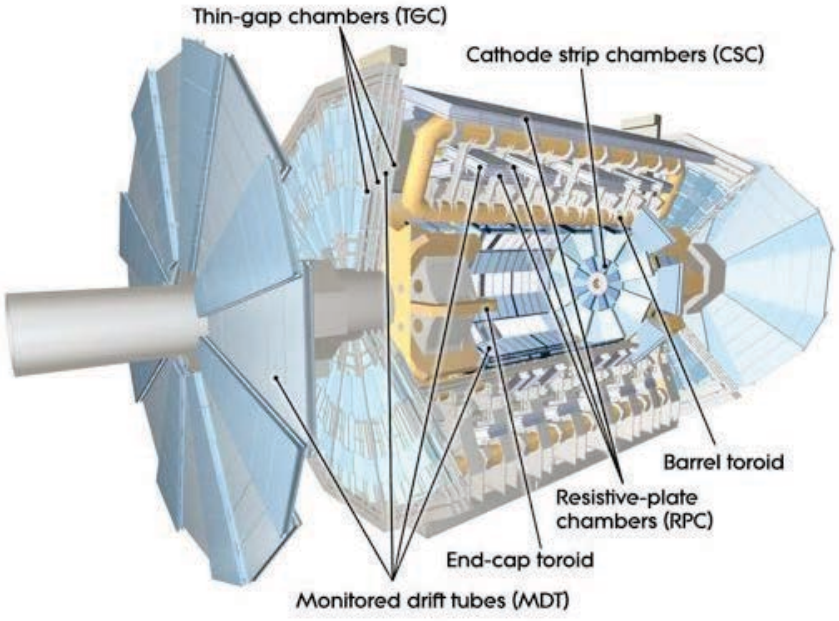

Figure 3.8: Design of the ATLAS muon system. Taken from [23].

3.6 Minimum-Bias Trigger Scintillators

The 'Minimum-Bias Trigger Scintillator' (MBTS) system is a set of polystyrene scintillator detectors separated into two concentric rings of eight scintillator tiles connected to Photo-Multiplier Tubes (PMTs) on both sides of the IP. Situated outside the ID ECs approximately 3.6 m from the IP, the MBTS detectors provide coverage in the region $2.1 < |\eta| < 3.8$. This η positing is motivated by covering the regions in the distribution of charged particles at which the maximas are observed, increasing its effectivity at triggering on as many inelastic events as possible and hence the name 'minimum-bias'. This detector component provides very high efficiency triggering and is also used to provide offline signatures for analyses such as those concerning the distribution of charged particles.

3.7 Triggering and Data Acquisition

In a hadron collider such as the LHC, the number of interactions is incredibly high [5], typically resulting in the requirement of a trigger system. This trigger system has the task of reducing the number of events that are recorded while retaining the events that are required for physics analyses.

At ATLAS, there are typically about one billion proton-proton interactions per second, see Section 2.2, corresponding to a rate of 1 GHz. The approximate size of a raw event is 1.3 Mb when written to disk, thus it is clear that not all this information can be recorded. Within the ATLAS detector, most triggers are configured to identify objects in the calorimeter and muon systems with high p_{T}, such as hadronic jets, electrons, photons, muons and MET that typically come from the decays of massive particles such as the W and Z bosons. There are also more general triggers such as the minimum-bias and random triggers which are for analyses that study the more general properties of proton-proton collisions, such as charged particle distributions and inelastic cross-section measurements.

During Run-1, the ATLAS trigger system consisted of three levels: 'Level-1' (L1), 'Level-2' (L2) and the 'Event Filter' (EF)[6]. The L1 trigger is hardware-based, meaning that the accept/reject logic is performed in the trigger hardware, rather than a software-based trigger where the accept/reject decision is made in dedicated computer farms above ground. The L1 trigger is formed from reduced granularity information from the calorimeter (all calorimeter systems) and muon spectrometer systems (RPCs and TGCs), referred to as L1Calo and L1Muon respectively. The overall L1 accept decision is produced by the Central Trigger Processor (CTP), which combines all the L1 trigger information, as displayed in Figure 3.9, and returns a decision with a latency of 2 μs. This decision can obviously not be performed within the bunch crossing spacing of 25 ns or 50 ns and so a pipeline memory is used to

[5] During ATLAS high pile-up runs in Run-1, μ was typically in the range $10 \lesssim \mu \lesssim 40$. During high pile-up runs in Run-2, $15 \lesssim \mu \lesssim 65$.

[6] For Run-2, the L2 and EF trigger levels were combined to form a high-level trigger (HLT). An L1 topological trigger (L1Topo) was also added in Run-2.

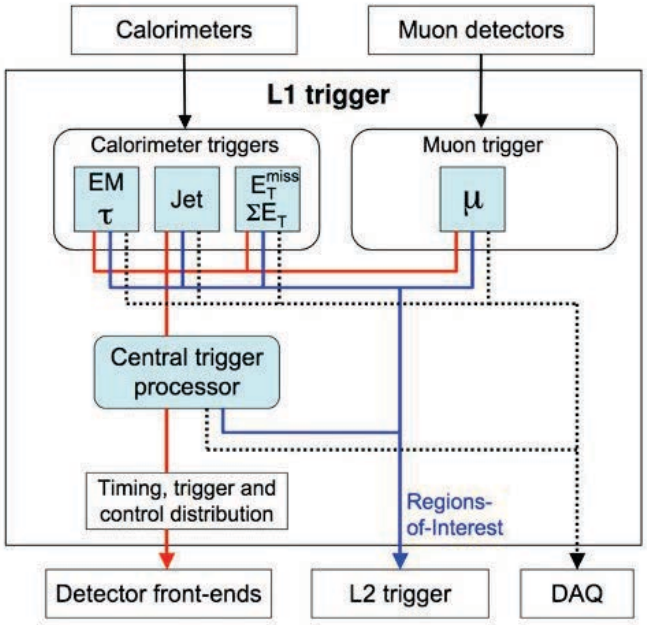

Figure 3.9: L1 trigger displayed as a block diagram. The red line displays the formation of the L1 accept decision, the blue line displays how the information is passed from the L1 to the L2 trigger and the dashed black line displays what information is read out from L1. Taken from [23].

store the information from the event until the decision can be made. This pipeline memory stores the information of the event while waiting for the L1 decision at which point, if the decision is to accept the event, the memories are read out via the ReadOut Drivers (RODs), thus freeing some of the pipeline for further events. The output rate of the L1 trigger is approximately 100 kHz. It is common for an additional rate-reducing selection to be applied to a particular trigger condition called a prescale factor, which determines what fraction of all events that pass this trigger are actually passed onto the next level of trigger. Prescales are typically applied at L1 as this is the level at which reducing the data taking rate is the most challenging.

Events passing the the L1 trigger are stored in readout buffers where they are analysed by the L2 trigger, which is implemented in software. This trigger considers the regions of interest identified by the L1 trigger in more detail. The full granularity of the detectors, including ID tracking information, is available to the L2 trigger, which filters the event storage rate down to approximately 1 kHz [30]. In contrast to

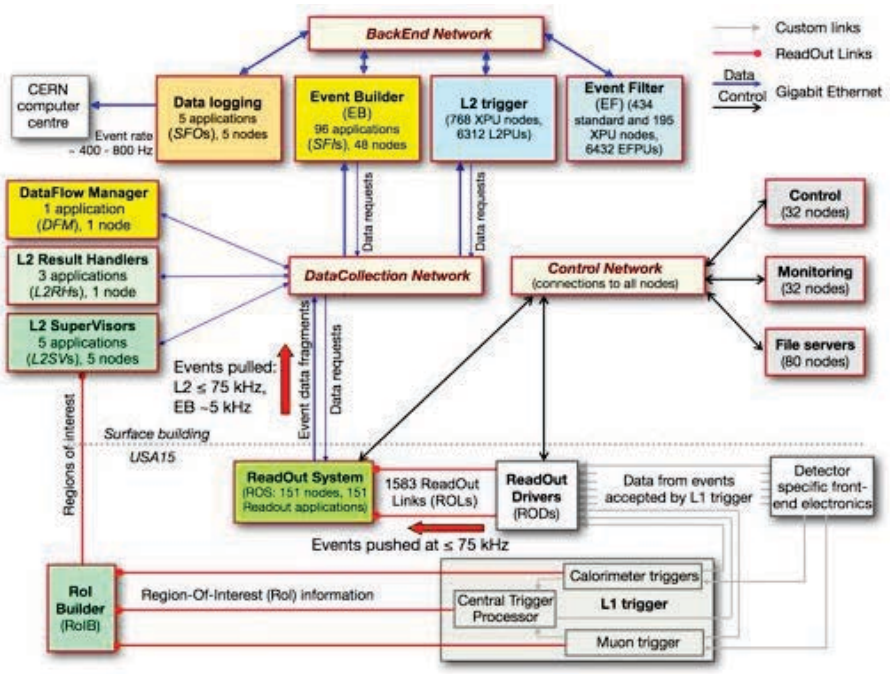

Figure 3.10: The atlas trigger and DAQ systems displayed as a block diagram. The data flow from L1 trigger to storage at the CERN computer centre is displayed. The ground-level is indicated as a horizontal dashed line. All values are applicable to September 2011. Taken from [29].

the L1 trigger, L2 decision is performed above ground, as displayed in Figure 3.10.

The final trigger level in the ATLAS detector is the EF, which selects events for storage by the CERN computer centre at a rate of approximately 0.1 kHz. Like the L2 trigger, the EF is a software trigger, but also has access to the full data of the event as well as the ID information. Both of these triggers operate similarly, but the EF has more time per event to perform more complex selection algorithms and typically applies tighter cuts than the L2 trigger.

3.8 ATLAS Physics Programme

In this section, a brief summary of the physics programme undertaken by the ATLAS Collaboration is provided. A full list of the over 700 ATLAS publications can be found at [12]. The ATLAS physics programme is separated into separate 'working

groups' which are:

- Standard Model Physics: This group focuses on fundamental interactions predicted by the SM that involve photons, W bosons, Z bosons, jets and low energy Quantum Chromodynamics (QCD) [31]. Diffraction, the process studied within this thesis, is contained within this working group.

- B Physics and Light States: With a focus on precision measurements of the production and decay of hadrons containing b-quarks, this group aims to probe the understanding of CP violation with the goal of understanding why we observe more matter than antimatter in the present day universe [20].

- Top Quark Physics: Following its discovery in 1995 [32, 33], measurements of the top quark's properties include its mass, which provides constraints on the mass of the Higgs boson enabling an evaluation of the internal consistency of the SM [34]. Top quark studies are also vital in understanding its contribution as a background for Beyond the Standard Model (BSM) physics.

- Higgs Physics: Initially having the primary goal of searching for the Higgs boson, this group now concerns itself with the measurements of properties of the Higgs boson as well as searches for BSM Higgs bosons [35].

- Supersymmetry Searches: This group is responsible for ATLAS's searches for supersymmetry; a potential extension to the SM in which each particle has a corresponding supersymmetric particle. If discovered, this theory has large implications for grand unification theories, dark matter and can naturally explain the large observed difference in strength between the couplings of the fundamental forces [36].

- Exotic Physics Searches: Searches for BSM physics are performed by the exotics group for a wide range of theories such as extra dimensions, dark matter and dark energy [37]. Many of these searches utilise the signature of a large amount of MET [38].

- Heavy Ion Physics: This analysis group studies the very high energy densities created when heavy lead ions are collided by the LHC (see Chapter 2). Measurements include many of those performed by the Standard Model working group, but where the results can vary greatly due to the different conditions in the interaction, including the production of the Quark-Gluon Plasma phase of strongly interacting matter [39].

- Physics Modelling: The physics modelling group is responsible for studies and tuning of Monte Carlo (MC) generator programs.

CHAPTER 4

Forward Detectors and ALFA

In diffractive collisions, particles are predominantly produced at very small angles from the beam, referred to as the 'forward' region. Forward detectors are used to perform measurements in these high pseudorapidity regions. The analysis work presented in this thesis utilises the 'Absolute Luminosity For ATLAS' (ALFA) forward detector, a description of which is provided here, alongside a brief summary of the other ATLAS forward detectors, 'LUminosity measurement using Cherenkov Integrating Detector' (LUCID) and the 'Zero-Degree Calorimeter' (ZDC). Also summarised is the 'TOTal Elastic and diffractive cross section Measurement' (TOTEM) detector; the analogous detector to ALFA situated near CMS. The analysis results presented in this thesis are compared to results from the TOTEM collaboration in Section 10.4.

4.1 The ALFA Detector

Situated approximately 240 m from the IP on both the A-side and C-side, the ALFA sub-detector consists of eight Roman Pot (RP) detectors which can detect scattered protons at distances only a few millimetres from the beam-line. The RPs are a special type of detector, first introduced at the 'Intersecting Storage Rings' (ISR) at CERN [40], that can be lowered into the primary vacuum region of the accelerator while remaining separated through the use of vacuum bellows, thus eliminating the risk of accidentally disturbing the vacuum.

The eight ALFA RPs are separated into four stations each comprising two RPs, one above and one below the outgoing beam. Two stations are situated on the C-side, 237 m and 241 m[1] down the beam-pipe from the IP. This formation is repeated on the A-side of the ATLAS detector, as displayed in Figure 4.1. Also displayed in Figure 4.1 is the name of each station, eg. A7L1, from which the individual names of the RPs are formed by affixing 'U' or 'L' after the station name, eg. A7L1U, corresponding to the upper and lower RPs, respectively. The combination of a near and far RP on the same side of the IP that are either both above or both below the beam-line is referred to as an armlet and this is typically the unit of detector that is responsible for detecting and reconstructing a scattered proton.

Figure 4.2 displays the layout of an individual station, showing both the upper and lower RP. Each RP is constructed from a 'Main Detector' (MD) and an 'Overlap Detector' (OD), both of which utilise scintillating fibres to detect incident particles and the resultant signals are read out by Multi-Anode Photo-Multiplier Tubes (MAPMTs). The MD comprises 20 layers of fibres in alternating u and v planes, which are rotated 45° from the (x, y) coordinate system, forming the shape of a truncated square. The ODs have three layers of fibres in the x-plane, thus only providing a vertical coordinate. The MDs are responsible for the proton detection utilised in analyses, while the ODs are required to calculate the distance between the upper and lower detectors with a precision of 10 μm. Due to the very high radiation

[1] In Run-2 the outer stations were moved to 245m.

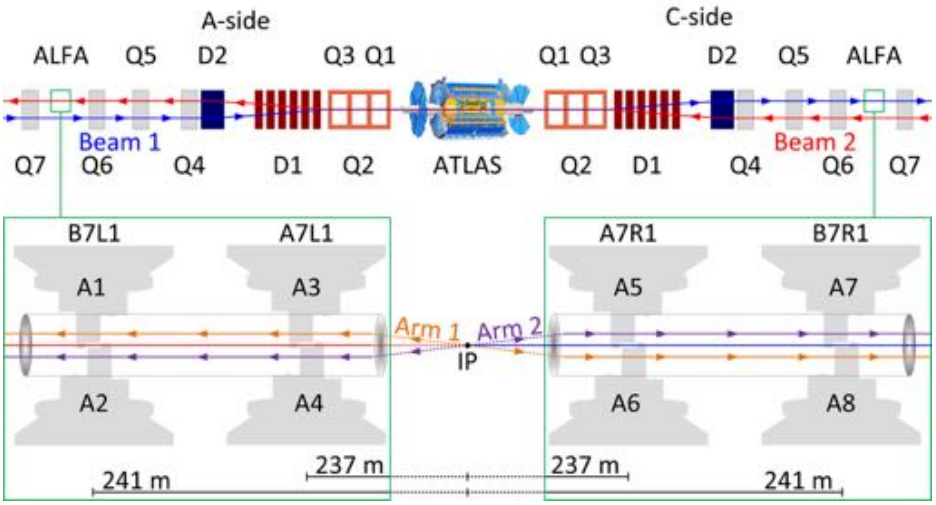

Figure 4.1: Schematic layout of the LHC optics around the ATLAS IP during Run-1. The relevant quadrupole and dipole magnets are indicated. The green expanded box displays the layout and names of the ALFA RPs. Taken from [41].

levels near the beam in standard running, the ALFA RPs are only lowered into a region near the beam for special low-luminosity runs. Thus the alignment between the upper and lower detector must be recalculated for each run in which ALFA is inserted.

Scintillating fibres are preferred over other available technologies as the signals are optical and thus not susceptible to picking up RF noise from the LHC beam. They also allow for a fully sensitive detector edge in the region closest to the beam. The main drawback to using scintillating fibres in the very forward region of a hadron collider is that the fibres are less radiation hard than alternatives and this is a major factor necessitating ALFA's removal from regular LHC high pile-up running. Following similar motivations, the 'ATLAS Forward Proton' (AFP) detector, introduced at ATLAS in Run-2, uses radiation-hard silicon pixels to perform proton-tagging in a similarly forward region, enabling it to withstand the high radiation environment and thus be included in regular high pile-up runs. AFP uses RP detectors that approach from the sides of the LHC beam rather than from above and below like ALFA. The LHC optics result in protons with different t values being separated vertically while protons with differing ξ values are separated horizontally. Thus,

AFP is more suited for diffractive dissociation measurements than ALFA which is optimised for elastic scattering measurements. AFP also provides time of flight detection enabling distinction between different interactions in the z-coordinate. A detailed description of AFP is provided at [42]

The arrays of scintillating fibres used in both the MDs and ODs have a square cross-section with height 0.5 mm and are surrounded by a 10 μm thick cladding. To minimise cross-talk from ultraviolet scintillation light, a 100 nm thick layer of aluminium foil is coated to the side faces of the fibres. Each layer of fibres in the MDs contains 64 parallel fibres and tracks are reconstructed using overlapping fibres. If all 20 layers are precisely staggered and fully efficient, it is possible to form an arrangement such that the resolution in u and v is 14.4 μm. In reality, the spatial resolution of all MDs is found to be in the range between 30 μm and 40 μm.

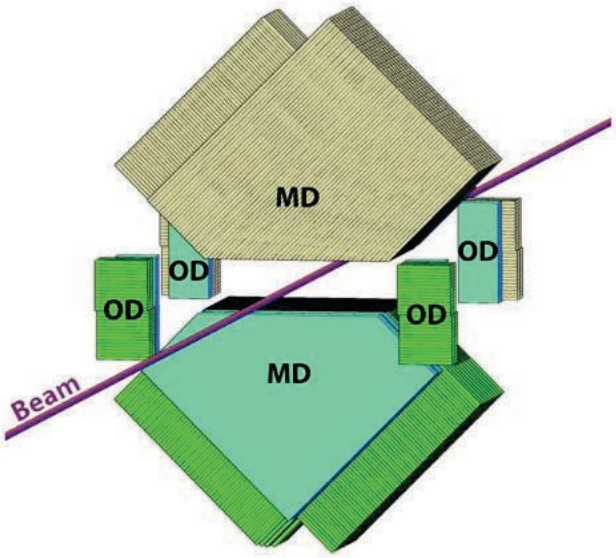

Figure 4.2: A sketch of an ALFA station. Two detectors are shown, one approaching the beam from above and one from below. The fibre directions are overlaid onto the diagram. The regions without fibre lines displayed indicate the location of the trigger tiles. The upper and lower RPs both contain all the trigger and fibre layers displayed and are symmetric about the horizontal axis. Taken from [41].

There are two 3 mm thick scintillating tiles for triggering on each MD which cover the sensitive region of the detector. The ODs are each covered by one scintillating tile. These tiles are read out by clear plastic fibres. All trigger tiles are coated in

white paint to prevent optical cross-talk. The full technical specifications of the ALFA detector can be found at [43].

The original physics programme of the ALFA group was to perform a measurement of the absolute luminosity of the LHC by detecting elastically scattered protons in the pseudorapidity region $10.6 < |\eta| < 13.5$ [44]. This measured rate can then be extrapolated to an elastic scattering cross section and, via the optical theorem, the total proton-proton cross-section can be calculated. The capabilities of the ALFA detector have also inspired the formation of a diffractive physics programme, including central ($pp \to pXp$) and single diffractive components. The single diffractive measurement constitutes the majority of this report.

4.2 Other ATLAS Forward Detectors

Although not used directly in the author's analysis, the LUCID and ZDC detectors perform complimentary roles which are briefly described here. Their relative locations about the ATLAS IP are displayed in Figure 4.3. A more detailed description of these detectors can be found at [23].

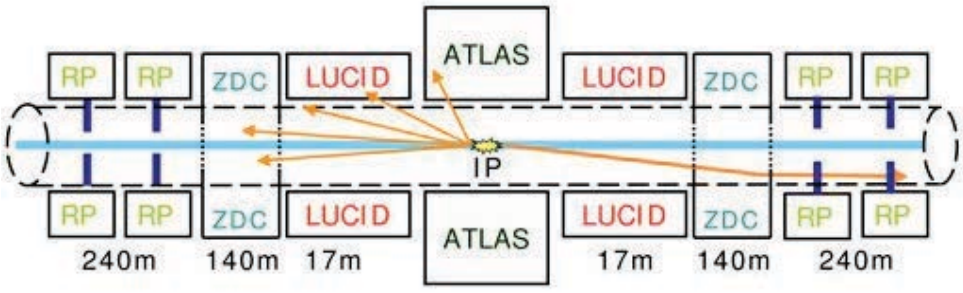

Figure 4.3: Schematic layout of ATLAS forward detectors with a typical single diffractive event depicted. The ALFA roman pots are denoted by 'RP'. Taken from [45].

4.2.1 LUCID

LUCID is a Cherenkov detector with the primary purpose of measuring the online luminosity at ATLAS. The detector is composed of sixteen 1.5 m long, 15 mm diameter aluminium tubes, filled with C_4F_{10} gas, surrounding the beam-pipe and aligned parallel to it [46]. Two detectors of this type are installed, one on each side of the IP at $z = \pm 17$ m, approximately 10 cm from the beam-line, corresponding to $5.6 < |\eta| < 6.0$. The Cherenkov thresholds within this configuration are 2.8 GeV for pions and 10 MeV for electrons. PMTs are situated at the end of the aluminium tubes to detect the resultant Cherenkov light produced by charged particles produced in proton-proton interactions.

The primary goal of the LUCID detector to measure the rate of interactions detected during a vdM scan (see section 2.2), and then compare this with the rate of interactions observed during regular running to infer an online luminosity. This relies on the principle that the number of particles interacting in LUCID is proportional to the number of interactions at the ATLAS IP, making use of the ability of LUCID to measure the number of particles incident in a single detector tube by measuring the size of the signal. Combining pile-up measurements from LUCID within its visible region, μ_{vis}, (see Section 2.2) with the calibration results from the vdM scans, the integrated luminosity can be calculated with only 1.9% uncertainty.

4.2.2 ZDC

The ZDC subdetector modules are situated 140 m downstream of the IP in both directions just after the point at which the beam-pipe separates into two to circulate the two LHC beams. Both modules contain one electromagnetic layer and three hadronic layers. All layers are constructed from tungsten sheets with quartz sampling rods connected to PMT readouts. Due to its location behind the point where the two proton beams are separated using the LHC's magnets, ZDC is largely only sensitive to neutral particles, which are unaffected by this separation, in the

region $|\eta| < 8.3$. The primary physics motivation of ZDC is the detection of very forward neutrons produced in lead-lead collisions.

While not included in the physics run studied in the main analysis in this document, it is possible for both the ZDC modules to be used in coincidence to reduce beam-halo background[2].

4.3 TOTEM

Operating in compliment to ALFA, situated around CMS at the LHC IP5 are the TOTEM detectors. Unlike ALFA, which operates as a sub-detector of the ATLAS experiment, TOTEM operated relatively autonomously during Run-1 and was considered a separate collaboration[3]. The Run-1 TOTEM detector is briefly described in this section while a more detailed description can be found at [48]. The results from the analysis described in this document are compared with a similar unpublished TOTEM analysis in Section 10.4.

As in ALFA, RPs are used by TOTEM as a means of performing measurements very close to the LHC beam. In total, 24 RPs are positioned around IP5, with 12 on each side of the IP. These RPs are separated into RP stations containing three RPs each. The RPs within an RP station are arranged such that one approaches the beam from above, one from below, and one from the radially outermost side of the LHC. The RP stations are located in pairs to provide coincidence measurements and reduce backgrounds, as with the ALFA stations. These pairs are centred at approximately $z = 147\,\text{m}$ and $z = 220\,\text{m}$ symmetrically about IP5, displayed in Figure 4.4. Differing from ALFA but similar to AFP, silicon detectors are utilised for the sensitive area of the TOTEM RP detectors.

[2] Charged particles circulating with the LHC proton beam but not contained within the main beam region.

[3] TOTEM has since been absorbed into CMS forming the CMS-TOTEM Precision Proton Spectrometer (CT-PPS)[47].

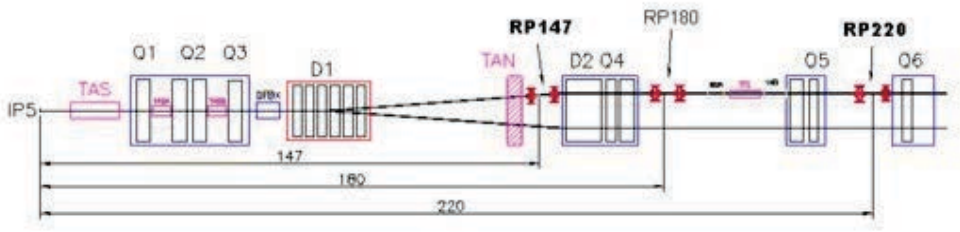

Figure 4.4: Single-sided view of the TOTEM RPs positioned at 147 m and 220 m from IP5. 'RP180' denotes another candidate location for RPs which was not utilised during Run-1. Taken from [48].

Figure 4.5: Single-sided view of the TOTEM 'forward telescopes' T1 and T2 and their positioning within the CMS detector. Taken from [48].

In addition to RP detectors, TOTEM also employs two tracking 'telescope' detectors, symmetric about IP5, providing coverage in the region $3.1 \leq |\eta| \leq 6.5$, referred to as 'T1' and 'T2' and displayed in Figure 4.5. T1 is constructed from CSCs while T2 utilises Gas Electron Multipliers (GEMs). Triggering is performed within T1, T2 and the RPs.

CHAPTER 5

Diffraction, and its place in The Standard Model

5.1 The Standard Model of Particle Physics

The Standard Model (SM) of particle physics provides the current best description of the fundamental particles and their interactions at the subatomic scale. At the time of its conception it described the behaviour of the known particles and has since successfully predicted the existence of further particles and phenomena, including the recently discovered Higgs boson [5, 6].

The SM is an $\mathrm{SU(3)_C} \times \mathrm{SU(2)_L} \times \mathrm{U(1)_Y}$ gauge theory that describes how the fundamental forces operate on elementary particles. Three of the four fundamental forces of nature are encapsulated within this description: the strong, weak and electromagnetic interactions; the SM does not provide a QFT to describe gravity. The $\mathrm{SU(3)_C}$ gauge group describes the strong interaction in QCD with three conserved colour charges, C. The electromagnetic ($\mathrm{U(1)_Y}$) and the weak ($\mathrm{SU(2)_L}$) interactions

are combined to form the Electro-Weak (EW) interaction. The EW interaction is described by the conservation of two left-handed isospin charges, L, and one hypercharge, Y.

There are two groups of elementary particles, distinguished by their spin. Particles with half-integer spin are classified as fermions and particles with integer spin are bosons. The fermions obey Fermi-Dirac statistics [49, 50] while bosons obey Bose-Einstein statistics [51]. The interactions described by the SM are mediated by the exchange of spin-1 gauge bosons. The strong interaction is mediated by gluons, the weak interaction is mediated by the electromagnetically charged $W^{\pm}$ bosons and the neutral Z^0 boson, and the photon mediates the electromagnetic interaction. To preserve local gauge invariance, these bosons should be massless. However, it is observed that the W and Z bosons have non-zero masses. This mass generation is caused by the scalar Higgs field, which has a non-zero vacuum expectation value and causes the breaking of the EW symmetry while preserving the gauge invariance of the theory [52]. The boson associated with the Higgs field is the Higgs boson, which only interacts with massive particles.

The absence of a description of gravity, among other shortcomings such as the lack of description of dark matter and dark energy mean that the SM is known to fall short of being a unified field theory, or ToE, which would provide a description of all the fundamental particles and interactions. A more detailed review of the SM can be found in [53].

5.2 Basic Kinematics

In order to describe diffraction and the strong interaction, it is first necessary to define several kinematic variables. Figure 5.1 displays the generic scattering of two particles (1 & 2) to two particles (3 & 4) where each particle is described by its four-momentum, $P_i(E_i, \vec{p_i})(i = 1, 2, 3, 4)$, which is constructed from the particle's energy, E, and vector momentum, $\vec{p}$.

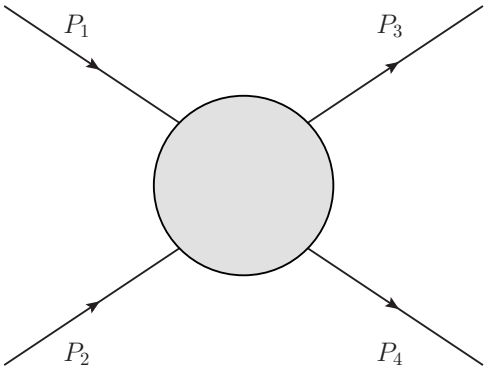

Figure 5.1: Generic scattering of two incoming particles to two outgoing particles. Vertices are not explicitly shown in order to display the most generic interaction.

The Lorentz invariant Mandelstam variables s, t and u provide useful descriptions of quantities. These are defined as,

$$s = (P_1 + P_2)^2 \ , \tag{5.1}$$

$$t = (P_1 - P_3)^2 \ . \tag{5.2}$$

and,

$$u = (P_1 - P_4)^2 \ . \tag{5.3}$$

Here, s is the square of the centre of mass energy of the interaction, while t denotes the squared four-momentum transfer in the scattering process. The addition of the Mandelstam variables is equal to the sum of the particle masses squared,

$$s + t + u = m_1^2 + m_2^2 + m_3^2 + m_4^2 \ . \tag{5.4}$$

Two body scattering interactions are named according to the mediator through which they propagate. The s-channel interaction, in which a resonance is produced, is displayed in Figure 5.2a while Figure 5.2b details a generic t-channel process, mediated via an exchange.

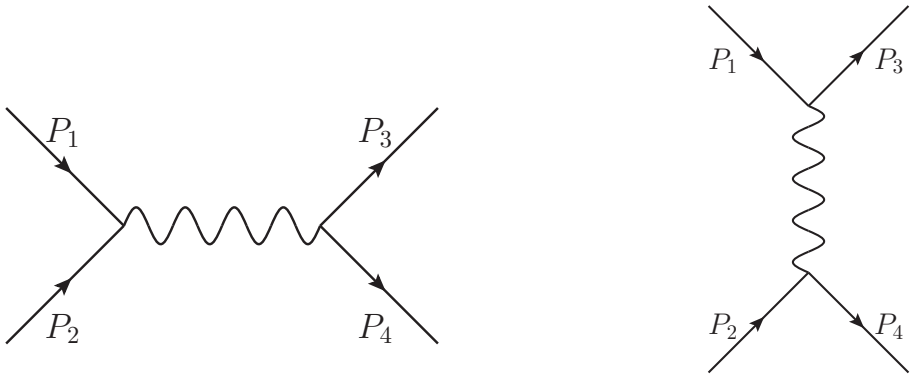

(a) s-channel exchange (b) t-channel exchange

Figure 5.2: Diagrams of an (a) s-channel process, mediated by a resonance (b) t-channel process, mediated by an exchange.

5.3 The Strong Interaction

QCD, introduced in more detail in [54], is a non-abelian gauge theory providing the description of the strong interaction in the SM. This theory describes the partonic view of interactions between the massive, spin-$\frac{1}{2}$ quarks and the massless, spin-1 gluons. Gluons are the mediators of this interaction and carry the conserved colour charge to which the strong interaction couples. The occurrence of quark-quark scattering at short distances can be modelled by a potential with a form similar to that of the Coulomb potential,

$$V_{\mathrm{QCD}}(r) = -\frac{4}{3}\frac{\alpha_{\mathrm{S}}}{r} \ , \tag{5.5}$$

where α_{S} is the strong coupling constant. The negativity of this potential defines the force as attractive and the constant, called the colour factor, stems from the existence of more than one gluon.

As both quarks and gluons carry colour charge, quark-gluon-quark and multiple-gluon vertices are possible. There are three colour charges and their corresponding anti-charges (r, g, b, $\overline{\mathrm{r}}$, $\overline{\mathrm{g}}$, $\overline{\mathrm{b}}$). Gluons exchange pairs of colour and anti-colour charge, thus one may initially expect the existence of nine distinct gluons. However, the

linear combination of all these colours and anti-colours must be colourless (necessarily as the r, g, b combination is neutral) and thus cannot carry the colour charge. The eight combinations of colours can be represented as: $\mathrm{r\bar{g}}$, $\mathrm{r\bar{b}}$, $\mathrm{g\bar{r}}$, $\mathrm{g\bar{b}}$, $\mathrm{b\bar{r}}$, $\mathrm{b\bar{g}}$, $\frac{1}{\sqrt{2}}(\mathrm{g\bar{g}} + \mathrm{b\bar{b}})$ and $\frac{1}{\sqrt{2}}$ $(\mathrm{r\bar{r}} + \mathrm{g\bar{g}})$. The state $\frac{1}{\sqrt{2}}$ $(\mathrm{r\bar{r}} + \mathrm{b\bar{b}})$ can be formed through the superposition of others already listed, while the $\frac{1}{\sqrt{3}}$ $(\mathrm{r\bar{r}} + \mathrm{b\bar{b}} + \mathrm{g\bar{g}})$ combination is colourless and thus cannot transmit colour charge.

When a pair of quarks separates, gluons are exchanged. These gluons self interact and a successful phenomenological model is obtained in the Lund String Model [55], where they form a string-like structure between the separating gluons. As the string increases in length, the energy stored within the string increases and thus so does the potential. This string potential increases linearly with distance and can be included as an extra term in $V_{\mathrm{QCD}}(r)$,

$$V_{\mathrm{QCD}}(r) = -\frac{4}{3}\frac{\alpha_{\mathrm{S}}}{r} + kr \ , \tag{5.6}$$

where k is a constant. It can be seen that at large values of r this second term dominates and $V_{\mathrm{QCD}}(r)$ increases linearly. Thus to completely separate a pair of quarks an infinite energy would be required. Instead of increasing this potential endlessly, a point is reached where it becomes energetically favourable to produce a quark and an anti-quark pair from the vacuum. This process is repeated until the energy per particle becomes low enough for the quarks and gluons to become bound in mesons ($q\overline{q}$) and baryons (qqq and $\overline{qqq}$) in a process called hadronisation. The requirement for an infinite energy to completely separate two quarks results in colour confinement, the principle that no particle carrying colour charge can be isolated and instead only colour neutral particles can be observed.

Despite its name, α_{S} is not actually a constant. Instead, the strength of the strong interaction depends on the scale, typified by the absolute value of the four-momentum transfer squared, Q^2, between the partons in the process. This 'running' of the coupling constant is displayed in Figure 5.3 and is determined to first order, at the

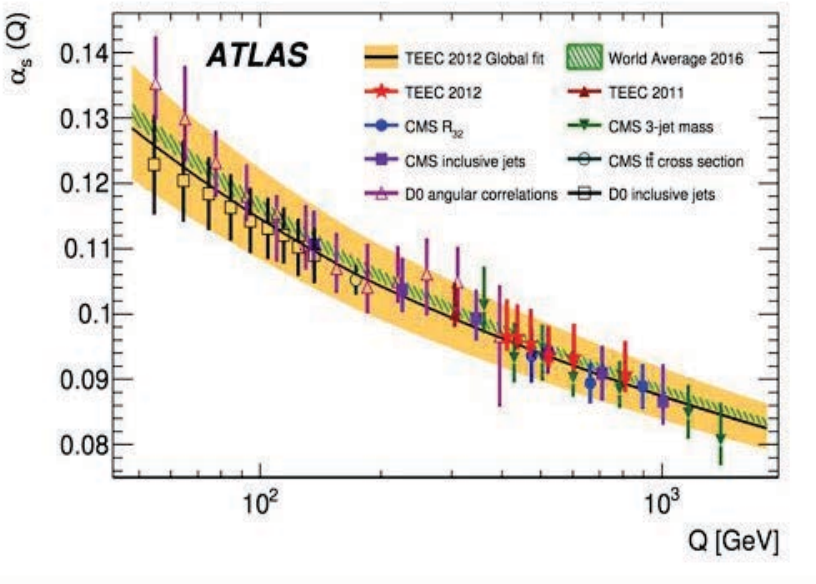

Figure 5.3: α_S as a function of the energy scale, Q. Results from multiple hadron-hadron experiments are displayed as well as a global fit. ATLAS results are displayed as red stars. The TEEC (Transverse Energy-Energy Correlation) is the mechanism under which the ATLAS data points are calculated and a separate fit to these is compared to the world average [56]. Taken from [57].

one loop level in perturbative QCD, by

$$\alpha_{\mathrm{S}}(Q^2) \approx \frac{1}{\beta_0 \log \frac{Q^2}{\Lambda^2_{QCD}}} \ , \tag{5.7}$$

where β_0, the first coefficient of the QCD beta function [58], is

$$\beta_0 = \frac{33 - 2n_f}{12\pi} \tag{5.8}$$

and n_f is the number of quark flavours. $\Lambda_{QCD} \approx 200\,\mathrm{MeV}$ is the characteristic QCD scale.

It can be seen from Equation 5.7 that α_{S} decreases as Q increases, a property that is known as asymptotic freedom. In the region in which α_{S} is small, when $Q \gg \Lambda_{QCD}$, perturbative QCD becomes applicable and calculations can be performed as a series of powers of α_{S}. Interactions that occur in this high energy, short distance, regime are referred to as 'hard' interactions. Conversely, when no hard scale is present,

α_S becomes large and the calculations diverge as powers of α_S increase. Thus, perturbative QCD is no longer applicable. In this region, to describe so-called 'soft' interactions one must turn to phenomenological models such as Regge theory, see Section 5.4.

5.4 Regge Theory and Scattering Amplitudes

Traditionally, diffraction is described with the concept of 'Pomeron exchange', which emerged in the context of Regge Theory. In 1959, Tullio Regge solved the non-relativistic equation for hadron-hadron scattering, analytically continuing (extending the domain) of the partial wave solutions and allowing the angular momentum to take complex and continuous values, rather than the then accepted integer values of J [59]. This results in relationships between mass-squared (s-channel) or t (t-channel) and angular momentum in the form of so-called Regge trajectories, $\alpha(t)$, expressed as,

$$\alpha(t) = \alpha(0) + \alpha' t \ . \tag{5.9}$$

At integer values of $\Re[\alpha(t)]$, observable resonances in the s-channel exist, while unstable hadrons also possess an imaginary component in $\alpha(t)$ which is related to their decay width. These resonances possess identical quantum numbers except for their differing angular momentum, J. The ρ trajectory, along with other states $(f_2, \omega, a_2, \omega_3)$ are displayed on a Chew-Frautshi plot of $\Re[\alpha(t)]$ as a function of M^2, in Figure 5.4. These mesons are collectively known as the Reggeon trajectory, $\mathbb{R}$, and are well described by the linear form $\alpha(t) = 0.5 + 0.9t$.

It is possible to express scattering amplitudes, $A(s,t)$, as the sum of s-channel resonances in partial wave solutions from the discrete angular momentum, as displayed pictorially in Figure 5.5. However, at large s, the density of resonances and number of solutions to the scattering equation mean it is simpler to represent the scattering amplitude as a sum in complex angular momentum space of t-channel partial wave solutions using the Sommerfeld-Watson transformation [61]. This transformation

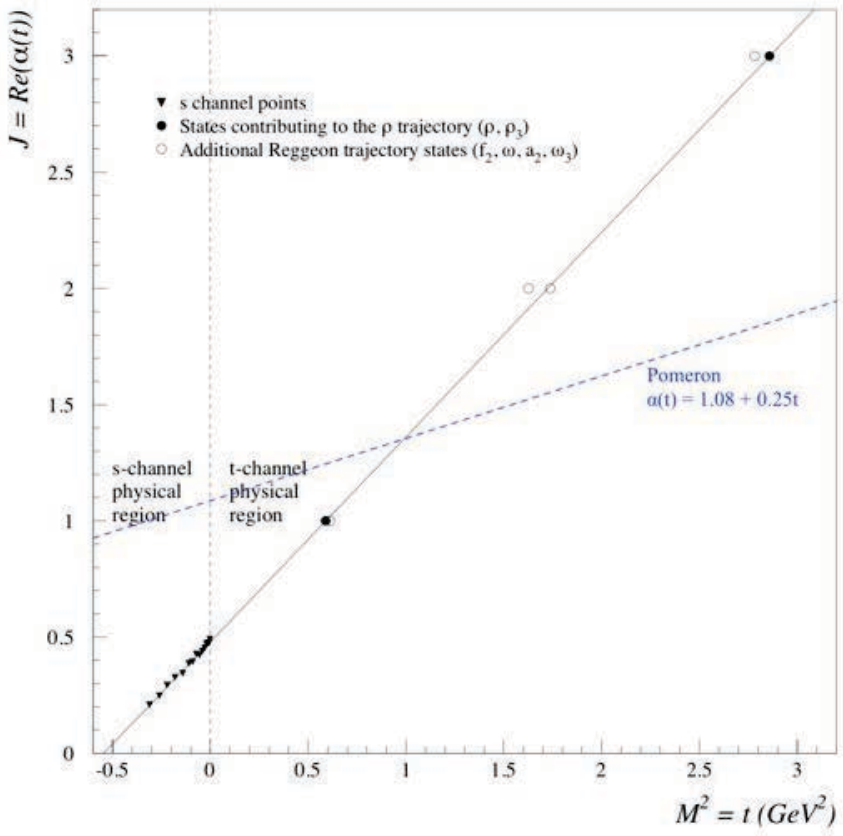

Figure 5.4: A Chew-Frautshi plot of the Regge trajectories for several degenerate meson families, $\mathbb{R}$. The Pomeron trajectory is displayed in blue and is discussed in Section 5.5. Adapted from [60].

enables the scattering amplitude to be expressed as a sum of Regge trajectories which, at large s with $|t| \ll s$, results in [62],

$$A(s,t) \propto s^{\alpha(t)} \ . \tag{5.10}$$

5.5 The Total Cross-section and the Pomeron

Elastic scattering ($AB \rightarrow AB$), where the two outgoing particles are the same as the two incident particles and have the same energy before and after the interaction, is mediated predominantly by the Pomeron and thus, from Equation 5.10, can be expressed as $A^{AB\rightarrow AB}(s,t) \propto s^{\alpha(t)}$. The optical theorem, expressed in Equation 5.11,

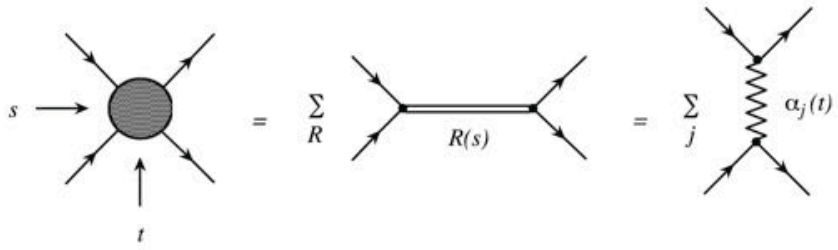

Figure 5.5: The scattering process, described as both the sum over s-channel resonances, $R(s)$, and t-channel Reggeon exchanges. Taken from [63].

relates the total cross-section to the imaginary component of the forward ($t = 0$) elastic scattering amplitude.

$$\sigma_{TOT}^{AB}(s) = \frac{1}{s} Im[A^{AB\to AB}(s, t = 0)] \sim s^{\alpha(0)-1} \ . \tag{5.11}$$

The elastic amplitude is almost entirely imaginary.

For the $\mathbb{R}$ with $\alpha(0) \sim 0.5$, this results in a total cross-section behaving as $\sim s^{-0.5}$. This prediction is in agreement with measurements when $\sqrt{s}$ is small. However it is observed that the cross-section starts to increase with s above $\sqrt{s} \sim 10\,\text{GeV}$. Figure 5.6 displays this effect for pp and $p\bar{p}$ interactions, but it is also observed in all other total hadronic cross-sections, such a πp [64]. The observed difference between pp and $p\bar{p}$ cross-sections at low $\sqrt{s}$ is due to the negative charge parity of the ω and ρ, which causes the signs of these contributions to change when a particle is replaced by an anti-particle. Accordingly, the $\bar{p}\bar{p}$ total cross-section should resemble the pp cross-section.

To account for this rising rather than falling cross-section as a function of the centre of mass energy, another Regge trajectory is required with $\alpha(0) > 1$. This trajectory is named the 'Pomeron', after Isaac Pomeranchuk. The Pomeron is a colour singlet with positive charge parity and possesses the quantum numbers of the vacuum. This property enables it to mediate elastic scattering and implies that it should couple to nucleons and anti-nucleons identically at high energy, satisfying Pomeranchuk's

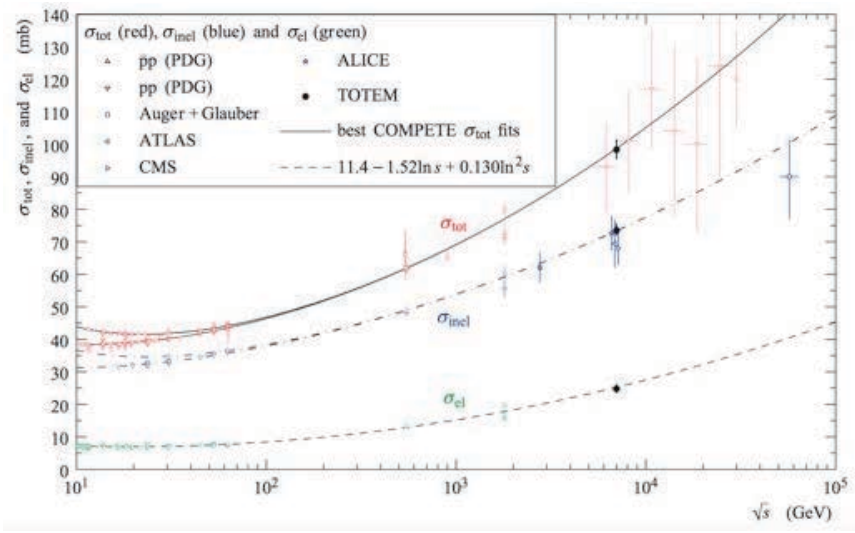

Figure 5.6: Proton-proton cross-sections (elastic (green), inelastic (blue) and total (red)). Results from multiple experiments are displayed as well as extrapolation of fits to pre-LHC data from the TOTEM collaboration. The very high energy points come from the Pierre Auger Observatory from cosmic ray scattering data [65]. The mid and low energy points come from a variety of proton-proton and proton-antiproton scattering experiments. Taken from [66].

theorem,

$$\frac{\sigma^{AB}}{\sigma^{A\bar{B}}} \overset{s\to\infty}{=} 1 \ , \tag{5.12}$$

where A and B are any two hadrons [67].

Fits to total cross-section measurements, such as those in Figure 5.6, result in a value of $\alpha_{\mathbb{P}}(0) \sim 1.08$ [68, 68], although tensions do exist with some more recent data [69]. If $\alpha(0) = 1$ for the Pomeron, its contribution to the total cross-section should not be dependent upon s. The deviation from unity is often termed ϵ, where $\alpha_{\mathbb{P}}(0) = 1 + \epsilon$. This parameterisation of $\alpha_{\mathbb{P}}(t)$ is displayed in Figure 5.4.

Of interest when considering the growth of cross-sections with centre of mass energy is the Froissart-Martin bound [70, 71]. This places an upper limit on the asymptotic growth of the total cross-section as a function of s,

$$\sigma_{TOT}(s) < K \ \ln^2(s) \ , \tag{5.13}$$

where K is an undetermined constant. This is generally not considered to be a

constraining limit at LHC energies, but it indicates that if the Pomeron trajectory is to be accepted, something must alter at higher energies to prevent the cross-section from violating this condition.

Beyond the fits to cross-section measurements, very little else is known about the Pomeron. It appears that the Pomeron couples to separate single quarks (and anti-quarks) in a hadron, as the ratio of couplings to nucleons and pions is measured to be $\sim 3/2$ [64]. It is possible that Pomeron exchange in the t-channel corresponds to s-channel production of glueballs [72], with the typical perturbative interpretation being that of two gluons. However, there is no absolute consensus on how to understand the Pomeron in terms of partons.

5.5.1 Proton-Proton Cross-section Decomposition

Based on elastic scattering measured in ALFA and Equation 5.11, the total proton-proton cross-section is measured by ATLAS to be 96.07 ± 0.92 mb at $\sqrt{s} = 8\,\text{TeV}$ [73]. It is often separated into three categories: elastic scattering, diffractive scattering and non-diffractive scattering. In this section these interactions are discussed in the context of proton-proton collisions, although diffractive scattering can also occur with other initial configurations of particles [74, 75]. Elastic scattering, depicted in Figure 5.7a, is defined as the interaction $AB \to AB$, in which the outgoing particles have the same energy as the incoming particles. These events are typified by very small t and are dominated at LHC energies by Pomeron exchange. At very small t ($|t| \ll 0.01\,\text{GeV}^2$) the Coulomb Nuclear Interference (CNI) region is reached, in which the contribution from photon exchange becomes significant. Elastic scattering contributes approximately a quarter of the total proton-proton cross-section and is measured by ATLAS in $\sqrt{s} = 8\,\text{TeV}$ collisions to be 24.33 ± 0.39 mb [73].

Diffractive scattering processes constitute a significant fraction ($\sim 25\%$) of the total proton-proton cross-section. These processes are defined at the theoretical level as those in which a dissociative X system, with mass M_X, is produced while no quantum

numbers are exchanged between the two interacting particles. The interaction can be understood through Pomeron exchange. At the observable level, the definition of diffractive scattering is looser, often being defined experimentally in terms of events with a large gap in rapidity between the final states.

Figures 5.7b and 5.7c display single dissociative diffraction (SD) and double dissociative diffraction (DD) processes, where the naming is derived from the number of incoming protons that dissociate into final states that are not solely protons. In SD interactions there is a rapidity gap between the X system and the outgoing proton, while in DD interactions it is between the X and Y systems. The ALICE collaboration estimated the SD and DD cross-sections to be $14.9\ ^{+3.4}_{-5.9}$ mb and 9.0 ± 2.6 mb respectively, in $\sqrt{s} = 7\,\text{TeV}$ proton-proton collisions using operational gap-based definitions [76]. It is worth noting that these cross-sections were achieved by observing SD and DD events in a relatively small window of their diffractive mass and rapidity gap size phase space. With no information outside this range of measurement, the extrapolation factors and corresponding uncertainties themselves are very difficult to constrain accurately.

Figure 5.7d displays central diffraction (CD), which entails the formation of a third vertex at the intersection of Pomerons from each interacting proton; for this reason it is also referred to as Double Pomeron Exchange (DPE). While similar to elastic scattering in that it results in two intact protons, the X system produced in CD interactions forbids the final state protons from maintaining their incoming energy. Rapidity gaps are expected between both protons and the X system. As CD is a higher order process, it has a significantly reduced cross-section compared with SD and DD, measured fractionally to be 0.194 ± 0.012 of the one-sided SD cross-section in proton-antiproton collisions at $\sqrt{s} = 1.8\,\text{TeV}$ by the CDF collaboration [77]. Extrapolating this measurement to proton-proton collisions, by doubling σ_{SD} to account for the SD process in both directions, corresponds fractionally to 0.097 ± 0.006 of the SD cross-section.

The remaining $\sim 50\%$ of proton-proton interactions are classified as Non-Diffractive

(ND), see Figure 5.7e. The rapidity gap observable is a powerful discriminant between diffractive and non-diffractive events as, typically in proton-proton collisions at $\sqrt{s} = 8\,\text{TeV}$, approximately five charged particles are observed per unit rapidity [78]. ND interactions are understood through the exchange of colour charge-carrying partons.

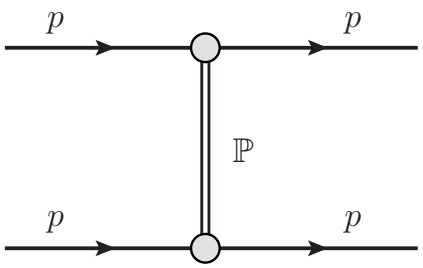

(a) Elastic Scattering

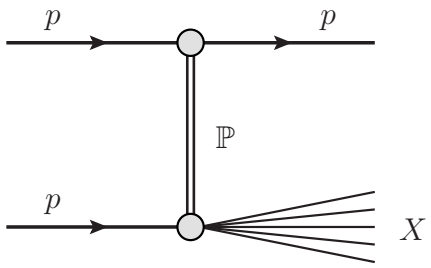

(b) Single Diffraction

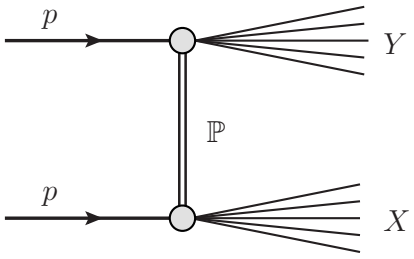

(c) Double Diffraction

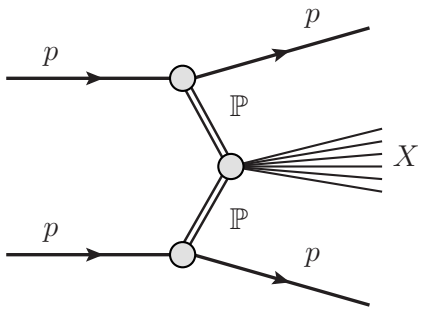

(d) Central Diffraction

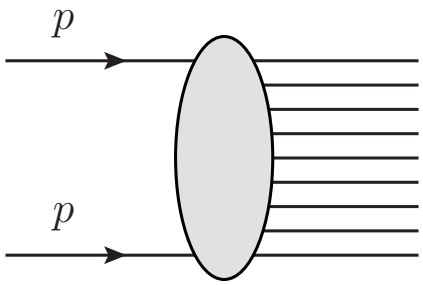

(e) Non-Diffraction Scattering

Figure 5.7: Diagrams of two incoming protons undergoing (a) elastic scattering, (b) single dissociative diffraction, (c) double dissociative diffraction, (d) central dissociative diffraction and (e) non-diffractive scattering.

5.6 Single Diffraction Cross-section Formalism

It is possible to represent the SD differential cross-section as a function of the properties of Regge trajectories. Underpinning this is Mueller's generalisation of the optical theorem [79], which enables $AB \to CX$ SD scattering to be represented as $AB\bar{C} \to AB\bar{C}$ elastic scattering through $AB\bar{C} \to X$ by changing the outgoing C particle to be its incoming antiparticle, $\bar{C}$, and where X sums over all possible states. This representation is illustrated in Figure 5.8 and is valid in the region of phase space $s \gg M_X^2 \gg t$. This restriction is satisfied for soft SD at the LHC.

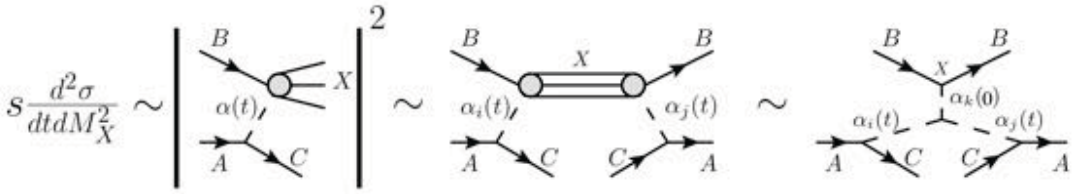

Figure 5.8: Diagrammatic representation of Mueller's generalisation of the optical theorem applied to SD scattering.

To preserve the proton in an SD event at large $\sqrt{s}$, the Regge trajectories $\alpha_i(t)$ and $\alpha_j(t)$ must be Pomerons. However this is not necessary for the trajectory $\alpha_k(0)$. The resulting scattering amplitude is therefore in principle the sum over all trajectories, k. However the $\mathbb{P}_i\mathbb{P}_j\mathbb{P}_k$ contribution is expected to strongly dominate in the region $s \gg M_X^2 \gg t$ and $M_X^2 \gg M_p^2$. This 'triple Pomeron' differential cross-section can then be expressed in Regge theory as [80, 81],

$$\frac{d^2\sigma_{SD}}{dt\ dM_X^2} = k(t)s^{2\alpha(t)-2}\left(\frac{1}{M_X^2}\right)^{2\alpha(t)-1}(M_X^2)^{\alpha(0)-1}\ , \tag{5.14}$$

where $k(t)$ contains the numerical constants, the triple Pomeron coupling and the basic t dependence of the elastic scattering amplitude, which is not predicted. Often, the SD cross-section is separated into a two components: the flux of Pomerons from the proton, $F_{\mathbb{P}/p}(M_X^2, t)$, and a total cross-section for the process $\mathbb{P}p \to X$,$\sigma_{tot}^{\mathbb{P}p\to X}$. These two processes are separated in Equation 5.14 such that $F_{\mathbb{P}/p}(M_X^2, t) \propto k(t)(1/M_X^2)^{2\alpha(t)-1}$ and $\sigma_{tot}^{\mathbb{P}p\to X} \propto (M_X^2)^{\alpha(0)-1}$.

A useful quantity with which to classify SD events is the fractional energy loss of the scattered proton, ξ,

$$\xi = 1 - \frac{E'}{E} = \frac{M_X^2}{s} \ , \tag{5.15}$$

where E and E' are the incoming and outgoing energy of the proton, respectively. The lower limit on the accessible ξ range can thus be determined by the low-mass limit on M_X which is that the X system consists of the first excitation of the dissociating proton that preserves the protons quantum numbers, $p \to p + \pi^0$, resulting in the conditions $M_X > 1.1\,\text{GeV}$ and $\log_{10}\xi > -7.7$ at $\sqrt{s} = 8\,\text{TeV}$. The diffractive signature is typically still clear up to values of $\xi \sim 0.1$. Due to the very large range of values it covers, ξ is often expressed logarithmically.

It is experimentally observed that the t-dependence of the cross-section can be described as an exponential function of t. Expressing Equation 5.14 in terms of ξ, at fixed s, results in,

$$\frac{d^2\sigma_{SD}}{dt\ d\xi} \propto \left(\frac{1}{\xi}\right)^{2\alpha(t)-\alpha(0)} e^{B_0 t} \ , \tag{5.16}$$

where B_0 is related to the mean transverse distance over which the interaction takes place. The t dependence of the ξ power can be absorbed into the exponential to leave a constant power,

$$\frac{d^2\sigma_{SD}}{dt\ d\xi} \propto \left(\frac{1}{\xi}\right)^{\alpha(0)} e^{Bt} \ , \tag{5.17}$$

where,

$$B = B_0 - 2\alpha' \ln\xi \ , \tag{5.18}$$

is referred to as the 'slope parameter', determining the steepness of the t-dependence of the cross-section. Expressed as a function of $\log_{10}(\xi)$, a more useful scale on which to visualise ξ dependences, the cross-section becomes,

$$\frac{d^2\sigma_{SD}}{dt\ d\log_{10}(\xi)} \propto \left(\frac{1}{\xi}\right)^{\alpha(0)-1} e^{Bt} \ . \tag{5.19}$$

Depending upon the parameterisation of $\alpha(t)$ and the assumed dynamics of B, the shape of the ξ distribution can vary dramatically. Figure 5.9 displays the predictions

for the SD differential cross-section as a function of ξ for several MC generators, clearly illustrating the need for experimental results to constrain these models.

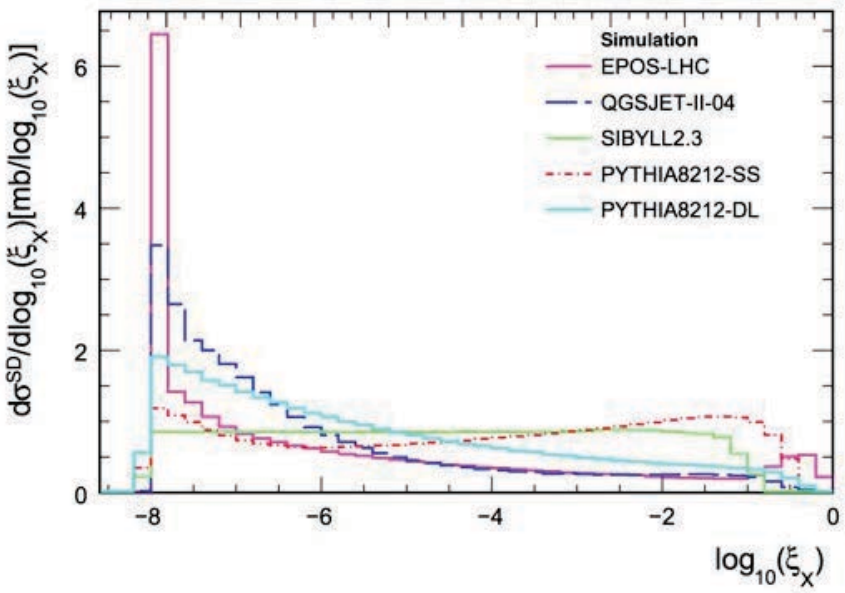

Figure 5.9: One-sided SD differential cross-section in ξ for various MC generators at $\sqrt{s} = 13\,\text{TeV}$. Adapted from [82].

5.7 Single Diffraction in Pythia

The analysis detailed in this thesis uses Monte Carlo (MC) samples produced with the Pythia8 event generator [83, 84]. A brief introduction to general purpose MC generators in the context of proton-proton collisions as well as an overview of the modelling of diffraction in Pythia8 is provided in this section. More information on LHC general purpose event generators can be found in [85]. A more detailed summary of how Pythia8 models diffraction is given in [86].

5.7.1 Introduction to Monte Carlo

The MC method assumes that the outcome of a collision can be modelled by probability density functions constructed using empirical and theoretical inputs. In a

particle physics MC generator, the generation of a single simulated event can be split into the following steps:

- Selecting the hard process and corresponding kinematics that will be simulated. These are calculated probabilistically using the Parton Distribution Functions (PDFs) of the incoming particles to the hard scatter; i.e. the process in the event with the highest momentum transfer.

- Performing the parton shower. This is the radiation of gluons and photons from the colour-charged and electromagnetically-charged incoming and outgoing partons. In addition, secondary interactions can occur between spectator partons in the incoming protons, producing further activity referred to as the 'underlying event'. The description of the event at this stage is referred to as the 'parton level'.

- The hadronisation model is applied. This is the process of confining a system of partons into hadrons. There are several different hadronisation models applied by different MC generators. In PYTHIA8, the previously describe Lund String Model is used for the hadronisation process [55]. The top quark decays before hadronisation occurs.

- Unstable particles decay. A lot of the hadrons produced in the hadronisation process are unstable resonances that decay to more stable hadrons. The ATLAS collaboration defines particles that have a lifetime enabling them to travel 10 mm from the primary vertex as stable [87]. The event at this stage is referred to as the 'hadron level', or the 'truth level'. The truth level is defined to be as close as possible to the observable final state entering the detector, but without any reconstruction effects, hence why stable particles are used in the definition.

- The detector response is simulated. This process is typically performed using a program such as GEANT4 [88]. Each particle is passed through the detector, separated into thin layers, with a probability of interacting with each layer

by, for example, ionising the gas, producing a hadronic shower or Compton scattering. The result of this stage is a simulation of the basic signals emerging from the detector prior to reconstruction.

- The final step is the event reconstruction, which collates all the 'hits' formed in the detector layers from the simulation and reconstructs ID tracks, calorimeter clusters and other useable physics objects.

5.7.2 Cross-sections

The first step in the generation of a diffractive event lies in the modelling of the total cross-section. In PYTHIA8, the parameterisation from Donnachie and Landshoff's total cross section fits is used [68], summing the Pomeron and Reggeon trajectories,

$$\sigma_{TOT}^{pp}(s) = 21.70 s^{0.0808} + 56.08 s^{-0.4545} \text{ mb}. \tag{5.20}$$

The diffractive and elastic cross-sections are then input according to specific models, with the ND cross-section comprising the remainder of the total cross-section, σ_{TOT}^{pp}, as follows,

$$\sigma_{ND}^{pp}(s) = \sigma_{TOT}^{pp}(s) - \sigma_{El}^{pp}(s) - \sigma_{SD}^{pp}(s) - \sigma_{DD}^{pp}(s) - \sigma_{CD}^{pp}(s) \ . \tag{5.21}$$

5.7.3 Kinematics and Proton Dissociation

In the PYTHIA8 MC generator, diffraction is based upon the Ingelman-Schlein approach [89] and such it is modelled as a convolution of a Pomeron flux from one proton and an interaction cross-section between the Pomeron and the other proton. The Pomeron-proton interaction is performed considering the Pomeron as a gluon-dominated combination of partons (a 'quasi-particle'). The default SD cross-section

at fixed s is parameterised as,

$$\frac{\mathrm{d}\sigma_{SD}}{\mathrm{d}t\mathrm{d}\xi} = \frac{g_{3\mathbb{P}}}{8\pi}\beta^3_{\mathbb{P}p}\frac{1}{\xi}e^{B(\xi)t}F_{SD}(\xi), \tag{5.22}$$

where $g_{3\mathbb{P}}$ is the triple-Pomeron coupling term (see Figure 5.8), $\beta^3_{\mathbb{P}p}$ is the proton-Pomeron coupling factor and $F_{SD}(\xi)$ is a 'fudge factor' to account for the behaviour outside of the region $s \gg M_X^2 \gg t$, where the description from Regge theory is no strictly longer valid [83]. The t-dependence is given by the exponential slope as in Equation 5.18. The cross-section presented in Equation 5.22, with its simple $1/\xi$ dependence, is referred to as the Schuler and Sjöstrand (SS) Pomeron flux factor.

There are several alternative parameterisations of the Pomeron flux available in PYTHIA8. The other model applied in the samples used within the analysis presented in this thesis is referred to as the Donnachie and Landshoff (DL) flux factor [68]. In this model, the exponent of the $(1/\xi)$ term in Equation 5.22 is $(2\alpha_{\mathbb{P}} - 1)$, which mirrors the $(1/M_X^2)$ term in Equation 5.14. In the DL model, the Pomeron intercept is set such that $\epsilon = 0.085$, by default. The proton-Pomeron cross-section is treated as a constant in PYTHIA8 for all Pomeron flux factors by default. However, from comparison with Equation 5.14, it can be seen that the full 'triple Regge' treatment can be reproduced by adding a ξ dependence to the proton-Pomeron cross-section of $(\xi)^{\alpha_{\mathbb{P}}(0)-1}$.

Expressing Equation 5.22 in the form of Equation 5.19, assuming no M_X^2 dependence of the proton-Pomeron cross-section, $\sigma_{tot}^{\mathbb{P}p\to X}$, the cross-section differential in $\log_{10}\xi$ at fixed s can be expressed as,

$$\frac{d^2\sigma_{SD}}{dt\ d\log_{10}(\xi)} \propto \left(\frac{1}{\xi}\right)^{2\alpha(0)-2} e^{Bt}\ . \tag{5.23}$$

While this is the default approach used in the PYTHIA8 event generator [90], the M_X^2 dependence of $\sigma_{tot}^{\mathbb{P}p\to X}$ is a tuneable parameter [86].

When it is decided that an SD event will occur in PYTHIA8, the values of t and M_X are selected using the differential cross-sections as a probability distribution

function. The proton-Pomeron interaction is modelled as a partonic collision for high diffractive masses, such as those within the acceptance of the analysis described in this thesis. This assumes that the Pomeron is factorizable and can be considered separate from the proton from which it is formed. A PDF, comprising of gluons and sea quarks, is then assigned to the Pomeron; the default Diffractive Parton Density Function (DPDF) used for the Pomeron is the H1 2006 Fit B at Leading Order (LO) [91]. The proton-Pomeron interaction is then evolved using the full PYTHIA8 machinery for partonic interactions.

CHAPTER 6

Analysis Strategy, Data Collection and Selection

In this chapter an introduction to the measurement described in this document is presented along with the details of how the data are collected. The analysis selection criteria are also described.

The relevant background sources in this analysis are briefly listed here, ranked in order of contribution size after the analysis selection is applied, to aid the reader's comprehension of the subsequent chapters:

- 'Overlay Background' (OB). Caused by the overlay of two events; one causing the ALFA signals and the other producing the central detector signals. This background is described in Chapter 8.2.
- Central Diffraction (CD). Two final state protons are produced, one of which can be detected by ALFA. The X-system can satisfy the central detector selection. See Figure 5.7d.

- Double dissociative Diffraction (DD). Occasionally, very forward charged hadrons within ALFA acceptance can be produced in the dissociation of either proton, resulting in an ALFA-tag. The X and Y-systems can satisfy the central detector selection. See Figure 5.7c.

- Non-Diffractive (ND). Very forward charged hadrons can also be produced in these collisions, although extremely rarely, and produce the required ALFA signals. ND events typically produce a lot of activity in the central detector region and so this selection criteria is usually passed. See Figure 5.7e.

6.1 Analysis Strategy

As displayed in Equation 5.19, the SD cross-section can be parameterised as a function of ξ and t. Accordingly, the best description of the SD cross-section would be provided by measuring it double differentially[1] in ξ and t. In this analysis, the SD cross-section is presented single differentially in t and in ξ. Neither of these measurements has been performed previously at the time of writing by an LHC collaboration. The double differential cross-section is deferred to future analyses, owing to time constraints and the desire to understand the single differential cross-sections before performing a more complex measurement.

ALFA is utilised to reconstruct the proton momenta and thus enable the calculation of t and ξ through Equations 5.3 and 5.15, respectively. It is also possible to measure ξ from the dissociative X system. Under the assumption that the net transverse momentum of the X system is negligible, an approximation to ξ can be calculated from the measured constituents, i, of the X system,

$$\xi \approx \frac{\sum(E_i \pm p_{z,i})}{\sqrt{s}} \ , \tag{6.1}$$

where the $(\pm)$ is determined by the direction of the scattered proton. The advantage

[1] A method of displaying how a cross-section varies as a function of a variable, eg. $\frac{d^2\sigma}{dtd\xi}$.

of this approximation to ξ is that while many particles from the X system are missed due to being outside the acceptance region in η, these are the ones that provide the smallest contribution, as $E_i - p_{z,i} \sim 0$ for particles produced at very small angles from the beam. Figure 6.1 displays the correlation between the truth level values for ξ calculated from the proton and from the particles within the X system, according to Equation 6.1. Throughout the analysis, ξ calculated from the scattered proton is referred to as ξ_p, while ξ calculated from the tracks in the ID is named ξ_{EPz}. ξ_p is the nominal method for reconstructing ξ, while ξ_{EPz} is used as a cross check. ξ_p is chosen to be the nominal ξ measurement as it is insensitive to hadronisation effects which can differ greatly between MC models. Additionally, ξ_p is a direct measure of ξ, rather than an approximation. A significant discrepancy between ξ_p and ξ_{EPz} is observed at low values of ξ, where the net transverse momentum of the X system is no longer entirely negligible.

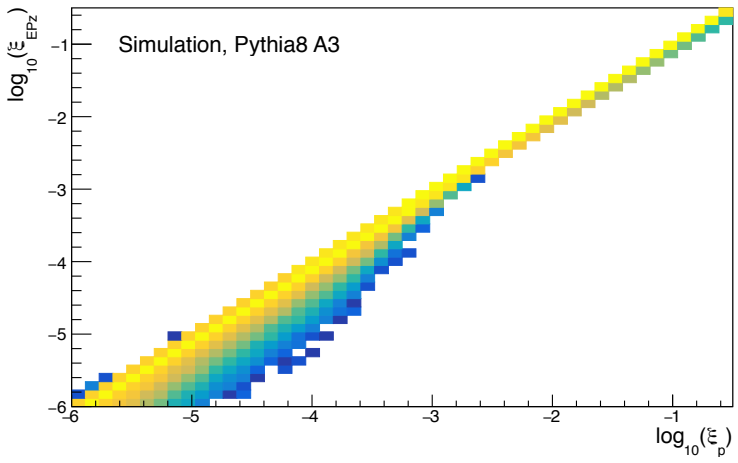

Figure 6.1: Truth level ξ as calculated from the proton (ξ_p) against ξ calculated from the dissociative X system (ξ_{EPz}). The z-axis is displayed as an arbitrary logarithmic scale. Produced using the PYTHIA8 MC generator with the A3 tune.

The typical signature that a diffractive event has occurred is the presence of a large rapidity gap in the final state particles. Various combinations of the SD and DD cross-sections have been measured at the LHC differentially in rapidity gap size [92, 93, 94], and so for comparison with previous analyses, the SD cross-section is

also presented differentially in gap size. The rapidity gap distribution between the scattered proton and the nearest particle in η, $\Delta\eta^{p\to X}$, is related to the ξ distribution as follows,

$$\Delta\eta^{p\to X} \approx -\ln(\xi). \tag{6.2}$$

The rapidity gap measured in this analysis, $\Delta\eta^{F}$, differs from the gap between the proton and the dissociated system as it is defined within our fiducial region, as detailed in Section 6.3.3, which is limited by the detector acceptance of the ID, $|\eta| < 2.5$. Additionally, only particles with $p_{\mathrm{T}} > 200\,\mathrm{MeV}$ are considered, for consistency with previous analyses. The truth level relationship between this $\Delta\eta^{F}$ and ξ is displayed in Figure 6.2. The pile up of events at low $\Delta\eta^{F}$ is due to events with small values of $\Delta\eta^{p\to X}$, where there are many particles within the coverage of the ID. The smearing of the correlation between $\Delta\eta^{F}$ and ξ is due to hadronisation fluctuations which cause the relationship in Equation 6.2 to be only approximate.

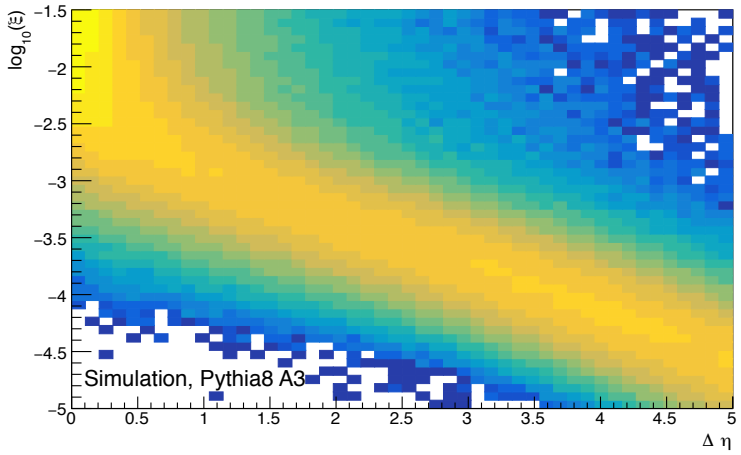

Figure 6.2: The correlation between rapidity gap, $\Delta\eta^{F}$ (x-axis), calculated from charged particles with $p_T > 200\,\mathrm{MeV}$ within the ID coverage, $|\eta| < 2.5$, and ξ as calculated from the proton (ξ_p) at the truth level. The z-axis is displayed as an arbitrary logarithmic scale. Produced using the PYTHIA8 MC generator with the A3 tune.

6.2 Data Sample

The data sample utilised in this analysis was collected during a special low luminosity run during July 2012, optimised for elastic and diffractive scattering measurements which require low pile-up conditions to identify individual events as they lack the typical high-p_{T} signatures of analyses that can be performed under high pile-up. The same run was used in the ALFA $\sqrt{s} = 8\,\mathrm{TeV}$ total cross-section measurement [73]. The peak instantaneous luminosity during this run was $1.4 \times 10^{30}\ \mathrm{cm}^{-2}\mathrm{s}^{-1}$. The integrated luminosity across the whole run is $24.11\,\mathrm{nb}^{-1}$, of which $16.75\,\mathrm{nb}^{-1}$ is suitable for use in this analysis, due to the analysis triggers being active and the beam conditions being optimised for diffractive physics [95].

During this run, a high β^* LHC quadrupole configuration was used, where β^* is a function of the beam emittance and is defined as the distance from the IP that the beam travels before the transverse radius of the beam doubles to twice its value at the IP. $\beta^* = 90\,\mathrm{m}$ for the run considered in this analysis, while the design $\beta^* = 0.55\,\mathrm{m}$ for LHC nominal running, due to the tight focussing of the beams close to the IP required to maximise the luminosity, resulting in a rapid dispersion of the proton beams. The high β^* configuration is particularly suited for measurements using the ALFA subdetectors as it enables the placing of the RPs close to the beam to detect small proton deflections from the main beam which would be contained within the beam envelope under regular conditions.

As a consequence of the high β^* configuration, the incident proton beams are less focussed than under normal operation and this results in a lower luminosity, and hence a low pile up, μ, of 0.08. This low pile up has the benefit of reducing the background from two overlapping physics events mimicking the SD signal. Of the maximum possible 2808 filled proton bunches in each LHC beam, only 108 are filled, with a spacing of at least 650 ns between each filled bunch. This low number of bunches enables a zero crossing angle to be used, compared to the nominal value at IP1 of $285\,\mu\mathrm{rad}$ [23]. The absence of a crossing angle means that the position

of protons in ALFA directly corresponds to the scattering angle, often referred to as 'parallel-to-point' optics [96]. A summary of the parameters used in the run analysed is provided in Table 6.1. More details on the 90 m running configuration used to collect the data used in this analysis are available at [96].

Parameter	**LHC design**	**Low luminosity**
Crossing angle [μrad]	285	0
β^* [m]	0.55	90
Bunch spacing [ns^{-1}]	25	650
Peak luminosity [cm^{-2}s^{-1}]	10^{34}	10^{30}
Pile up, μ, at IP1	30	0.08

Table 6.1: Comparison of main beam parameters between their design values for nominal running and the low luminosity run studied in the analysis presented within this document.

The ZDC was the only detector component not enabled during this low luminosity run. Information from the calorimeter is not used in this analysis as there were issues with the data taking, resulting in only noise distributions in the calorimeter components. The likely cause of this calorimeter issue is incorrect latency settings being used to align the timings of the ALFA triggers and calorimeter readout. The measurement performed in this analysis requires that the ALFA, ID and MBTS detectors were fully operational during data taking. The fraction of the run that is unusable due to one of these components being insensitive to new events being recorded due to reading out the detector information, referred to as 'dead-time', is 0.39%.

6.2.1 Monte Carlo Samples

The MC samples used within this analysis are listed in Table 6.2. All samples are produced using the PYTHIA8 generator, of which an overview is provided in Section 5.7. The A3 tune of this generator [97] is optimised using ATLAS measurements of charged particle distributions and the inelastic cross-section from early Run 2 data [98, 99] as well as Run 1 data [92, 100, 101, 102]. The NNPDF23LO proton PDF set is used [103]. The A2 tune [104] used ATLAS $\sqrt{s} = 7$ TeV Minimum Bias (MB),

leading track and Underlying Event (UE) measurements as inputs [100, 105, 106]. The A2 tune uses the MSTW2008lo proton PDFs [107]. A major difference between the A2 and A3 tunes is the modelling of the Pomeron flux factor, $F_{\mathbb{P}/p}(M_X^2, t)$. In the A2 tune, the SS model is used, built upon diffraction mediated by a Pomeron with $\epsilon = 0.0$ [108]. The A3 tune utilises the DL flux factor, which has been the most successful in modelling ATLAS diffractive measurements to date [93], using a Pomeron-based approach with $\epsilon = 0.07$. Both the A2 and A3 tunes set $\alpha' = 0.25\,\text{GeV}^{-2}$.

Process	Generator Tune	Diffraction Model	σ [mb]	Number of Events	Usage
SD	Pythia8 A3	DL	12.48	8.0 M	Unfolding
CD	Pythia8 A3	DL	1.211	0.5 M	Background subtraction
DD	Pythia8 A3	DL	8.254	1.0 M	Background subtraction
ND	Pythia8 A3		50.91	0.5 M	Background subtraction
EL	Pythia8 A3	DL	19.89	0.6 M	ALFA reconstruction efficiency
SD	Pythia8 A2	SS	12.48	0.4 M	Comparison

Table 6.2: Summary of Pythia8 MC simulation samples used within the analysis. The top four samples are used in the nominal analysis for signal and background modelling. The elastic scattering sample is labelled 'EL'.

6.3 Event Selection

6.3.1 Online Selection

Events are selected for use in an analysis in two ways: online and offline selection. The online selection is performed by the trigger and is of critical importance as events that are not selected by the trigger are not written to disk and thus are lost forever. The typical signature of an SD event is of a very forward proton continuing down the beam-pipe and a dissociated system with all or most of its constituents on the opposite side of the detector. This topology motivates the selection of analysis trigger to be, in ATLAS nomenclature for brevity, `L1_MBTS_2_A_ALFA_C`. Dissecting this trigger name: the '`L1`' indicates that it is a level-1 trigger, the '`MBTS_2_A`' states the requirement that two of the MBTS counters on the A-side of the detector have fired and the '`ALFA_C`' indicates that there must be a coincidence between the trigger

tiles of both detectors in an ALFA armlet on the C-side of the IP, ie. R1U or R1L. This trigger, along with the corresponding `L1_MBTS_2_C_ALFA_A` trigger, is prescaled by 10, meaning that only one in 10 triggered events are allowed to pass on to the L2 trigger. This prescale is necessary to prevent high dead-time in ALFA due to its limited readout rate. The L2 and EF triggers that receive the L1 accept signal from `L1_MBTS_2_A(C)_ALFA_C(A)` do not apply any further selection or prescale and all events passing the L1 trigger are written to disk. The effective integrated luminosity, accounting for prescales and dead-time, is $1.67\,\mathrm{nb}^{-1}$.

6.3.2 Offline Selection

Offline selection is applied at a later stage after the data has been written to disk with the general motive of removing background events while retaining signal events. This selection is separated into ALFA and central detector selection.

6.3.2.1 ALFA Selection

Track Candidate Selection: The tagging of the scattered proton in ALFA is the main differentiating analysis element that enables the measurement of the SD cross-section differentially in t and ξ, compared to previous LHC analyses that probe diffraction as a function of a rapidity gap size, relying on simulation to separate SD and DD. Consequently, it is required that a proton is reconstructed in exactly one of the four ALFA armlets. This requirement alone removes over 99.99% of ND interactions from the analysis according to the Pythia8 MC. A proton is reconstructed by pairing the best track candidate in the near detector of an armlet with the best track candidate in the far detector. The best track candidate is defined as the track with the most u+v layers that were utilised in its reconstruction. The track reconstruction algorithm forms tracks using overlapping hit fibres. Figure 6.3 displays the u and v fibre layer multiplicities observed in the run used in this analysis for an example RP. To minimise the number of fake tracks originating from

'cross-talk' between ALFA fibres and short tracks originating from showering within the ALFA stations, a track is required to have at least six u and six v fibre layers utilised in the track reconstruction algorithm. Six was selected as the first bin in which contributions from real, good quality tracks are visible in both the u and v layers. It is observed in both data and MC that less than 1% of events that pass the offline selection actually have more than one track that satisfies this criterion.

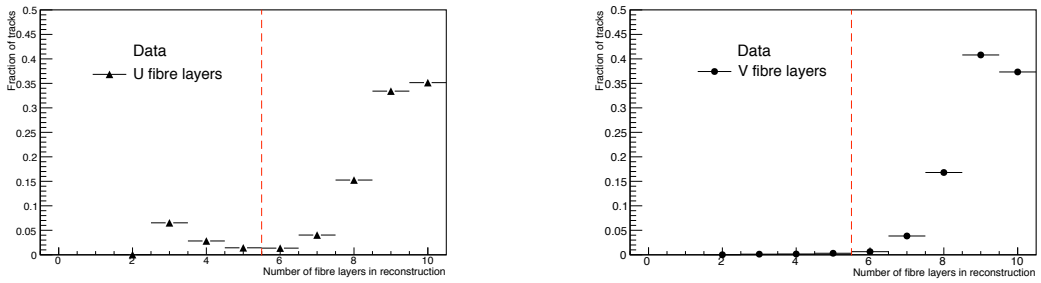

(a) u-fibres (b) v-fibres

Figure 6.3: Number of (a) u and (b) v fibre layers used in the reconstruction of each track in Roman pot B7L1U in the data sample, with no offline selection applied. At least six fibre layers in each plane are required in the offline selection, represented by the dashed red lines.

Despite being described as an 'edgeless detector', it was observed in previous analyses utilising the ALFA subdetector that optimal performance is not achieved along the edge closest to the LHC beam. To ensure maximal efficiency for the fibres, it is required that tracks are at least 90 μm from the physical detector edge. Another cut is applied in the vertical plane to account for the 'beam-screen shadow'. The beam-screen is responsible for shielding the quadrupoles. However, it also casts a shadow in the sensitive detector region in ALFA that is directly behind it along the path of the protons. Another effect of the beam-screen is that it can produce showering as protons interact with it. To avoid the mis-tagging of these scattering fragments as scattered protons it is required that reconstructed tracks are at least 1 mm away from the beam-screen shadow. The optimisation of these vertical selections was performed for the ALFA total cross-section analysis [73], and the values used are displayed in Table 6.3. For RPs above the beamline, the beam-screen and detector

edge cuts correspond to an upper and low limit, respectively. For RPs below the beamline, this is reversed.

Roman Pot	**Detector edge cut [mm]**	**Beam-screen shadow cut [mm]**
B7L1U	8.071	20.257
B7L1L	-8.152	-18.814
A7L1U	8.472	21.336
A7L1L	-8.477	-19.786
A7R1U	8.441	20.376
A7R1L	-8.369	-20.631
B7R1U	8.091	19.352
B7R1L	-8.109	-19.629

Table 6.3: Detector edge and beam-screen shadow vertical selection applied to each ALFA detector in LHC coordinates (origin is in centre of beam-pipe). The region between the detector edge and beam-screen cuts is the region used in the analysis.

To provide an appreciation for the location of the detector edge and beam-screen cuts, Figure 6.4 displays the track coordinates for the example of the B7L1U detector, overlaid with the positions of these cuts. The hit distribution displays that most tracks are situated at $x \sim 0\,\text{mm}$, which corresponds to protons with the beam energy (elastically scattered protons), or very close to the beam energy as is the case for low-ξ SD events. Due to the LHC optics, protons that have lost a significant fraction of their energy, such as high-ξ diffractively scattered protons, are detected in the positive x region. This smearing effect is visible in Figure 6.4. A summary of the selection of a track in an ALFA detector is displayed at the end of this section in Table 6.4.

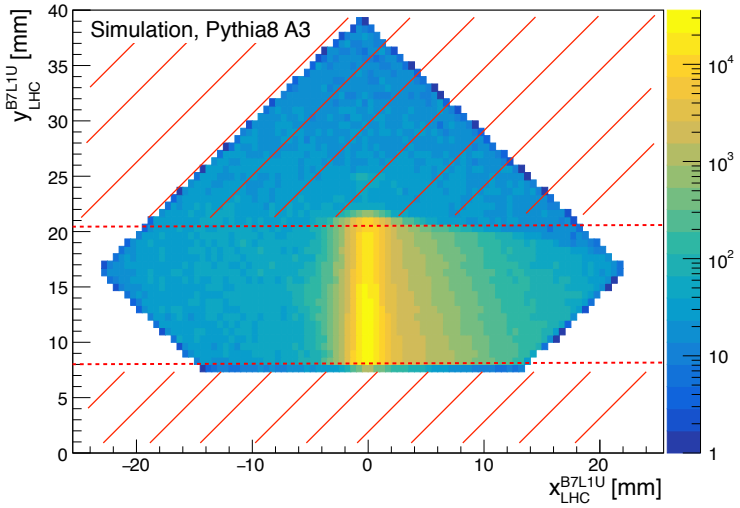

Figure 6.4: (x,y) coordinates for tracks collected in detector B7L1U in data which satisfy the standard analysis selection criteria with all ALFA track position requirements. The detector edge cut is represented by the lower red dashed line and the beam-screen cut is displayed as the upper red dashed line. The excluded region is represented by the red diagonal lines. x and y are displayed in LHC coordinates.

Proton Candidate Selection: A proton candidate is reconstructed by connecting two tracks, one in each ALFA detector that form an armlet. Further selection is applied to these proton candidates based on the mean x coordinate of the tracks in the near and far detectors, $\bar{x} = (x_{\text{near}} + x_{\text{far}})/2$, and the local angle in the x-plane between the two tracks, $\theta_x = (x_{\text{near}} - x_{\text{far}})/(z_{\text{near}} - z_{\text{far}})$. The distribution of these two variables is displayed in Figure 6.5 for the MC samples and in Figure 6.6 for the data sample. The diagonal correlation between these two variables is apparent for protons transported from the IP. As beam backgrounds are not simulated in the MC, there are very few MC events that do not show this correlation. The population located at $\bar{x} \sim 0$ in the data distribution that spans across the whole range of θ_x is due to showering in the near detector, thus $x_{\text{near}} \sim 0$ while x_{far} can take any value within the coverage of the ALFA detector. The beam-induced background, visible in the data but not MC distributions, stems from beam halo[2] and beam-gas interactions[3]. Beam halo is visible as horizontal bands with small local angles, as these are high energy particles. Beam-gas interactions are visible as the general uncorrelated background. From Figures 6.5c and 6.5d it can be seen that forward charged hadrons, such as those produced from dissociated protons in diffractive collisions and in the QCD hadronisation process in ND interactions, are more evenly distributed across the higher end of the diagonal correlation pattern than is the case for SD and CD.

[2] Charged particles that circulate within the beam-pipe which have departed from the main bunch structure.

[3] This can be elastic scattering between beam protons and residual gas in the beam-pipe which knocks protons out of the beam focussing, or inelastic scattering just upstream of the ALFA detectors which causes showers of energetic secondaries to hit the sensitive ALFA detector volume.

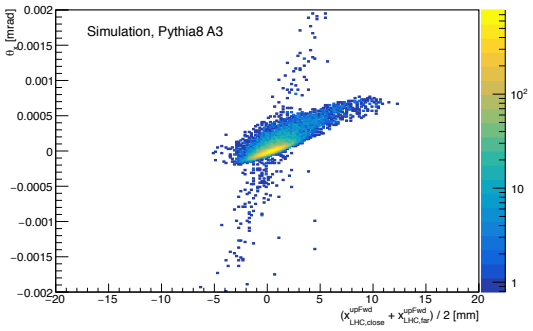

(a) SD MC before $\bar{x}$ and θ_x selection

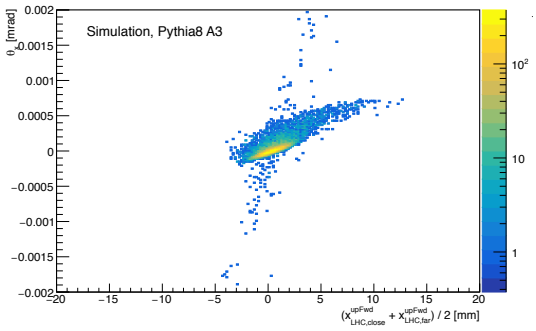

(b) CD MC before $\bar{x}$ and θ_x selection

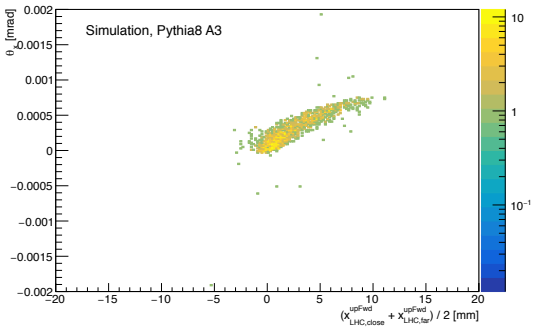

(c) DD MC before $\bar{x}$ and θ_x selection

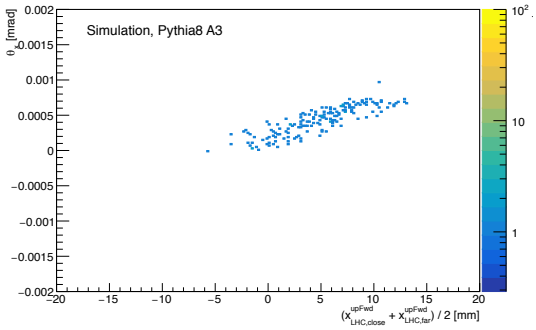

(d) ND MC before $\bar{x}$ and θ_x selection

Figure 6.5: $(\bar{x}\ ,\ \theta_x)$ distribution in the L1U armlet for all Monte Carlo samples after full analysis selection, excluding selection in the variables displayed. (a-d) display SD, CD, DD and ND simulations, respectively. Arbitrary units are displayed on the z-axes.

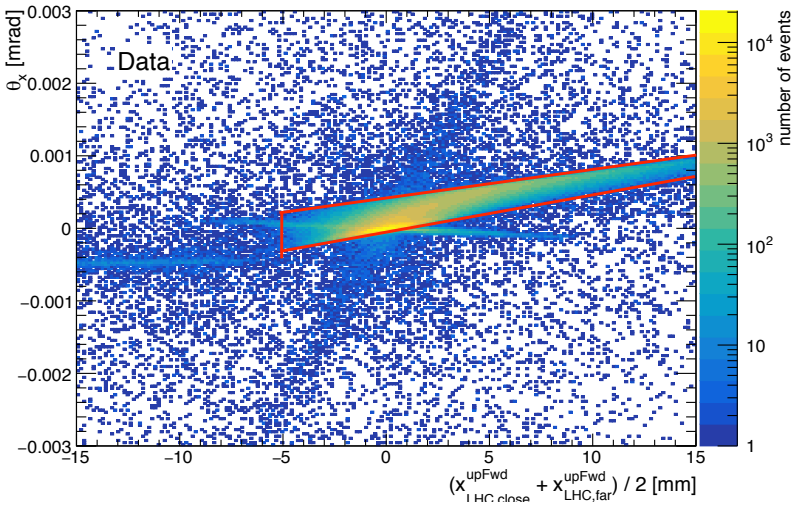

Figure 6.6: $(\bar{x}\ ,\ \theta_x)$ distribution in the L1U armlet for the data sample after full analysis selection, excluding selection in the variables displayed. Arbitrary units are displayed on the z-axes.

Figure 6.5a shows that diffractively scattered protons are concentrated about (0,0) in ($\bar{x}$,θ_x). Thus, to select a signal-enhanced region, a correlated double-Gaussian is fitted to the central region, following the approach taken in previous ALFA-based analyses [73], resulting in a elliptical selection region. The resultant elliptical contour follows the equation,

$$\frac{(\bar{x}-x_0)^2}{\sigma_x^2} - \frac{2\rho(\bar{x}-x_0)(\theta_x-\theta_0)}{\sigma_x\sigma_\theta} + \frac{(\theta_x-\theta_0)^2}{\sigma_\theta^2} = 1-\rho^2 \ , \tag{6.3}$$

where x_0 and θ_0 are the coordinates of the centre of the elipse, σ_x and σ_θ are the standard deviations of the elipse and ρ is the correlation coefficient[4]. The individual elipses resulting from the fits for each armlet are detailed in the ALFA selection summary at the end of this section in Table 6.6.

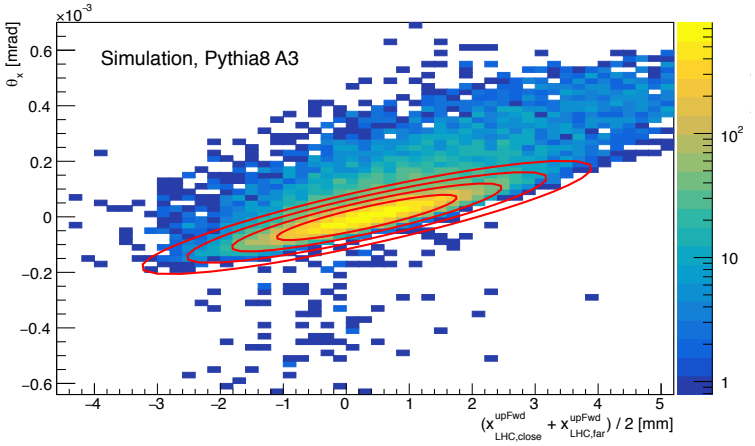

Figure 6.7: $(\bar{x}, \theta_x)$ distribution in the L1U armlet with contours of the 2σ, 3σ, 4σ, and 5σ elliptical selection zones displayed in red.

[4] ρ indicates how correlated the two variables are. $|\rho| \leq 1.0$. $|\rho| = 1$ indicates perfectly correlated or anti-correlated. $\rho = 0$ means there is no correlation between the two variables.

Figure 6.8 displays the distribution of SD MC events as a function of ξ_p for integer multiples of the standard deviations of the elipse. It can be seen that a very high signal acceptance is preserved in the low-ξ region for all cut values. The elipse bounded by 3σ is chosen for the analysis cut as it is observed to maintain a very high signal acceptance for events in the low-ξ region. Its lack of acceptance in the high-ξ region is not of concern as this region is completely overwhelmed by poorly constrained backgrounds and thus would not improve the measurement potential of the analysis.

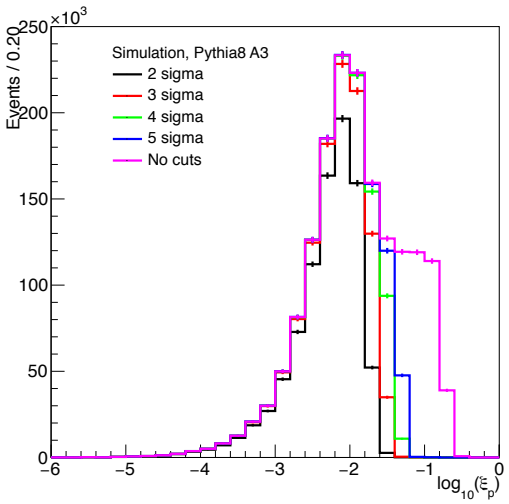

Figure 6.8: SD signal acceptance for 2σ, 3σ, 4σ, and 5σ elipses in $(\bar{x}, \theta_x)$, compared to no selection. Displayed as a function of the reconstructed level value of ξ_p

The offline selection criteria used to identify proton candidates are summarised in Tables 6.4, 6.5 and 6.6.

Criteria
$\geq 6u$ fibre layers used in track reconstruction
$\geq 6v$ fibre layers used in track reconstruction
$y \geq 90\mu$m from detector edge
$y \geq 1$mm from detector beam-screen

Table 6.4: Offline track selection in an individual ALFA detector. 'y' is the vertical coordinate of the reconstructed track.

Criteria
≥ 1 track in near station
≥ 1 track in far station
Elliptical 3σ requirement in $(\bar{x}, \theta_x)$

Table 6.5: Offline proton selection in an ALFA armlet.

Armlet	x_0 **[mm]**	θ_0	σ_x **[mm]**	σ_θ	ρ
L1U	$3.258 \cdot 10^{-1}$	$-2.338 \cdot 10^{-6}$	$7.154 \cdot 10^{-1}$	$4.086 \cdot 10^{-5}$	$8.760 \cdot 10^{-1}$
L1L	$3.089 \cdot 10^{-1}$	$-2.320 \cdot 10^{-6}$	$7.128 \cdot 10^{-1}$	$4.061 \cdot 10^{-5}$	$8.798 \cdot 10^{-1}$
R1U	$3.216 \cdot 10^{-1}$	$2.642 \cdot 10^{-6}$	$7.052 \cdot 10^{-1}$	$4.010 \cdot 10^{-5}$	$-8.780 \cdot 10^{-1}$
R1L	$3.333 \cdot 10^{-1}$	$2.216 \cdot 10^{-6}$	$7.106 \cdot 10^{-1}$	$4.025 \cdot 10^{-5}$	$-8.840 \cdot 10^{-1}$

Table 6.6: The elliptical selection in $(\bar{x}\ ,\ \theta_x)$ used for the proton selection in each armlet. $3\sigma_x$ and $3\sigma_\theta$ are used as the edge of the selected region.

6.3.2.2 Central Detector Selection

MBTS Offline Selection: The MBTS detector is well situated to detect the dissociated X system from a single diffractive event and in addition to its use as a trigger, it is also utilised in the offline selection in this analysis. As the MBTS detector consists of scintillator tiles, to be classified as 'hit' a counter must read out an offline charge greater than that of a threshold value. The threshold values are determined by a fit to the noise distribution of each individual counter. The noise distribution originates predominantly from the read-out electronics and is well described by a Gaussian fit approximately centred at zero, as displayed in Figure 6.9. The fit is constrained to a narrow region about the noise peak and the non-Gaussian shape due to real MBTS signals within this region is considered negligible. The fit is performed on a data sample selected by a random trigger and the sum of the MC samples, normalised to the data. The lack of a dedicated MC noise sample results in differing behaviour at larger offline charges, as the MC sample contains an actual proton-proton interaction in every event, while the data does not. From Figure 6.9a, it can be seen that there is a discrepancy between the data and MC noise distributions around $\mathrm{Q} = 0\,\mathrm{pC}$. This discrepancy stems from the MC response being tuned to early data and does not include the subsequent degradation in performance due to radiation damage to the scintillators and electronics. To overcome this potential

bias, different thresholds are used for data and MC. To ensure that noise is not being selected, the threshold is selected to be four standard deviations away from the Gaussian mean and is repeated for 3σ and 5σ to assess the systematic uncertainty, which is found to be very small in the final measurement. It is required that at least five MBTS counters on the opposite side to the tagged proton in ALFA are above the 4σ offline noise threshold as part of the event selection. Ideally, the analysis would be fully inclusive and no offline MBTS selection would be applied. However, it is observed that the efficiency of the signal trigger used in this analysis is below 50% for events with less than five counters hit, see Section 7.1, thus motivating this selection.

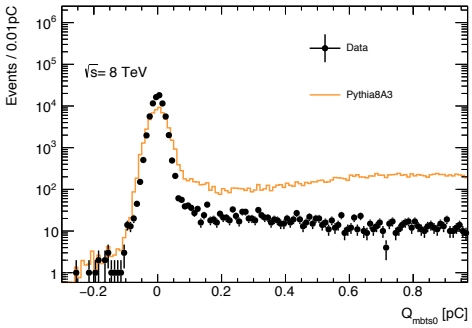

(a) Data vs MC noise distribution

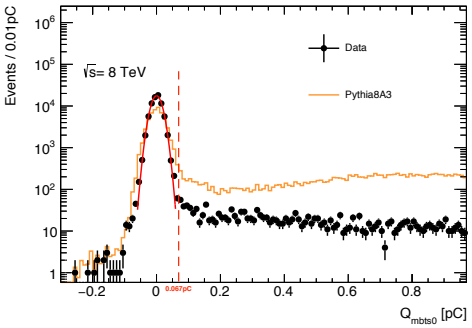

(b) Data noise peak fitted

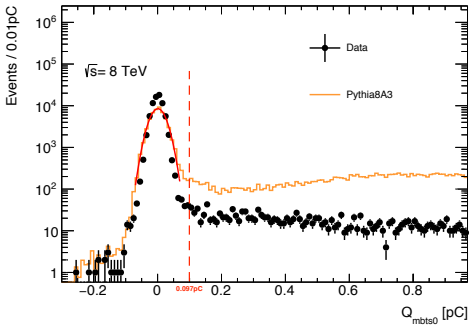

(c) MC noise peak fitted

Figure 6.9: Charge [pC] in the mbts0, an outer-ring C-side counter. Gaussians are fitted to the noise peak of (b) data ($\mu = 1.13 \times 10^{-4}$pC, $\sigma = 1.68 \times 10^{-2}$pC, threshold = 0.067pC) and (c) MC ($\mu = 8.73 \times 10^{-4}$pC, $\sigma = 2.41 \times 10^{-2}$pC, threshold = 0.097pC.).

ID Selection: Events passing all other offline selection criteria are also required to have a reconstructed Primary Vertex (PV) and at least one reconstructed track in the ID. Offline tracks are required to pass the following criteria, as recommended for ATLAS track-based analyses [100]:

- $|\eta| < 2.5$, i.e. within the inner detector acceptance.
- $p_{\mathrm{T}} > 200\,\mathrm{MeV}$, for consistency with the random 200 MeV track trigger used in several parts of the analysis (the only available 'random' trigger with significant statistics). Also motivated by consistency with previous rapidity gap analyses, where this threshold was used [92, 93].
- ≥ 1 hit in the pixel layers of the ID.
- ≥ 2, 4 or 6 hits in the SCT for tracks with p_{T} in the ranges: $100 \leq p_{\mathrm{T}} < 200\,\mathrm{MeV}$, $200 \leq p_{\mathrm{T}} < 300\,\mathrm{MeV}$ and $p_{\mathrm{T}} \geq 300\,\mathrm{MeV}$ respectively.
- $|d_0| < 1.5\,\mathrm{mm}$ and $|z_0 \cdot \sin\theta| < 1.5\,\mathrm{mm}$ relative to the PV to remove non-primary tracks. d_0 and z_0 are the transverse and longitudinal impact parameters with respect to the primary vertex.

For the calculation of ξ_{EPz}, tracks with p_{T} between 100 MeV and 200 MeV are also used to improve the resolution of this reconstruction method.

6.3.3 Fiducial Region

The fiducial region in which this measurement is performed is defined in terms of the phase space (t,ξ). The region of this phase space probed by this analysis is determined by the physical coverage of the ALFA RPs, the MBTS and the ID. The t sensitivity is restricted by the vertical coverage of the ALFA stations, as the parallel-to-point focusing directly correlates t with the vertical coordinate measured in ALFA. The lower ξ coverage is restricted by the MBTS and ID requirements, as very low ξ events result in very low mass diffractive systems that are entirely

contained at pseudorapidities above those of the MBTS coverage. The upper ξ acceptance limit stems from the ALFA selection, which is optimised for the signal to background ratio, as seen in Figure 6.8.

The fiducial region is chosen based on studies with the PYTHIA8 A3 SD MC sample by comparing the number of events before and after the reconstructed level selection is applied, as a function of the truth level variable. The truth level distributions are displayed before cuts in Figure 6.10.

Figure 6.10b displays the acceptance, defined as the fraction of events passing the reconstructed level selection as a function of the truth level variables, in ξ which is flat in the central region. The fiducial boundaries are chosen to be the points on the falling slope at which half of the maximum acceptance is still achieved: $-4.0 < \log_{10}\xi < -1.6$. After applying this selection, the t-acceptance is assessed and is displayed in Figure 6.10d. Mirroring the selection applied in previous ALFA analyses [73], 10% is selected as the lower acceptance threshold resulting in lower and upper $|t|$ fiducial boundaries of $0.016\,\mathrm{GeV}^2$ and $0.43\,\mathrm{GeV}^2$. The choice of fiducial region was also assessed using the PYTHIA8A2 SD MC sample and was found to be consistent. The two-dimensional acceptance is displayed in Figure 6.10f, displaying no significant correlation between the acceptances in t and ξ. Accordingly, the fiducial region used in the analysis is,

$$-4.0 < \log_{10}\xi < -1.6\ ,$$

$$0.016 < |t| < 0.43\ \mathrm{GeV}^2\ .$$

This ξ range corresponds to $80 < M_X < 1270\,\mathrm{GeV}$.

6.3.4 Resolution and Bin Widths

Owing to the high number of events in all analysis bins, the binning used for each variable is determined by the resolution; statistics are not considered. The bin width

is chosen to be approximately twice that of the standard deviation of a Gaussian fit to the difference between the truth and reconstructed level values for each variable, determined as a function of the truth level variable. An example of this Gaussian fit for the ξ_p variable is displayed in Figure 6.11a, with Figure 6.11b displaying the Gaussian width for all such fits across the full ξ range. Following this method, the bin edges for the four analysis variables are determined to be:

- $|t|$ bin edges [GeV^2]: 0.016, 0.024, 0.034, 0.049, 0.067, 0.087, 0.115, 0.150, 0.200, 0.280, 0.430.
- $\log_{10}(\xi_p)$ bin edges: -4.0, -3.3, -2.65, -2.15, -1.8, -1.6.
- $\log_{10}(\xi_{EPz})$ bin edges: -4.0, -3.5, -3.0, -2.4, -1.6.
- $\Delta\eta^F$ bin edges: 0.00, 0.25, 0.50, 0.75, 1.00, 1.25, 1.50, 1.75, 2.00, 2.25, 2.50, 2.75, 3.00, 3.25, 3.50, 3.75, 4.00, 4.25, 4.50, 4.75, 5.0.

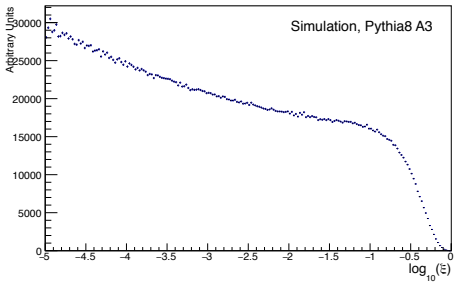

(a)

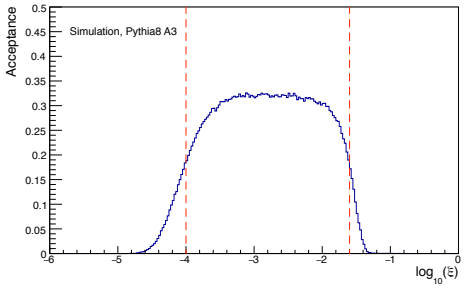

(b)

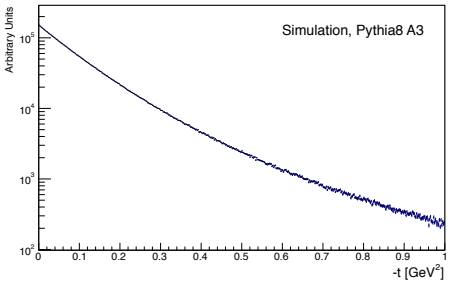

(c)

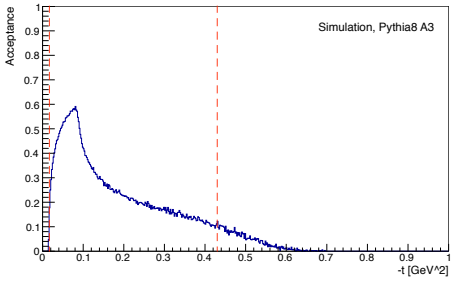

(d) Acceptance in $|\xi|$

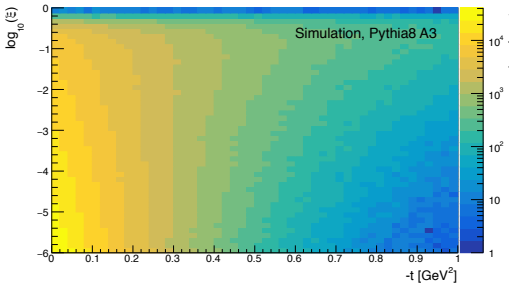

(e) Acceptance in $|t|$

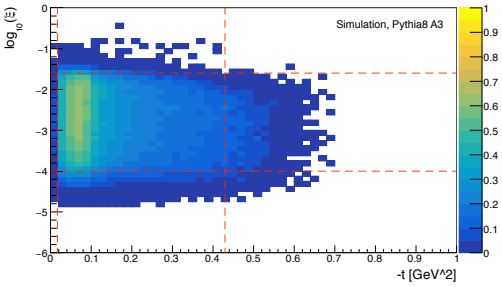

(f) 2D acceptance in $|t|$ vs ξ

Figure 6.10: Truth level (a) ξ distribution, (c) $|t|$ distribution and (e) $|t|$ vs ξ distribution. Acceptance as a function of true value of (b) ξ, (d) $|t|$ and (f) $|t|$ vs ξ, calculated from the PYTHIA8 A3 MC. The $|t|$ acceptance is calculated after the selection in ξ is applied. The dashed red lines indicate the choice of fiducial region.

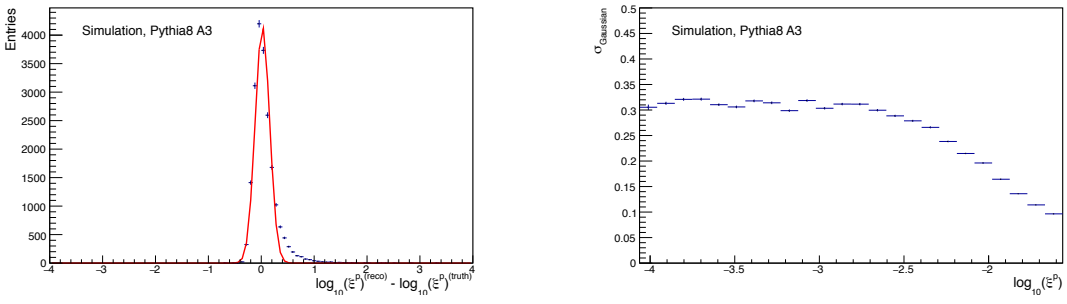

(a) $\log_{10}(\xi_p)$ resolution

(b) $\log_{10}(\xi_p)$ Gaussian widths

Figure 6.11: (a) An example bin within which the resolution is measured for use in determining the bin widths for the ξ_p variable. The resolution is calculated by subtracting the truth level ξ value from the reconstructed level ξ. (b) The width of each Gaussian is plotted as a function of the truth level value of ξ across the full ξ fiducial region. Obtained from PYTHIA8 SD MC.

CHAPTER 7

Efficiency Corrections

In this chapter, the procedure for calculating and applying corrections for the trigger and ALFA reconstruction efficiencies are detailed. The trigger is not simulated in the MC samples and the ALFA reconstruction efficiencies measured in the data and MC samples is observed to be marginally different, thus both must be accounted for.

7.1 Trigger Efficiency

The efficiency of the signal triggers, `L1_MBTS_2_A(C)_ALFA_C(A)`, are measured with respect to a random trigger which only has the requirement at the L2 trigger of a track with p_{T} above 200 MeV (corresponding to the offline analysis requirement). This trigger has a prescale of 576 combined across all levels of the trigger chain. This reference trigger is selected as it is the trigger with the least bias that still

has significant enough statistics with which to calculate the trigger efficiency. For comparison, the fully random bunch crossing trigger is prescaled by 190,080. The efficiency is calculated as follows,

$$\epsilon = \frac{\#\text{ events(passing offline selection } \cap \text{ reference trigger } \cap \text{ signal trigger (BP))}}{\#\text{ events(passing offline selection } \cap \text{ reference trigger)}} . \tag{7.1}$$

The signal trigger is evaluated before prescale (BP) to avoid biases from its prescale, utilising the trigger decision information that is stored for every event that is selected by any trigger chain. Binomial error propagation is used to evaluate the statistical uncertainties on the trigger efficiency as the events in the numerator are a subsample of the events in the denominator.

The trigger efficiency as a function of the number of MBTS counters on the non-proton side with a charge collected that is above the offline threshold is displayed in Figure 7.1. This distribution is used to decide the number of MBTS counters that are required in the nominal offline selection and thus no MBTS selection is applied. It can be seen that there is a very low trigger efficiency for events with less than two counters above the offline threshold, which is to be expected as the trigger requires two MBTS trigger counters to fire. The slow turn-on of the trigger efficiency as a function of MBTS counter multiplicity indicates that the offline signal threshold is not well correlated with that of the trigger. At least five counters above threshold are required in the main analysis selection so that the analysis is performed in the region with at least 50% trigger efficiency. The trigger efficiency cannot be considered constant as a function of all the analysis variables. Accordingly, the trigger efficiency is calculated and applied separately for each bin of the analysis when correcting the data for trigger efficiency effects. Figure 7.2 displays the trigger efficiencies as a function of the analysis variables.

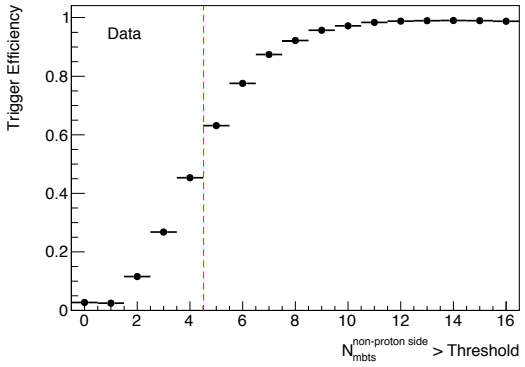

Figure 7.1: Signal trigger efficiency as a function of the number of MBTS counters on the opposite side of the detector to the ALFA-tagged proton that are above threshold. Statistical uncertainties are smaller than the data points. The offline selection cut is displayed by the dashed red line.

7.1.1 Systematic Uncertainty on Trigger Efficiency

As the reference trigger used to calculate the trigger efficiency in Equation 7.1 (referred to as the nominal trigger) is almost perfectly random, with only the requirement of one track, there is not expected to be any systematic bias or uncertainty associated with the calculation of the trigger efficiency. However, this assumption is tested by using an alternate reference trigger and repeating the efficiency calculation. The alternate reference trigger used is from the LUCID detectors which requires a trigger signal from either side of the IP. This trigger is selected for the cross-check as it is the trigger with the highest statistics that does not contain any geometrical overlap with the triggers or detector components utilised in the analysis; LUCID provides coverage in the range $5.6 \leq \eta \leq 6.0$. The trigger efficiency as a function of the analysis variables, and the number of MBTS counters hit on the non-proton side, is displayed in Figure 7.2. No significant discrepancies are observed between the nominal and LUCID triggered reference samples outside of statistical fluctuations, which are relatively large for the LUCID sample. Since there is no evidence for any systematic bias in the trigger efficiency determination, only the statistical uncertainty on the nominal trigger efficiency is included in the systematic

uncertainty. As with the efficiency itself, the uncertainty on the trigger efficiency is calculated and applied as a function of all the analysis variables.

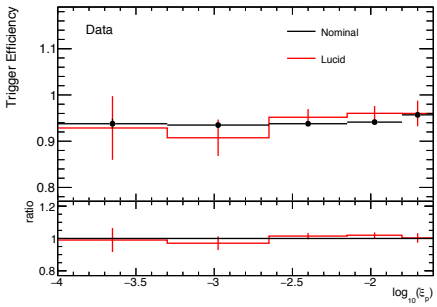

(a) Trigger efficiency as a function of $\log_{10}(\xi_p)$

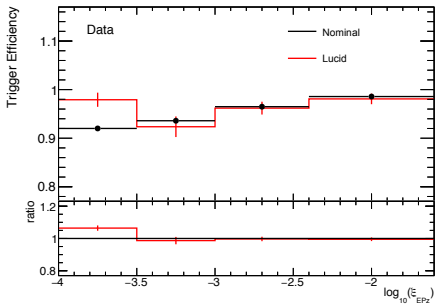

(b) Trigger efficiency as a function of $\log_{10}(\xi_{EPz})$

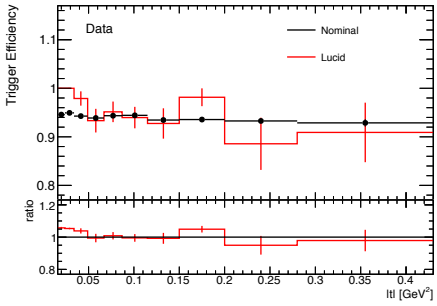

(c) Trigger efficiency as a function of $|t|$

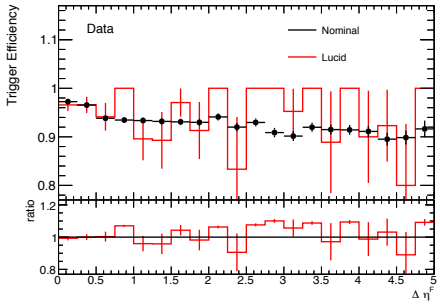

(d) Trigger efficiency as a function of $\Delta\eta^F$

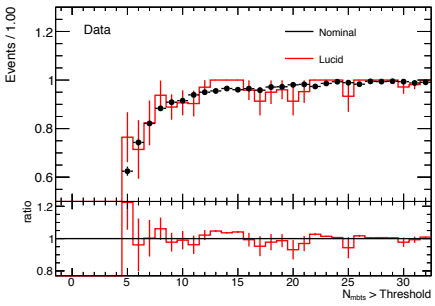

(e) Trigger efficiency as a function of MBTS multiplicity

Figure 7.2: The trigger efficiency using different reference triggers is displayed as a function of the four diffractive variables considered in this analysis, along with the number of MBTS counters above the offline threshold. Statistical uncertainties are displayed.

7.2 ALFA Reconstruction Efficiency

In a single diffractive event within the region of ALFA acceptance, it is expected that exactly one track is reconstructed in each of the near and far detectors of an armlet. Due to hadronic shower generation, pile-up and non-physics background it is possible for multiple particles to pass through the detectors, resulting in multiple tracks. In such cases, the track with the greatest number of overlapping fibres is used for the reconstruction of the proton in the armlet. When too much activity is detected in a single detector, it becomes possible that a track cannot be identified and reconstructed. By far the dominant source of such reconstruction inefficiencies is hadronic shower development. As the intrinsic reconstruction efficiency of ALFA for minimum ionising particles[1] was determined to be close to 100% in test beams [73], the reconstruction efficiencies derive entirely from the failure of the track reconstruction algorithm due to an overpopulation of the ALFA detector fibres. In this analysis, a data-driven tag-and-probe method is used to determine the ALFA reconstruction efficiency from elastic scattering events. This method is based on that previously used in ALFA elastic scattering analyses [41, 73] but adapted for the unique ALFA track and event selection utilised in this analysis. It was previously demonstrated that the reconstruction efficiency is uniform across the ALFA sensitive detector area [41].

Elastic scattering events are used as they produce two back-to-back protons with opposite momenta. Thus if an event is within ALFA's acceptance, four detectors should reconstruct tracks, resulting in two reconstructed protons. This back-to-back armlet layout of diagonally opposite armlets (L1U + R1L and L1L + R1U) is described as an 'elastic configuration'. When one of these protons is reconstructed it operates as a 'tag' and then it is possible to 'probe' whether the other proton is reconstructed in the opposite armlet in the elastic configuration. The possible scenarios for this probe armlet are neither, one, or both of its detectors reconstructing a track. The sum of the events when neither or only one of the near and far ALFA

[1] A particle which results in near the minimum possible ionisation and thus energy loss as it passes through a material.

detectors of the probe armlet reconstruct a track is referred to as N_{fail} while the number successfully reconstructing a proton in the probe armlet is referred to as N_{pass}. The efficiency of the track reconstruction is defined as,

$$\epsilon_{\text{rec}} = \frac{N_{\text{pass}}}{N_{\text{fail}} + N_{\text{pass}}} \ . \tag{7.2}$$

To select elastic events, dedicated elastic scattering triggers are required which require a trigger signal from both armlets within an elastic configuration. There triggers operate using an 'OR' decision between the near and far triggers in each armlet. To increase the purity of elastic scattering events in the sample, it is required that each of the four individual detectors in the elastic configuration also passed its trigger decision. This mirrors the central analysis requirement that the near and far detector are both required to have triggered an event. To measure the efficiency of this analysis, the track and proton selection criteria in Section 6.3.2.1 are used to identify the 'tag' armlet, and then the same criteria are checked against on the 'probe' armlet. In Figure 7.3, armlets L1L and R1U combine to form an elastic configuration as they are back-to-back, with L1L constituting the tag and R1U being the probe armlet.

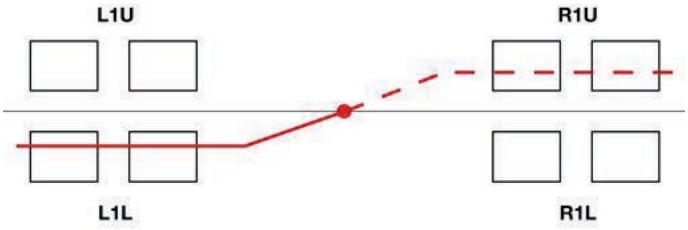

Figure 7.3: A simplified elastic interaction demonstrating the tag and probe method used for ALFA reconstruction efficiency calculations. L1L is identified as the 'tag' and the R1U armlet is 'probed'.

An additional requirement of at least 12 fibres hit is applied to both of the detectors in the probe armlet to ensure that the elastic proton was within the acceptance of the detector and thus enough fibres were hit to enable the reconstruction of a track. These events where the proton only 'scratches' the detector must be removed as they are acceptance issues and are not the concern of the efficiency calculation. The limit

of 12 is selected as the nominal analysis track selection requires at least six fibre layers to be hit in both the u and v planes, thus a track cannot be reconstructed with less than 12 fibres.

To further reduce the number of SD events in the sample, a veto is applied on the trigger decisions from several triggers that can be fired by SD events. These triggers are the most inclusive triggers with the lowest possible threshold in the MBTS, LUCID and calorimeter detector systems. These triggers should not be fired by elastic scattering interactions that are within the acceptance of ALFA.

The process is also performed on simulated elastic scattering MC events that use the same optics and ALFA simulation as the main MC samples considered in this analysis, thus ensuring the reconstruction efficiency should be the same. Due to the absence of trigger simulation in the MC samples, the same trigger requirements cannot be applied. However, this does not affect the procedure as the trigger vetoes are designed to remove SD background, which is obviously not present in the elastic MC, and the offline selection applied in each detector is much tighter than the ALFA trigger requirements.

It is possible for an elastic scattering event to pass the full offline proton selection in the tag armlet and yet to fail the elipse selection applied on $(\theta_x, \bar{x})$ in the probe armlet. This occurrence can be due to the event being on the edge of acceptance or because of interactions of the proton in the inner ALFA detector thus perturbing its path and reconstructed value of θ_x. Events of this type would incorrectly be classified into N_{fail}, even thought the reconstruction algorithm has not failed to identify a track. To avoid this misclassification, events that would be included in N_{fail} but have a reconstructed track in each detector in the probe armlet that satisfies the offline track selection are removed from the sample. They are removed rather than being classified into N_{pass}, despite their successful reconstruction, as this efficiency study aims to measure the efficiency for reconstruction within our event selection, not for all ALFA tracks. As these tracks that fail the event selection may also cause showering that then results in an event that is classified as a failed

reconstruction, it is necessary to remove some N_{fail} events to account for this. This is achieved by assuming a 90% reconstruction efficiency for these events and thus the number equal to 10% of the number of events with a track in each detector in the probe armlet which fail reconstruction are removed from the total value of N_{fail}. The 90% efficiency is used as it is close to the trigger efficiency. A conservative uncertainty of $\pm 10\%$ is applied in Section 7.2.2 and is observed to have little effect on the precision of the measurement. These events with reconstructed tracks that fail the $(\theta_x, \bar{x})$ selection constitute less than 3% of events in data and MC.

7.2.1 Uncorrelated Background

The rate of background that remains after the elastic selection arising from combinations of multiple beam-halo and/or SD interactions arranged in an elastic configuration is estimated using information from the remaining armlets of an already identified elastic scattering event. To avoid confusion with the probe armlet these armlets are referred to as the 'queried' armlets. Two distinct backgrounds are defined, referred to as 'pass' background and 'fail' background for events where the queried armlet has at least 12 fibres hit and either successfully or unsuccessfully reconstructs an offline track. To remove events caused by the pile-up of two or more elastic scattering events, which is dominantly seen in the four-proton event topology rather than the three-proton, it is required that less than 12 fibres are hit in each detector in the armlet diagonally opposite to the queried armlet. An example of this configuration in the context of Figure 7.3 is that the L1L and R1U armlets both reconstruct an offline proton, L1U is required to not have 12 or more fibres hit in either the near or far detector and R1L is queried to measure the background rate. This procedure is repeated for all armlets. The measured rate of events with at least 12 fibres hit in each detector without a reconstructed proton and that of successful proton reconstruction are then the rate of fail and pass backgrounds in the queried armlet, respectively. To enable proper comparison, the same track and proton definitions are used as in the main analysis. This method assumes that the

rate of halo background and SD interactions is independent of the primary elastic scattering process. This method also accounts for elastic scattering events in which one of the protons is within the ALFA acceptance while the other is not, as such an event would still require another background process in coincidence to recreate the elastic two-proton signal.

The probabilities of pass and fail backgrounds in each armlet due to uncorrelated halo and SD protons for a random bunch crossing are displayed in Table 7.1.

Armlet	N^{Events}	$N^{\text{Events}}_{\text{pass}}$	$N^{\text{Events}}_{\text{fail}}$	$\mathbf{P}(^{\text{Background}}_{\text{pass}})$ **[$\times 10^{-3}$]**	$\mathbf{P}(^{\text{Background}}_{\text{fail}})$ **[$\times 10^{-3}$]**
L1U	65272	69	8	1.01	0.12
L1L	67929	61	17	0.90	0.25
R1U	67929	63	17	0.93	0.25
R1L	65284	67	12	1.03	0.18

Table 7.1: Probability of random signals in an armlet due to an uncorrelated background in any given bunch crossing.

The values in Table 7.1 can be combined to form the probabilities of each of the possible armlet-pair hit patterns being produced by background, outlined in Table 7.2. When multiplied by the number of bunch crossings in the run, this results in the number of background events for each specific armlet hit pattern in each elastic configuration. It can be seen that very few events are expected where the elastic signal is recreated by uncorrelated background events.

Armlet pair pattern	**P(background) [$\times 10^{-6}$]**	**N(background)**
L1U_{pass} & R1L_{pass}	1.08	74
L1U_{pass} & R1L_{fail}	0.19	13
L1U_{fail} & R1L_{pass}	0.13	9
L1L_{pass} & R1U_{pass}	0.83	57
L1L_{pass} & R1U_{fail}	0.22	15
L1L_{fail} & R1U_{pass}	0.23	16

Table 7.2: Probability per bunch crossing that different armlet pass/fail reconstruction patterns form a background in the ALFA reconstruction efficiency calculation. Pass indicates that a proton was reconstructed in the armlet, fail indicates that at least 12 fibers were hit in both detectors in the armlet but no proton was reconstructed. In the final column, the probabilities are multiplied by the number of bunch crossings in the analysed run.

The background contribution is subtracted within the efficiency calculation by mod-

ifying Equation 7.2 to,

$$\epsilon_{\text{rec}} = \frac{N_{\text{pass}} - N_{\text{pass}}^{\text{Background}}}{(N_{\text{fail}} - N_{\text{fail}}^{\text{Background}}) + (N_{\text{pass}} - N_{\text{pass}}^{\text{Background}})} \,. \tag{7.3}$$

The efficiency, ϵ_{rec} obtained for each armlet is given in Table 7.3. In the elastic

Armlet	ϵ_{Data}	$\epsilon_{\text{Elastic MC}}$
L1U	0.943 ± 0.001	0.949 ± 0.001
L1L	0.912 ± 0.001	0.918 ± 0.001
R1U	0.925 ± 0.001	0.941 ± 0.001
R1L	0.918 ± 0.001	0.939 ± 0.001

Table 7.3: ALFA armlet efficiency calculated from an elastic scattering dominated data sample and MC samples. The uncertainties displayed are statistical only.

scattering MC, there is no background and the armlets outside of the identified elastic configuration armlets are always found to be empty; thus no background subtraction is performed.

7.2.2 Systematic Uncertainty

The systematic uncertainty on the reconstruction efficiency is estimated by varying the event selection cuts that are applied to select the elastic events. Where possible, this has been kept as close as possible to the strategy adopted in previous ALFA analyses [41, 73]. The sources of systematic uncertainty considered are: the beam-screen and detector edge cuts, the θ_x vs $\bar{x}$ elliptical selection on proton candidates, the fibre layer multiplicity required in the probed armlets to define activity rather than just a scratch, the number of failed reconstructed events removed due to showering initiated by tracks that would lie outside of the elliptical selection and the SD/halo uncorrelated background determination. Each cut is varied up and down (relaxed and tightened), and the upwards and downwards deviations from the nominal efficiency are taken to be the uncertainty from a given source. The upwards and downwards uncertainties from all sources are summed in quadrature and then the larger of the two sums is taken to be the systematic uncertainty. More detail of the individual sources is given below.

To maintain consistency between the definition of a scratch and a track, when the number of fibres hit in a probed armlet is reduced to 8 (nominally 12), the number of u and v fibre layers required to define a track is reduced to $4u$ and $4v$ (nominally $6u$ and $6v$). If this were not performed, it would result in events where activity is defined in an ALFA detector, but not enough fibres would be hit for it to be possible to reconstruct a track, thus biasing the measurement. It is not necessary to perform such an alteration to the track definition in the upwards shift of this uncertainty (to 16 fibres) as this is enough fibres with which to reconstruct a track in a detector.

The number of SD and halo uncorrelated background events is conservatively varied between 0% and 200% of its nominal value and due to its small size, the uncertainty resulting from this is not significant. The assumed reconstruction efficiency of tracks falling outside of the elliptical selection in θ_x and $\bar{x}$ is varied between the nominal 90% to its theoretical maximum, 100%, and the systematic lower variation, 80%. The variations used in previous ALFA analyses for the beam-screen and detector edge selection are used here. The size of the ellipse used to select protons in the (θ_x, $\bar{x}$) correlation is varied from 3σ to 2σ and 4σ. The amount each selection criteria is varied by is summarised in Table 7.4.

Cut	**Nominal Value**	**Lower Variance**	**Upper Variance**
Δy beam-screen	1mm	0mm	2mm
Δy detector edge	90μm	0μm	180μm
N_{fibres} in probe armlet	12	8	16
N_σ applied in elipse	3.0	2.0	4.0
ϵ_{rec} outside of ellipse	90%	80%	100%
Background rates	measured rate, R	0 × R	2 × R

Table 7.4: Amount by which each selection criterion was varied to assess the systematic uncertainty on the ALFA reconstruction efficiency. The uncertainties considered are: The vertical cut to exclude the beam-screen shadow (Δy beam-screen), the vertical cut to exclude the detector edge region (Δy detector edge), the number of fibres required to be hit in each detector in a probe armlet (N_{fibres} in probe armlet), the number of standard deviations used in defining the elliptical selection in θ_x and $\bar{x}$ (N_σ applied in elipse), the assumed reconstruction efficiency of tracks that fall outside of the elliptical selection in θ_x and $\bar{x}$ (ϵ_{rec} outside of elipse) and the background rates of halo/SD mimicking the elastic topology (Background Rates).

Table 7.5 details the contribution to the total uncertainty from each systematic

variation. It can be seen that there are no overly dominant sources of systematic uncertainty.

	L1U	**L1L**	**R1U**	**R1L**
Δy beam-screen:				
Data	+0.0018 -0.0011	+0.0092 -0.0082	+0.0023 -0.0019	+0.0078 -0.0070
MC	+-0.0006 -0.0027	+0.0154 -0.0088	+0.0026 -0.0022	+0.0081 -0.0159
Δy detector edge:				
Data	+0.0056 -0.0063	+0.0051 -0.0060	+0.0060 -0.0044	+0.0046 -0.0056
MC	+0.0050 -0.0042	+0.0057 -0.0050	+0.0042 -0.0043	+0.0030 -0.0053
N_{fibres} in probe armlet:				
Data	+0.0003 0.0012	+0.0006 0.0022	+0.0003 0.0007	+0.0006 0.0012
MC	+0.0061 -0.0087	+0.0074 -0.0127	+0.0054 -0.0063	+0.0090 -0.0131
N_σ applied in elipse:				
Data	+0.0005 -0.0049	+0.0013 -0.0083	+0.0011 -0.0075	+0.0015 -0.0094
MC	+0.0001 -0.0014	+0.0002 -0.0022	+0.0002 -0.0015	+0.0002 -0.0016
ϵ_{rec} outside of elipse:				
Data	+0.0029 -0.0029	+0.0026 -0.0025	+0.0025 -0.0025	+0.0023 -0.0023
MC	+0.0014 -0.0014	+0.0012 -0.0012	+0.0013 -0.0013	+0.0015 -0.0015
Background Rates:				
Data	+0.0001 -0.0001	+0.0001 -0.0001	+0.0001 -0.0001	+0.0001 -0.0001
MC	+0.0000 0.0000	+0.0000 0.0000	+0.0000 0.0000	+0.0000 0.0000
Total syst. uncertainty:				
Data	+0.0067 -0.0086	+0.0112 -0.0134	+0.0070 -0.0092	+0.0096 -0.0132
MC	+0.0080 -0.0102	+0.0180 -0.0164	+0.0074 -0.0081	+0.0126 -0.0214

Table 7.5: Table of absolute contributions to the systematic uncertainty on the ALFA reconstruction efficiency, ϵ_{rec}, for each armlet. Data and MC uncertainties are displayed on separate lines.

The main difference between the data and MC systematic uncertainties is the number of fibre hits required in the probed armlet (nominally 12 in the near and far station). The data displays very little variance with this systematic variation while the MC varies by $\sim 1\%$. The cause of this deviation is the noise distribution in the MC which appears to be of Gaussian shape centred around 10 fibres. Figure 7.4a displays the number of hit fibres in the probe armlet in data and MC before any requirements are made on the reconstructed tracks or the fibres hit, and this noise distribution is clearly visible in the MC. In Figure 7.4b, the number of fibres hit in a spectator armlet (not the tag or the probe armlet) is displayed for elastic scattering MC. This displays this clear noise peak centred at the same number of fibres as the structure observed in the probe armlet for the elastic scattering MC.

It should be noted that this noise distribution never results in a reconstructed

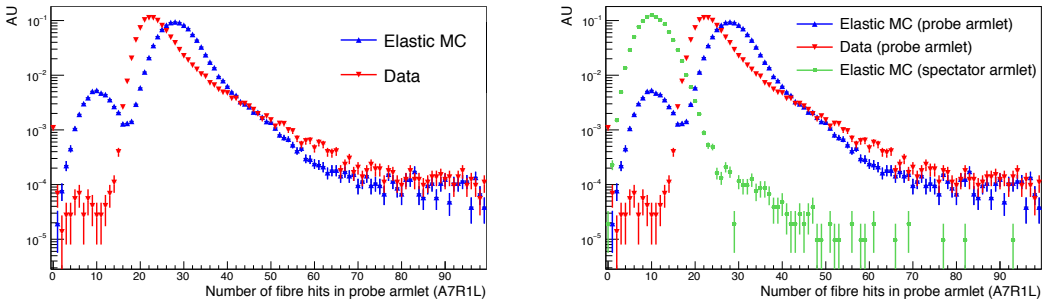

(a) Number of fibres hit in probe armlet (b) Spectator armlet added to display noise

Figure 7.4: Number of fibres hit in probe armlet in data (red) and elastic scattering MC (blue). The noise distribution from a spectator armlet in elastic scattering MC is also displayed (green). All distributions are normalised to one.

track and only impacts the analysis in this efficiency calculation. This conclusion is reached by observing that the spectator armlets do not have a reconstructed proton in any of the elastic scattering MC events. No noise peak is observed in data due to the requirement that both detectors in the probe armlet were successfully triggered, thus ensuring a minimum level of activity. As the noise and signal distributions overlap, it is decided to keep the cut on the number of fibres at 12 so as to not unnecessarily remove any of the signal distribution. This results in an overestimation of the systematic uncertainty on the ALFA reconstruction efficiency in MC. However, this is deemed acceptable as it is not a limiting source of systematic uncertainty and it ensures that all events with particles passing through the detectors in the probe armlet are used in the efficiency calculation.

The final ALFA reconstruction efficiency for each armlet is listed in Table 7.6, together with the statistical and systematic uncertainties. The systematic uncertainty is taken as the maximum of the up and down total systematic uncertainties, summarised in Table 7.5. It can be seen that the data and MC have similar values for the efficiency, with the MC having slightly larger uncertainties.

	L1U	**L1L**	**R1U**	**R1L**
ϵ_{rec}				
Data:	0.9427	0.9123	0.9247	0.9179
MC:	0.9491	0.9177	0.9411	0.9391
Statistical uncertainty				
Data:	0.0009	0.0011	0.0010	0.0010
MC:	0.0007	0.0009	0.0008	0.0008
Systematic Uncertainty				
Data:	0.0086	0.0134	0.0092	0.0132
MC:	0.0102	0.0180	0.0081	0.0214
Total Uncertainty				
Data:	0.0086	0.0134	0.0093	0.0133
MC:	0.0103	0.0180	0.0082	0.0214

Table 7.6: ALFA reconstruction efficiency for each armlet, ϵ_{rec} with statistical and systematic uncertainties listed. Values displayed for both data and MC.

7.2.3 Efficiency Correction

To correct for the effects of the differing reconstruction efficiency in data and MC, the MC is weighted by the fraction $\epsilon^{\text{data}}/\epsilon^{\text{MC}}$. The factors used are listed in Table 7.7. This results in, by construction, the same reconstruction efficiency in the data and the MC, so that the global correction for this inefficiency can be handled within the unfolding procedure. The values used to assess the systematic uncertainties are detailed in Section 9.2.6 and they are propagated through to an uncertainty on the efficiency correction factor.

Armlet	$\boldsymbol{\epsilon^{\text{data}}/\epsilon^{\text{MC}}}$
L1U	0.9933
L1L	0.9941
R1U	0.9826
R1L	0.9774

Table 7.7: Event weights applied to MC to correct for differences from the data in the ALFA reconstruction efficiency.

CHAPTER 8

Background Determination

This chapter details the background sources that are identified and how they are accounted for within the measurement of the SD cross-sections.

8.1 Simulated Backgrounds

The physics processes which can pass the analysis selection and enter the analysis as a background source can be divided into CD, DD and ND categories. CD interactions produce two forward protons which can fall into the ALFA acceptance and DD and ND collisions can produce forward hadrons through the evolution of showering of their final states. These processes can also satisfy the central detector requirements, producing particles in the ID and MBTS coverage. The physics background sources are accounted for by means of the Pythia8 A3 tune MC simulations introduced in 6.2.1.

Background	Cross-section [mb]	Fractional Acceptance
ND	50.91	$\ll 0.001$
DD	8.254	0.001
CD	1.211	0.086

Table 8.1: Fraction of events for each background MC sample passing the offline selection. The cross-section according to the steering used in PYTHIA8 is also displayed.

Table 8.1 displays the fractions of events passing the full selection criteria for each background MC sample. It can be seen that there is only a significant contribution from CD events, with DD and ND being negligible sources of background. These background sources are evaluated bin-by-bin. The contribution from CD events is given further consideration in Section 8.5.

8.2 Data-Driven Background

The dominant source of background in this analysis is caused by the coincidence of two uncorrelated processes, one producing a signal in ALFA and one emulating the dissociative system of an SD event and satisfying the central detector requirements. An example of such a coincidence is an elastic scattering event where only one of the outgoing protons is reconstructed and an ND event producing many charged particles within the ID and MBTS coverage. The background constrained within this section is referred to as the 'Overlay Background' (OB) as it involves the overlay of ALFA samples with central detector information.

The OB is assessed through an inclusive method accounting for all possible combinations of central detector and ALFA backgrounds. An ND-enriched data sample, in which little or no ALFA activity due to the proton-proton collision is expected, is selected starting from the random trigger with track sample described in Section 7.1. The offline selection criteria applied to this sample to remove events that may produce protons within the ALFA acceptance correlated with the central detector activity are:

- all 32 MBTS counters above offline threshold,
- no large rapidity gaps on either side of the ID, $\Delta\eta^A < 0.5,\ \Delta\eta^C < 0.5$.

It is estimated from MC simulations that this sample is enriched to consist of 99.3% ND events with only a 0.7% impurity from SD events.

Within this ND-enriched sample, the number of protons passing the ALFA offline requirements is counted. The probabilities of 0,1,2,3 or 4 protons are displayed in Table 8.2. These probabilities are used to determine how often central detector activity from other (MC-modelled) processes are expected to have additional uncorrelated ALFA activity.

Number of 'overlaid' protons	**Probability (%)**
0	98.498
1	0.767
2	0.732
3	0.002
4	0.001

Table 8.2: Fraction of events in the highly ND-enriched sample with different numbers of protons reconstructed in ALFA.

The central detector component of the uncorrelated background is modelled using the MC samples. Events which pass all the analysis event selection except that they have no protons and thus fail the overall selection are selected to form the 'MC background template'. This sample is weighted by 0.00767, the probability of any event having one unassociated background proton, and forms the background contribution which is subtracted from the raw data in distributions derived from the inner detectors and the MBTS systems (ξ_{EPz} and $\Delta\eta^F$).

The proton kinematics (t and ξ_p) from events with one proton in the ND-enriched data control sample are used to form the t and ξ_p 'data background template' shapes. The data background template is normalised to the MC background template.

To correct for the 0.7% SD impurity within the ND-enriched control region, the MC samples are used to subtract a contribution from the background templates. It is

calculated from the SD MC that 8.8% of the sample where exactly one proton is reconstructed stems from the SD contamination. In the data background template, the SD MC distribution (for events satisfying the ND enriched sample selection criteria) is used to subtract this contribution. In the MC background template, the proton is not correlated to the ID distributions, thus the background sample can simply be scaled down to account for the 8.8% contamination. The effect of this correction is dwarfed by the uncertainty stemming from the OB, described in Section 8.4.

It is also possible for an event that passes the analysis event selection to be in coincidence with a background proton. To account for this effect, events that pass the analysis selection are weighted by a factor of 0.985, the probability of no background protons being detected, see Table 8.2, resulting in a 1.5% reduction in the predicted SD signal.

8.3 Control Plots

Control plots are displayed in Figure 8.1 for all the diffractive variables considered within this analysis (ξ_p, ξ_{EPz}, $|t|$ and $\Delta\eta^F$) as well as ID track and MBTS multiplicities, which are of interest in soft-physics analyses. The MC samples are normalised to the default Pythia8 cross-sections. It is observed in all distributions that the sum of the signal and background is greater than that measured in the data. The shape distributions are well modelled for all variables except for the MBTS and ID track multiplicities, which are highly sensitive to hadronisation modelling. This number of tracks discrepancy is consistent with a previous ATLAS measurement which observed that all considered Pythia8 tunes predicted an excess of low multiplicity events and a deficit of high multiplicity events [78]. Pythia8 with the DL diffraction model was observed to provide the best description of all MC tunes considered in [99]. However, differences of approximately 50% were still observed within this tune and thus the discrepancies observed in Figure 8.1e and 8.1f are not

unexpected or considered problematic.

In Figure 8.2, for visual purposes, the SD cross-section is adjusted to 8 mb, the approximate extrapolated value calculated in this analysis, and the control plots are reproduced. Of course, σ_{SD} cannot simply be changed without impacting the other cross-sections such as the total inelastic cross-section; this is only done in this section to demonstrate the normalisation issue and good shape agreement.

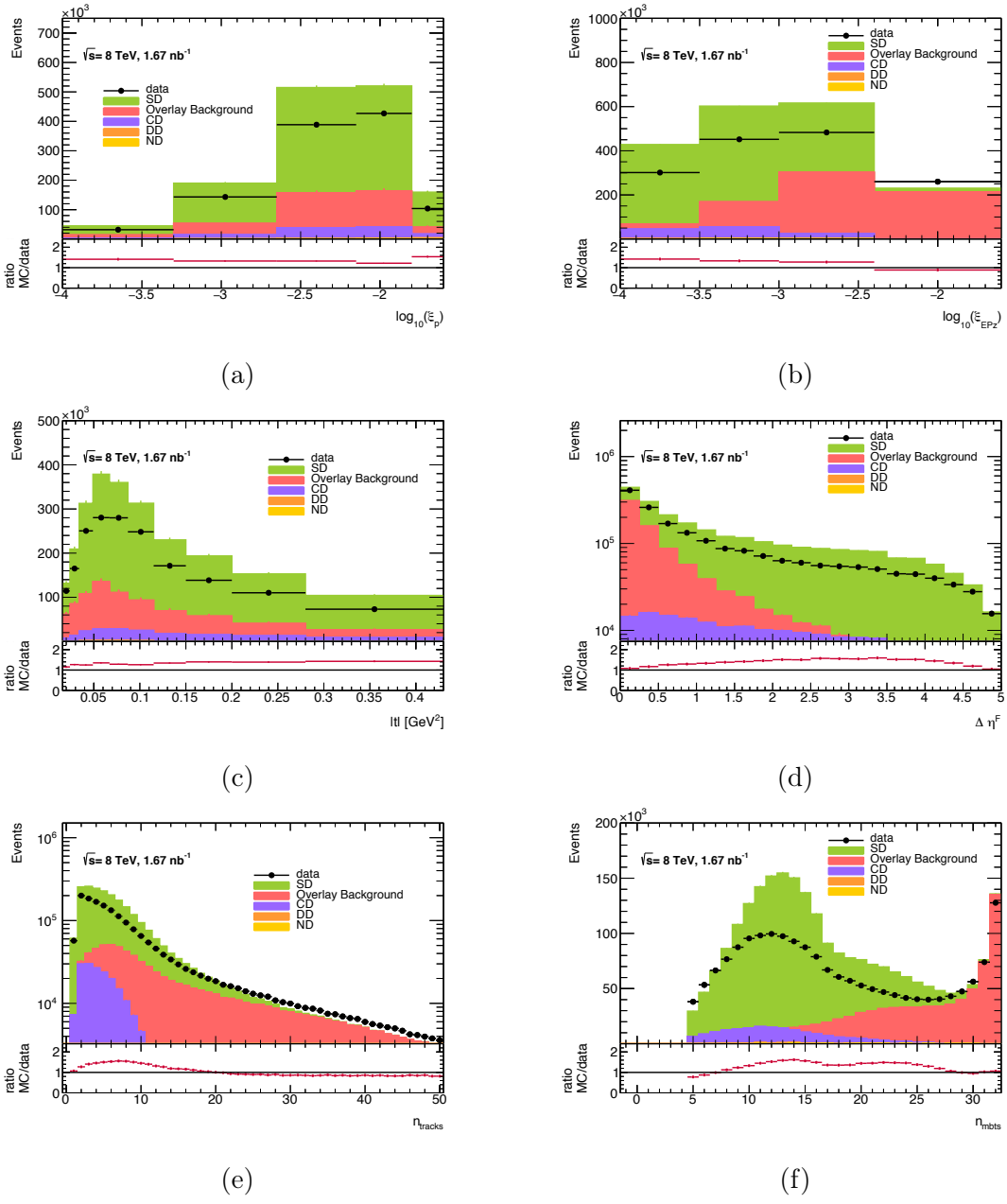

(a) (b) (c) (d) (e) (f)

Figure 8.1: Uncorrected measured distributions of (a) $\log_{10}\xi_p$, (b) $\log_{10}\xi_{EPz}$, (c) $|t|$, (d) $\Delta\eta^F$, (e) Number of MBTS counters above offline threshold and (f) charged particle multiplicity in the ID. Statistical uncertainties are displayed.

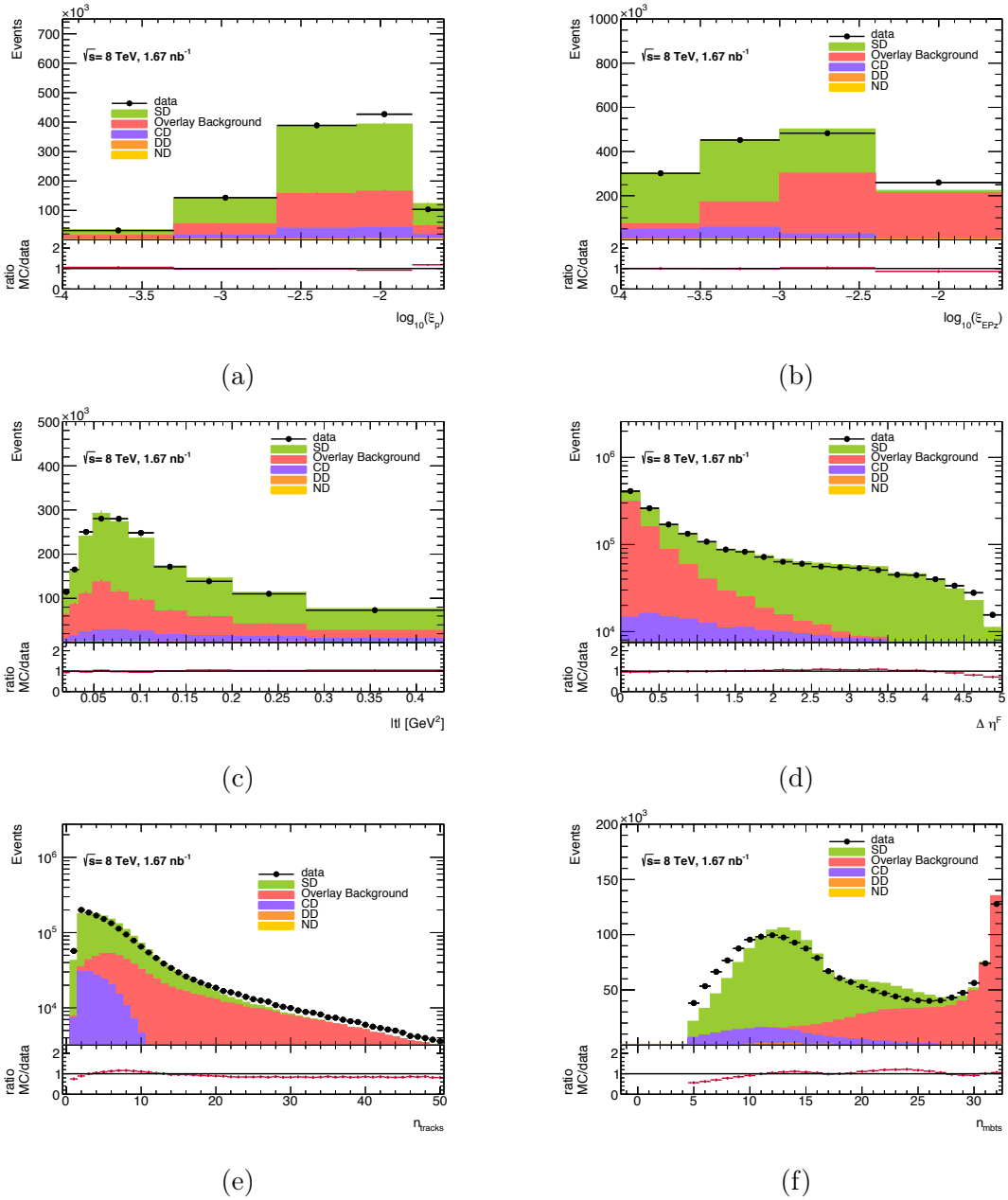

Figure 8.2: Uncorrected distributions of (a) $\log_{10}\xi_p$, (b) $\log_{10}\xi_{EPz}$, (c) $|t|$, (d) $\Delta\eta^F$, (e) Number of MBTS counters above offline threshold and (f) charged particle multiplicity in the ID. In all distributions, σ_{SD} is modified to 8.0 mb compared to the default value in PYTHIA8 of 12.48 mb. Statistical uncertainties are displayed.

8.4 Systematic Uncertainty on Overlay Background

The systematic uncertainty on the OB, stemming from sources such as incorrect cross-sections for the MC events from which the MC background template is formed and the assumption that the backgrounds in ALFA and the central detector are always uncorrelated, is assessed by defining a 'two-proton control region'. This control sample is obtained by using the same random trigger used in the selection of the ND-enriched sample and the trigger efficiencies calculation. The offline selection applied on the sample is the same as the nominal analysis selection, described in Section 6.3.2, with the altered requirement that two instead of one of the ALFA armlets reconstruct a proton. While the two protons are observed to be in an elastic configuration in approximately 96% of events within this sample, no requirement is placed on which armlets tag protons as no such requirement is used in the determination of the OB probabilities.

Figure 8.3 displays the uncorrected distributions obtained within this control region compared to the sum of the simulated and OB contributions. It is observed that the OB is dominant in this region. The discrepancies between the data and background predictions, expressed more obviously in the ratio plots in Figure 8.3, are used to define the systematic uncertainty on the OB. The systematic uncertainty on the OB is implemented separately for each distribution to allow for shape uncertainties as well as normalisation uncertainties.

8.5 CD Shape Uncertainty

The second largest background source, after the OB, is that from CD events. A CD-enriched control region is used to assess the modelling of this background contribution and derive the systematic uncertainty on the CD shape distributions (the normalisation uncertainty is described in Section 9.2.9). This control region is the same as the two-proton control region but with the additional requirement that the num-

ber of MBTS counters above the offline threshold is in the range, $2 \leq n_{\mathrm{MBTS}} < 10$, motivated by the observation of CD dominance at low MBTS multiplicities. The description of this region is displayed in Figure 8.4, in which it can be seen that only OB and CD contribute significantly. A good normalisation agreement is observed, validating the use of the default PYTHIA8 cross-section and associated uncertainties (Section 9.2.9). The study was also performed with similar results in the region $2 \leq n_{\mathrm{MBTS}} < 6$ which has a higher CD purity, but where statistics were found to be a limiting factor.

A good shape agreement is observed for this control sample in all variables except for ξ_p, which is displayed in Figure 8.5a. The background-subtracted data (treating CD as the signal) is compared to the CD MC prediction and a linear fit of,

$$\text{weight} = -1.6 - 1.0 * \log_{10}(\xi) \ , \tag{8.1}$$

is found to describe the data-to-MC ratio. This function is then used to reweight the CD MC, which is then renormalised so as to preserve its normalisation. Following this reweighting, a flat ratio is observed in the ξ_p distribution, see Figure 8.5b, which validates the choice of control region and the fitted function. To assess the systematic uncertainty on the final results, the CD MC is reweighted using this function and then the main analysis is performed.

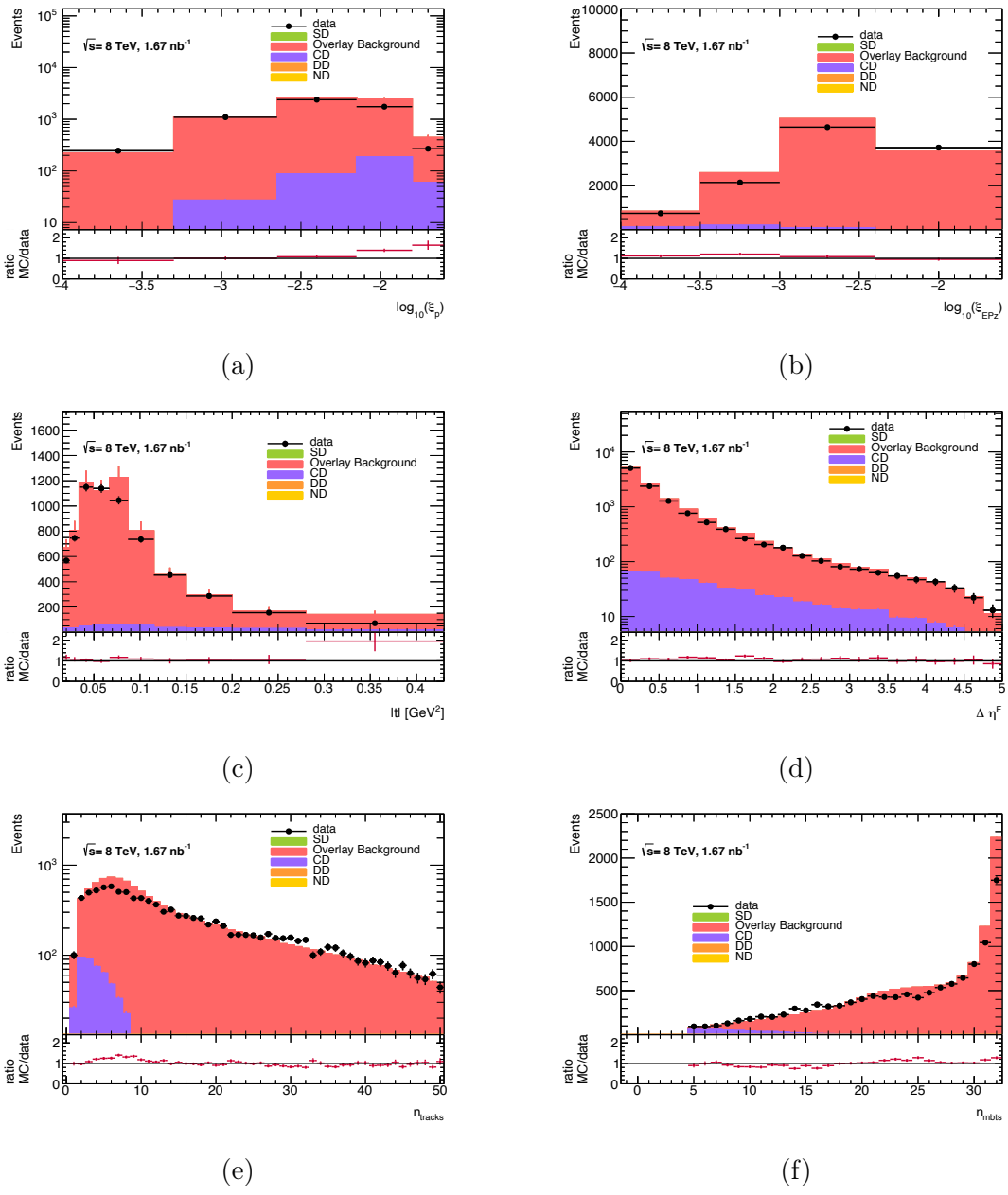

(a) (b) (c) (d) (e) (f)

Figure 8.3: Two-proton control region for assessing the validity of the OB method and from which the systematic uncertainties on the OB subtraction are derived. Statistical uncertainties are displayed.

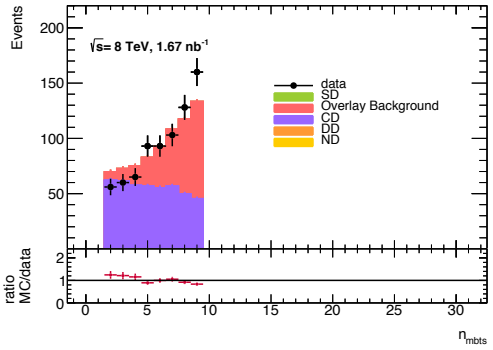

Figure 8.4: Number of MBTS counters above threshold in the two proton, low-MBTS control region. Statistical uncertainties are displayed.

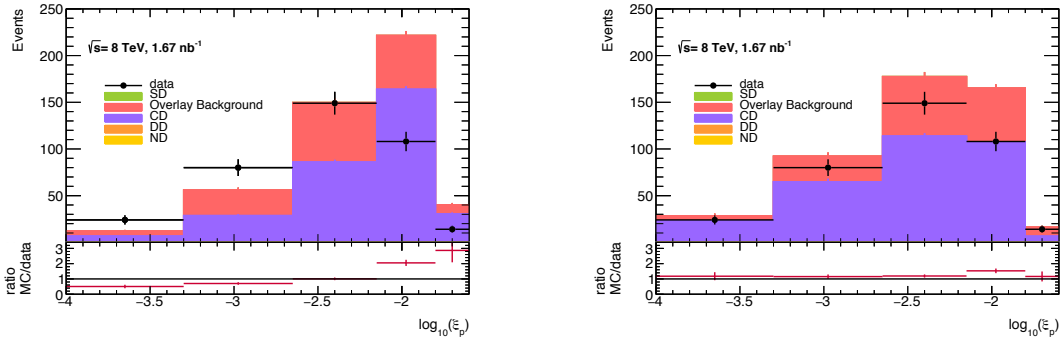

(a) (b)

Figure 8.5: Two-proton, low-MBTS, control region for assessing the CD ξ-shape uncertainty (a) with the nominally weighted CD sample and (b) with the reweighted CD distribution. Statistical uncertainties are displayed.

CHAPTER 9

Unfolding and Systematic Uncertainties

The distributions presented in Figure 8.1 correspond to a data-MC comparison, distorted by detector effects and acceptance. To produce results that may be compared with predictions and other experimental results in a fashion that is independent of the individual experiment, it is necessary to correct the measured data distribution for these effects through a procedure known as unfolding.

9.1 Unfolding

Detector effects are simulated through the use of a response matrix, $\mathbf{A}$, which operates on the vector of true values of a binned measurement, $\vec{x}$, to transform them to the reconstructed values, $\vec{y}$, in the specific experimental setup. This transformation is expressed as,

$$\mathbf{A}\vec{x} = \vec{y} \; . \tag{9.1}$$

$\mathbf{A}$ is a matrix, where the elements $\mathbf{A_{ij}}$ denote the probability of measuring a true value of x_i as y_j. Inverting $\mathbf{A}$ enables the transformation from reconstructed level quantities back to the corresponding truth level values,

$$\vec{x} = \mathbf{A^{-1}}\vec{y}\,, \tag{9.2}$$

which is referred to as unfolding. In this analysis, the data are unfolded to the truth level within the fiducial region defined in Section 6.3.3. Unfolding outside of this region becomes overly dependent on the predictions from the response matrices which are constructed from the signal MC sample. Before unfolding the measured distributions it is necessary to subtract the background contributions, N^{bkgd} (see Section 8), from the raw measured events, N^{meas} (see Section 6.3), so that the result corresponds only to the signal process. Several corrections are applied as part of the unfolding procedure:

- ϵ^{corr}, a factor applied to correct for measurement effects that are not simulated in the MC. These effects in this analysis are the trigger efficiency (see Section 7.1) and the ALFA reconstruction efficiency which, while included in the MC, is observed to differ marginally from the efficiency measured in the data (see Section 7.2). The ϵ^{corr} correction factor is applied separately to each bin to account for the non-constant trigger efficiency for some analysis variables.

- ϵ^{fake}, a correction applied to remove events which lie outside of the fiducial region but pass the event selection. This factor is calculated using MC as,

$$\epsilon^{fake} = \frac{N(\text{reco \& true})}{N(\text{reco})}\,, \tag{9.3}$$

  where $N(\text{reco})$ is the number of events reconstructed in a bin and $N(\text{reco \& true})$ corresponds to $N(\text{reco})$ after the requirement that the events are also within the fiducial region. This fake factor is referred to as the 'unmatched' correction in some analyses

- ϵ^{miss} , a correction applied to account for events that are within the fiducial

region yet are not reconstructed. ϵ^{miss} is calculated from MC through the equation,

$$\epsilon^{miss} = \frac{N(\text{true \& reco})}{N(\text{true})} \ , \tag{9.4}$$

where N(true) represents the number of events that lie in a bin at the truth level and N(reco & true) is N(true) after the requirement that events pass the event selection. This variable is similar to the acceptance variable used to determine the choice of fiducial region, but is expressed as a function of the reconstructed level values rather than the truth level as in the acceptance calculation. It accounts for the reconstruction efficiency as well as for events that migrate out of the fiducial region in their reconstruction.

To calculate the cross-section from the measurement, it is necessary to divide the number of events after unfolding by the integrated luminosity, $\mathcal{L}$, of the data sample. The differential cross-section in observable X is then calculated by dividing each bin, i, by its bin width, ΔX_i. The combination of all these steps in producing the physics measurement is,

$$\frac{\mathrm{d}\sigma}{\mathrm{d}X_i} = \frac{1}{\mathcal{L} \cdot \Delta X_i \cdot \epsilon_i^{miss}} \sum_j A_{ij}^{-1} \cdot (N_j^{meas} - N_j^{bkgd}) \cdot \epsilon_i^{fake} \cdot \epsilon_i^{corr} \tag{9.5}$$

The unfolding method used in the analysis is the iterative Bayesian [109], as implemented in the RooUnfold package [110]. This technique has the advantage over simplistic acceptance and efficiency corrections for each bin, often referred to as 'bin-by-bin unfolding', as it accounts explicitly for migrations of events between bins. If no migration were to occur, the migration matrix would be purely diagonal. From Figure 9.1, the normalised response matrices for the variables studied, it can be seen that this is not true in this analysis, with both methods of ξ reconstruction having very off-diagonal response matrices. That these two response matrices differ between each other demonstrates the power of the ξ_{EPz} cross-check.

The fraction of events that are classified as fake ($1 - \epsilon^{fake}$) and miss ($1 - \epsilon^{miss}$) are displayed in Figures 9.2a and 9.2b, respectively, for the ξ_p variable. The 'purity' is

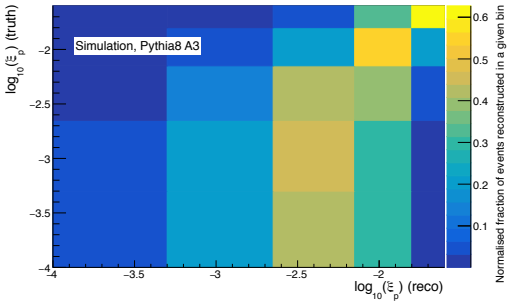

(a) Response matrix for $\log_{10}(\xi_p)$

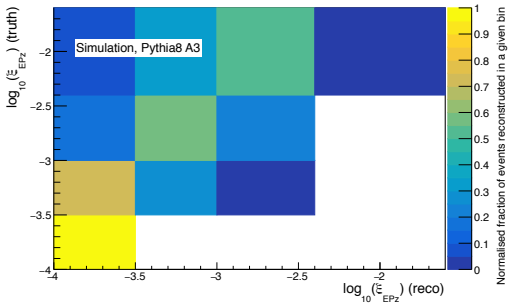

(b) Response matrix for $\log_{10}(\xi_{EPz})$

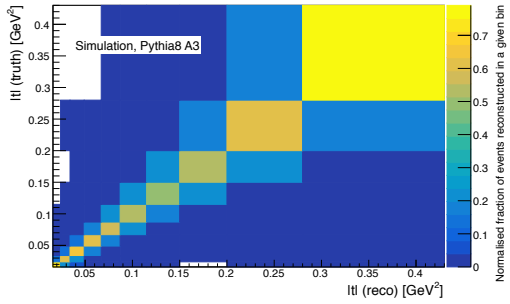

(c) Response matrix for $|t|$

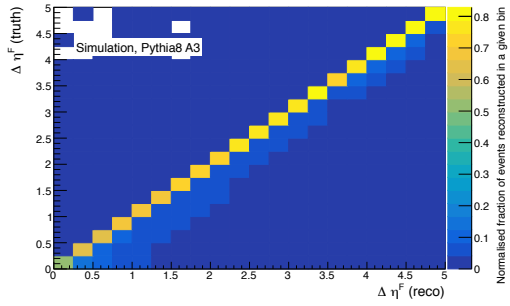

(d) Response matrix for $\Delta\eta^F$

Figure 9.1: Response matrices for diffractive variables. The reconstructed value (x-axis) is plotted against the truth value (y-axis) for all SD events in MC. Each truth bin is normalised to total 1.0, enabling simple interpretation of the fraction of events reconstructed in each reconstructed level bin.

defined as the fraction of events in a bin at the reconstructed level that are in the same bin at the truth level. A low purity can be the result of poorly defined bin widths, which are significantly smaller than the resolution, or due to a systematic shift between the truth and reconstructed level observable. It can be seen in Figure 9.2c that the purity is low for the ξ_p variable. Figure 9.1a displays that this low purity stems from a systematic shift in the reconstruction rather than from the binning. Within this analysis, the systematic shift is accounted for by the unfolding procedure, which results in the unfolding procedure having to perform larger corrections and can result in a larger systematic uncertainty. The fake, miss and purity plots for all analysis variables are displayed in Appendix A.

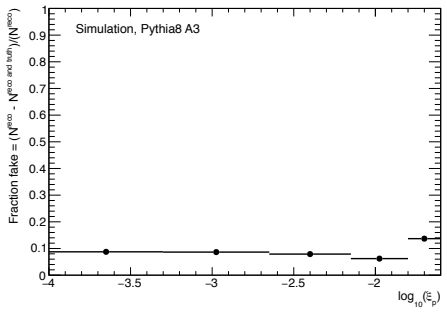

(a) $(1 - \epsilon^{fake})$ for $\log_{10}(\xi_p)$

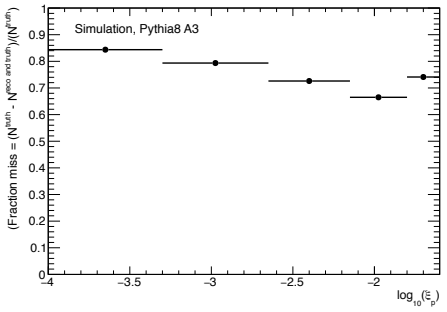

(b) $(1 - \epsilon^{miss})$ for $\log_{10}(\xi_p)$

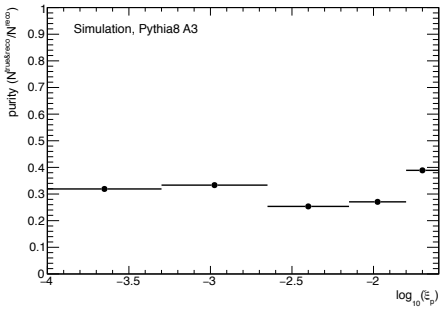

(c) Purity for $\log_{10}(\xi_p)$

Figure 9.2: Unfolding plots for the example of the ξ_p variable. (a) The fraction of events in each reconstructed level bin that are fakes, (b) the fraction of events in each truth level bin that are missed, (c) the purity in each reconstructed level bin.

9.1.1 Optimisation

Within the iterative Bayesian unfolding method, the degree of regularisation (the relative weight placed on the data compared to the truth level MC) is determined by the number of iterations used. Under-regularisation results in the amplification of statistical fluctuations in the data whereas over-regularisation results in more bias from the prior (the truth level distribution used in the unfolding). Within the iterative Bayesian method, more iterations performed by the unfolding procedure result in a less regularised result, as each iteration serves to distance the result from the prior.

The prescription followed for selecting the number of iterations used in the unfolding procedure is to use the number of iterations which minimises the systematic

uncertainty resulting form the unfolding process (see Section 9.1.3) while reducing statistical fluctuations due to under-regularisation where possible. Two factors are considered when reducing the uncertainty on the unfolding: the average absolute uncertainty across all bins and the uncertainty deriving from the unfolding on the extraction of the fitted parameters, see section 10.

The considerations used in the optimisation of the number of unfolding iterations for the ξ_p variable are displayed in Figure 9.3. The equivalent distributions for the other analysis variables are displayed in Appendix A. The fractional uncertainty on the ξ_p variable is displayed for between one and ten iterations of the unfolding procedure in Figure 9.3a. The mean uncertainty per bin is displayed in Figure 9.3b. The absolute uncertainties on one of the the fitted parameters for the extraction of the main analysis results is displayed in Figure 9.3c. The details of these fits are provided in section 10.

The stability under differing numbers of iterations of the the main variables on which the final fits are performed (ξ_p and $|t|$) are displayed in Figure 9.4. It can be seen that the fitted parameters are stable under number of iterations, within uncertainties. The number of iterations used for each variable is selected by minimising the unfolding uncertainty on the fitted parameters. Where there is no obvious minimum, the number is selected to be that after which the fitted parameter is observed to be stable with respect to the number of iterations. Where no fits to the cross-section are performed, such as for the $\Delta\eta^F$ variable, the number of iterations resulting in the lowest unfolding uncertainty per bin is selected. The number of iterations selected for every variable is listed in Table 9.1.

Variable	**Number of iterations**
$\log_{10}(\xi_p)$	3
$\log_{10}(\xi_{EPz})$	1
$\|t\|$	4
$\Delta\eta^F$	2

Table 9.1: Number of iterations used in the iterative Bayesian unfolding method.

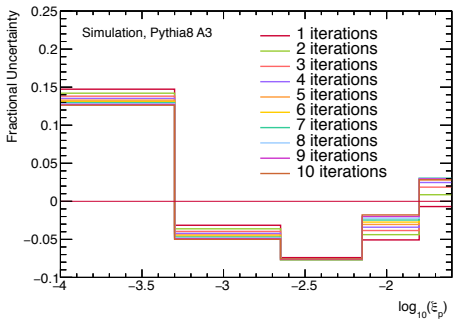

(a)

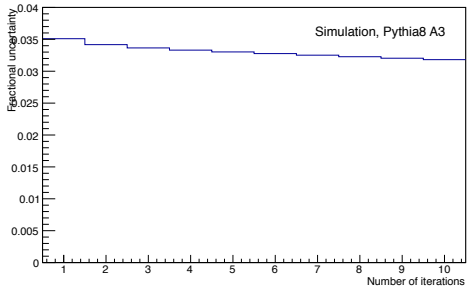

(b)

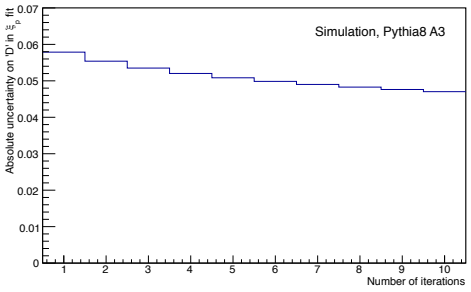

(c)

Figure 9.3: Plots used in the optimisation of the number of iterations for ξ_p: (a) Fractional unfolding systematic uncertainty for between one to ten iterations of the unfolding procedure, (b) mean unfolding uncertainty per bin as a function of the number of iterations of the unfolding procedure, (c) absolute unfolding uncertainty on the 'D' parameter in the fit to the ξ differential cross-section as a function of the number of iterations.

9.1.2 Validation of Unfolding Method

To verify that the unfolding procedure is correctly implemented and that all internal and external migrations are accounted for, a simple 'closure' test is undertaken. This test is performed by unfolding the PYTHIA8 A3 MC sample reconstructed level distribution with the response matrix generated using the same sample and then comparing the unfolded distribution with the truth level A3 distribution. As the samples compared in this test are statistically identical, the unfolding procedure should be able to perfectly reproduce the truth level distribution. The results of this test are displayed in Figure 9.5. A perfect agreement is observed, as can be best

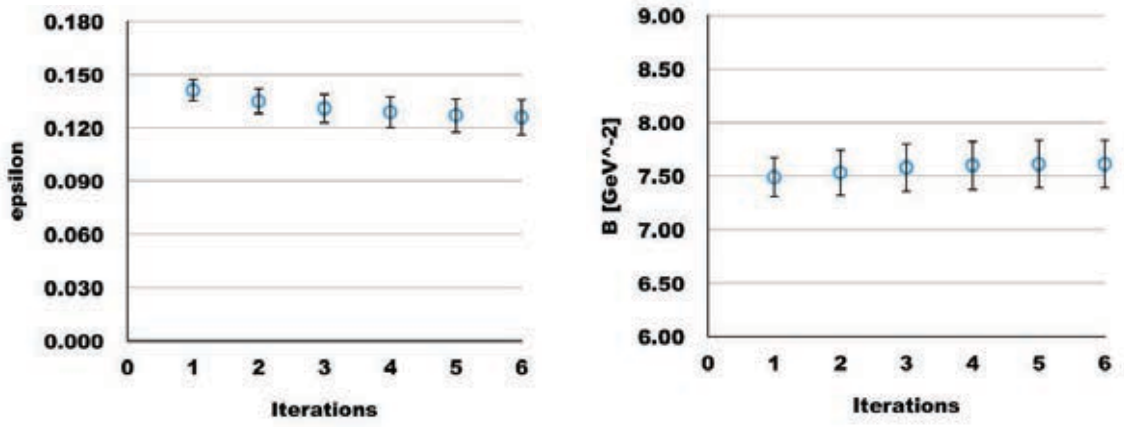

(a) ϵ from $\log_{10}(\xi_p)$ (b) B slope from $|t|$

Figure 9.4: Stability of the final analysis extracted parameters from the fits (see Section 10) as a function of the number of iterations. Statistical uncertainties are displayed. The value of ϵ is calculated in the 'triple Pomeron' formalism.

seen in the ratio plots.

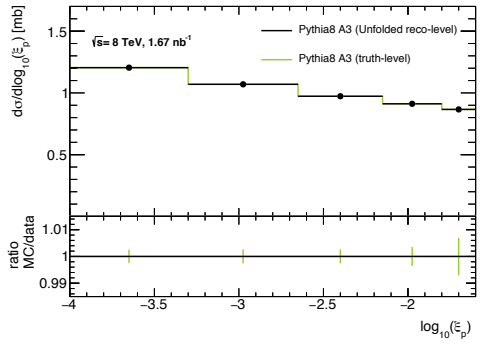

(a) $\log_{10}(\xi_p)$

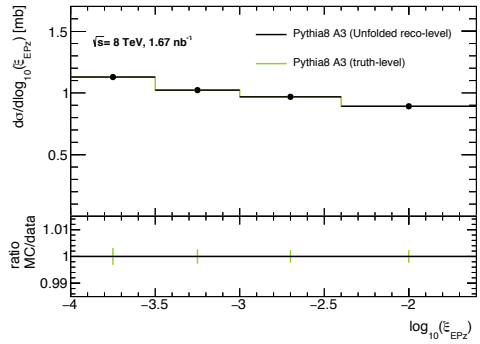

(b) $\log_{10}(\xi_{EPz})$

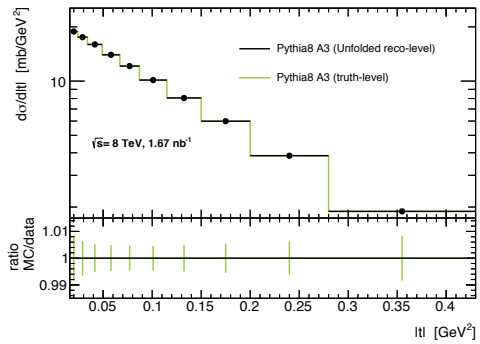

(c) $|t|$

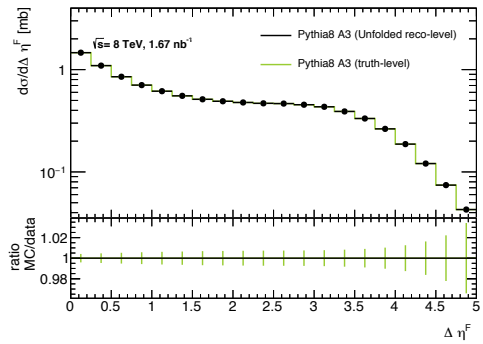

(d) $\Delta\eta^F$

Figure 9.5: Simple closure tests for all analysis variables. The detector-level Pythia8 A3 MC is unfolded using the nominal analysis response matrix (black). This is compared to the truth level distribution within the Pythia8 A3 MC sample (green). The truth level distribution is hidden behind the unfolding output in all bins. Statistical uncertainties on the MC are displayed.

9.1.3 Closure Test and Systematic Uncertainty on Unfolding

A more non-trivial closure test is performed to evaluate the systematic uncertainty inherent to the unfolding of the raw measured data. The motivation behind this test is to determine how accurately the response matrix can unfold a data-like shape, which is recreated in the MC. The steps involved in this method are:

- The MC is reweighted by a polynomial such that the reconstructed level MC agrees well with the background-subtracted data. The reweighting function is applied at the truth level, such that the MC event has the same weight whether the truth or reconstructed level information is used.
- The reweighted reconstructed level MC is unfolded using the nominal (not reweighted) response matrix.
- The difference between the reweighted truth level MC and the unfolding output is taken as the systematic uncertainty.

The reweighting functions used for each variable are listed in Table 9.2, where the order of the polynomial was determined by eye as to which provided the best reweighting performance. The background-subtracted data are compared to the reweighted and nominal MC in Figure 9.6. After unfolding, the reweighted MC is compared to the reweighted truth level MC in Figure 9.7. The fractional difference between the reweighted unfolding output and the reweighted truth level distribution is taken to be the fractional systematic uncertainty.

The largest unfolding uncertainties are observed in the ξ distributions, due to their non-diagonal shape. Conversely, the other distributions are much smoother and the unfolding uncertainty is not found to be one of the dominant sources of systematic uncertainty.

An additional stress test of the unfolding procedure was performed by reweighting the prior by the functions $W = e^{\pm|t|}$ and $\xi^{\pm 0.1}$ and again performing a closure test.

The performance within these tests was found to be consistent with the unfolding uncertainties, implying that the unfolding method can be relied upon to not fail across a large range of t and ξ shapes.

Variable	**Reweighting function (x = Variable)**
$\log_{10}\xi_p$	$0.2578 - 0.3249x - 0.0697x^2$
$\log_{10}\xi_{EPz}$	$0.0118 - 0.3723x - 0.0578x^2$
$\|t\|$	$0.63245 - 0.2750x + 0.1329x^2$
$\Delta\eta^F$	$0.6400 + 0.0378x - 0.0610x^2 + 0.0121x^3$

Table 9.2: Smooth functions used to re-weight the MC as a function of the truth level variable for the data-driven closure test.

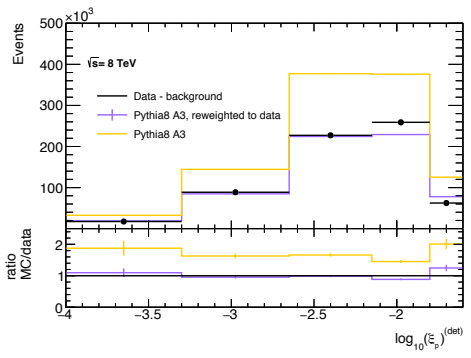

(a) Reweighted MC Vs Data in $\log_{10}(\xi_p)$

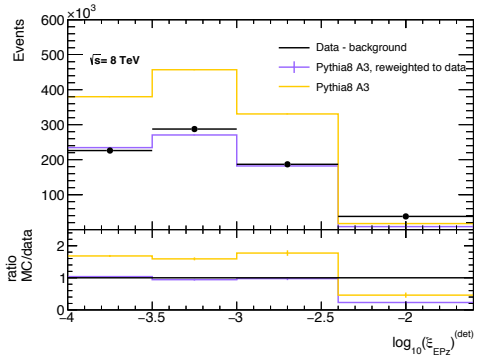

(b) Reweighted MC Vs Data in $\log_{10}(\xi_{EPz})$

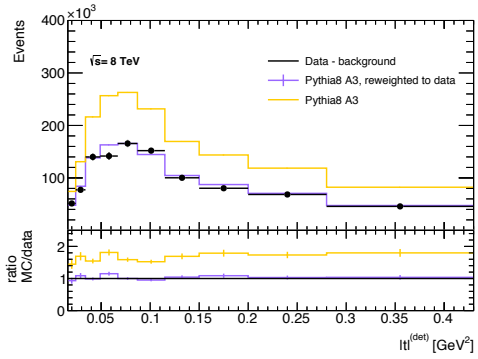

(c) Reweighted MC Vs Data in |t|

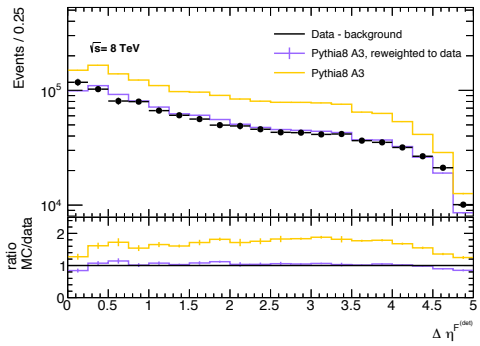

(d) Reweighted MC Vs Data in $\Delta\eta^F$

Figure 9.6: Nominal MC (yellow), compared to reweighted MC (purple) and the measured data (black). Statistical uncertainties are displayed.

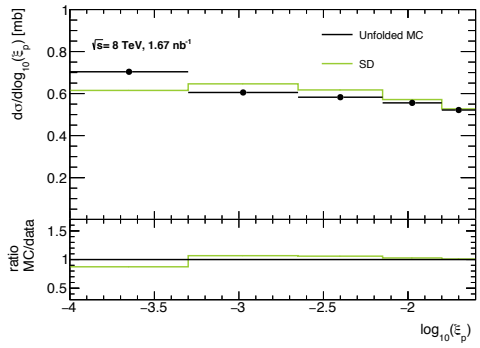

(a) Unfolded, reweighted MC Vs reweighted truth level MC in ξ_p

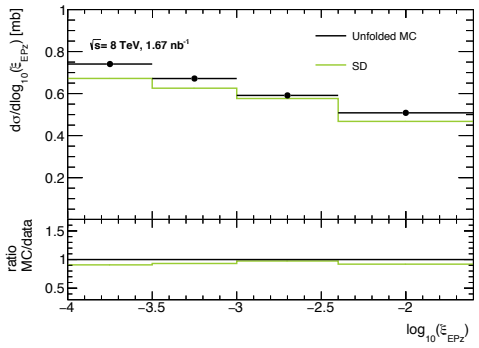

(b) Unfolded, reweighted MC Vs reweighted truth level MC in $\log_{10}(\xi_{EPz})$

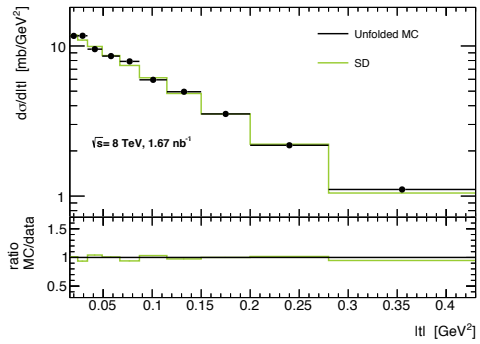

(c) Unfolded, reweighted MC Vs reweighted truth level MC in |t|

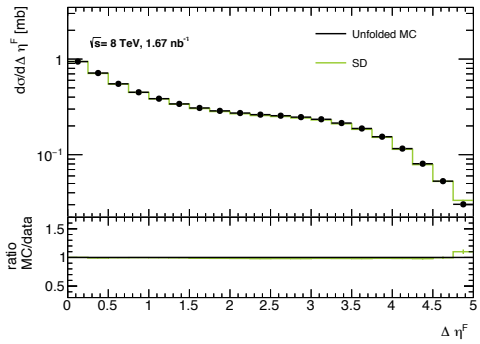

(d) Unfolded, reweighted MC Vs reweighted truth level MC in $\Delta\eta^F$

Figure 9.7: Reweighted truth level MC (green) compared to unfolded, reweighted reconstructed level MC (black). The difference between these two distributions is taken to be the systematic uncertainty stemming from the unfolding. Statistical uncertainties on the MC are displayed.

9.2 Systematic Uncertainties

The systematic uncertainties described within this section aim to account for any inaccuracies in the final results that stem from experimental effects. The uncertainty from each contribution is evaluated by repeating the analysis with the parameter in question varied to one extreme of its uncertainty range and then again for the other extreme of the uncertainty range. The systematic uncertainty on the final cross-section is determined to be the difference between the systematically shifted cross-sections and the nominal analysis value. The contributions from all evaluated sources of systematic uncertainty are displayed in Figure 9.8 to enable easy identification of the dominant sources, which are the overlay background, unfolding and 'cross-section' uncertainties. The individual sources are described in detail in the rest of this section. In addition, several systematic checks were performed to test the stability of the analysis, for example including repeating the analysis using only protons tagged on the A and C sides separately. These systematic checks are included as Appendix B.

For all sources of systematic uncertainty, unless otherwise stated, an upward and downward variation is applied. The separate resulting upwards and downwards shifts in the cross-section from each variation are maintained as they can have differing impacts on the non-linear fits applied in Section 10. An upward and downward total uncertainty is calculated by summing in quadrature the upward and downward contributions in each bin separately. These sums are displayed as the dashed black lines in Figure 9.8, from which it can be seen that the uncertainties are symmetric to first approximation. On the final presented cross-sections, the upward and downward totals are symmetrised by taking the larger of the two and these form the error bars displayed. The uncertainty on the fitted parameters is similarly symmetrised after summing the upwards and downwards contributions.

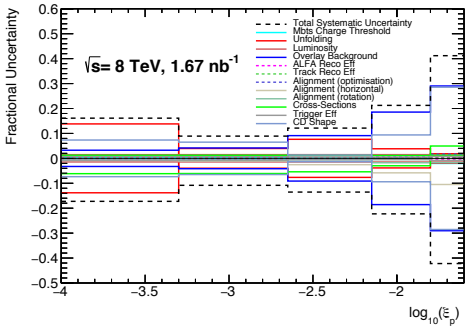

(a) Total uncertainty in $\log_{10}(\xi_p)$

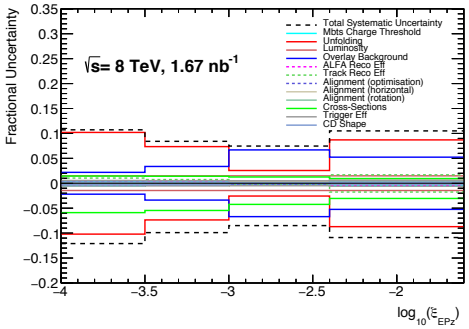

(b) Total uncertainty in $\log_{10}(\xi_{EPz})$

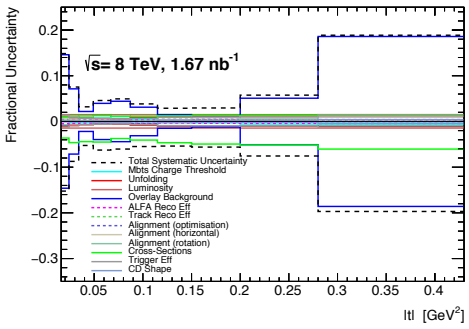

(c) Total uncertainty in $|t|$

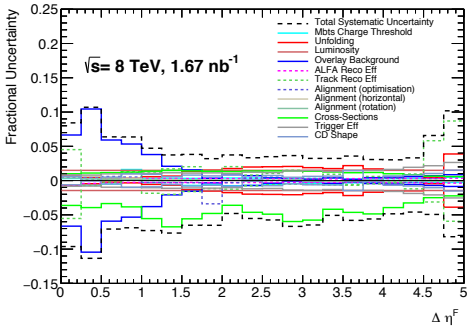

(d) Total uncertainty in $\Delta\eta^F$

Figure 9.8: Total fractional uncertainty and all contributions to this uncertainty on the measured differential cross-sections of the studied variables.

9.2.1 MBTS Charge Threshold

The charge threshold used to suppress noise in the MBTS counters is determined by a Gaussian fit to the noise peak, which is centred at approximately 0.0 pC. The threshold used to distinguish between noise and signal in the MBTS counters is defined as $\mu + 4\sigma$. For the systematic uncertainty, the threshold is varied between $\mu + 3\sigma$ and $\mu + 5\sigma$. Little effect is observed in any of the unfolded cross-sections, as displayed in Figure 9.9, where the uncertainty is less than 1% in all bins.

9.2.2 Unfolding

The systematic uncertainty deriving from the unfolding procedure is described in section 9.1.3. As the procedure to evaluate this systematic uncertainty only results

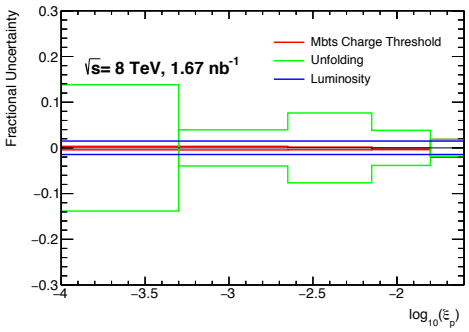

(a) Fractional uncertainty as a function of $\log_{10}(\xi_p)$

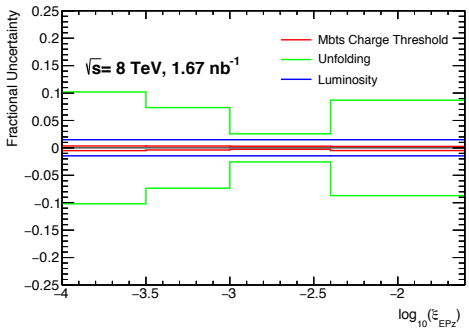

(b) Fractional uncertainty as a function of $\log_{10}(\xi_{EPz})$

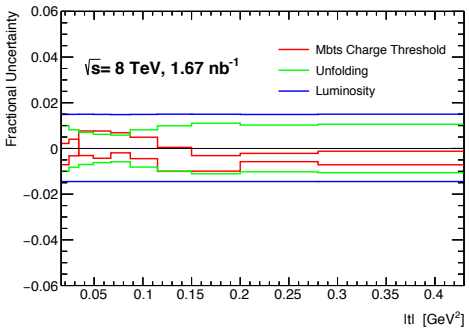

(c) Fractional uncertainty as a function of $|t|$

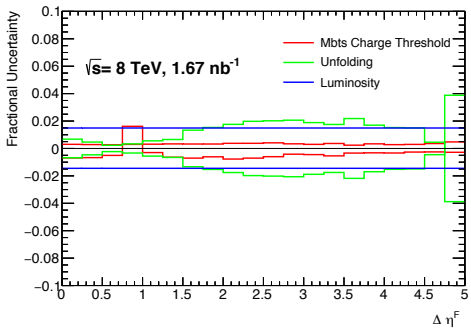

(d) Fractional uncertainty as a function of $\Delta\eta^F$

Figure 9.9: Fractional uncertainties on the measured differential cross-sections stemming from uncertainties on the selection of the MBTS charge threshold, unfolding and luminosity.

in an uncertainty in one direction, it is symmetrised. The resultant uncertainties on the measured variables are displayed in Figure 9.9.

9.2.3 Luminosity

The luminosity uncertainty used is 1.47 %, derived using the method described in [46] which calculates the luminosity uncertainty for the $\sqrt{s} = 8\,\text{TeV}$ 2012 ATLAS running period to be 1.9%. The smaller uncertainty used in this analysis is due to the unique features of this low luminosity run and the fact that all the data were collected in one physics run. As the instantaneous luminosity used in the analysis described in this document is similar to that used in the van der Meer (vdM) runs,

described in Section 2.2, there is no need to account for the 'calibration transfer' uncertainty which is used to account for the fact that the luminosity is very different in vdM and nominal high pile-up runs. Another source of luminosity uncertainty that can be neglected is the 'run to run' consistency uncertainty, which does not pertain to analyses performed on a single data run. This approach to calculating the luminosity uncertainty was applied to previous ALFA analyses and is detailed in [73]. To assess the uncertainty on the measured cross-sections from this uncertainty, the luminosity is varied by $\pm 1.47\%$ and is propagated through the entire analysis. The resultant uncertainties on the measured variables are displayed in Figure 9.9.

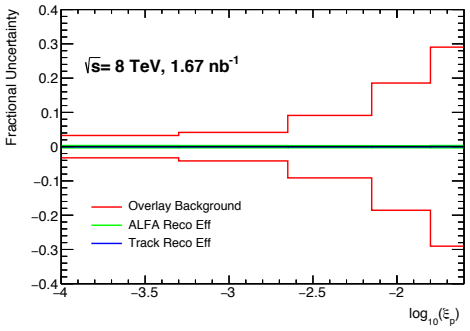

(a) Fractional uncertainty as a function of $\log_{10}(\xi_p)$

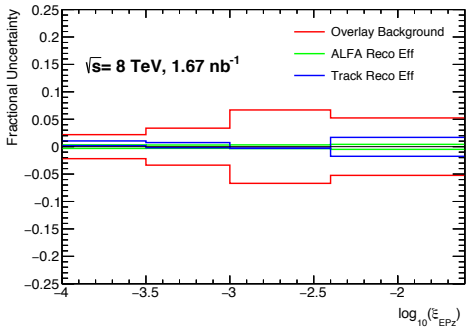

(b) Fractional uncertainty as a function of $\log_{10}(\xi_{EPz})$

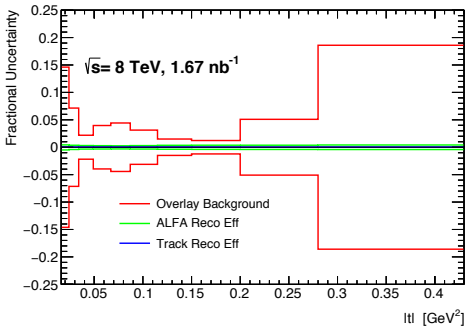

(c) Fractional uncertainty as a function of $|t|$

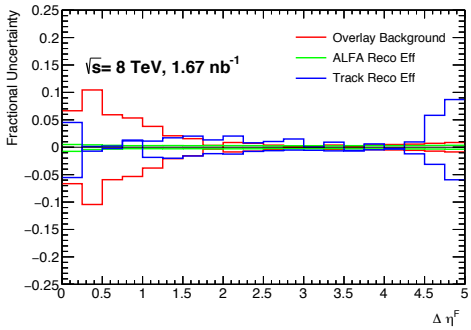

(d) Fractional uncertainty as a function of $\Delta\eta^F$

Figure 9.10: Fractional uncertainties on the measured differential cross-sections stemming from uncertainties on the overlay background, the track reconstruction efficiency and the ALFA reconstruction efficiency.

9.2.4 Overlay Background

The 'Overlay Background' (OB) contribution that is subtracted from the raw data is varied by the uncertainty on the OB which is defined in Section 8.4. This uncertainty is then symmetrised. The uncertainty per bin varies considerably, but is of order 10%, with a much larger uncertainty at high ξ_p. Uncertainties are treated as uncorrelated between bins, resulting in a conservative overestimate of the systematic uncertainty. The resultant uncertainties on the measured variables are displayed in Figure 9.10.

9.2.5 Tracking Efficiency

The tracking efficiency uncertainty for the detector configuration used in this analysis, at $\sqrt{s} = 8\,\text{TeV}$, has previously been studied in detail [78], finding that the dominant source of uncertainty on the track reconstruction efficiency arises from the material description in the ATLAS ID. In this previous analysis, the efficiencies are calculated as a function of track η and p_T and are displayed in Figure 9.11 with their corresponding uncertainties. These uncertainties are reused in this analysis.

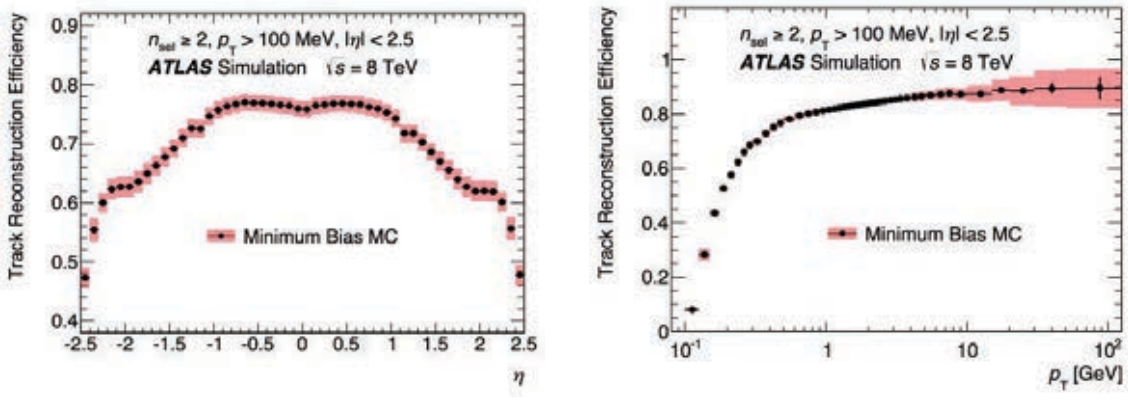

(a) (b)

Figure 9.11: ATLAS ID track reconstruction efficiency as a function of (a) pseudo-rapidity, η, and (b) transverse momentum, p_{T}. Taken from [78]

The downward systematic uncertainty is calculated by randomly removing tracks from the data sample, with the probability of removal dictated by the uncertainty as

a function of (η, p_{T}). The upward uncertainties are evaluated by repeating the same process in the MC samples. Figure 9.10 displays the uncertainty on the measured cross-sections stemming from the track reconstruction efficiency uncertainty. In variables calculated in ALFA, the uncertainty is negligible, as only events where all tracks fail the reconstruction have an effect. In the variables calculated from the ID tracks, $\Delta\eta^F$ and $\log_{10}\xi_{EPz}$, the uncertainty has non-negligible effects, as missed events and migrations in the reconstructed value of the variables are more significant. The uncertainty is greatest at large values of $\Delta\eta^F$ as when the leading track fails reconstruction, the rapidity gap becomes larger or the event is not reconstructed at all.

9.2.6 ALFA Reconstruction Efficiency

The method of determining uncertainties on the ALFA reconstruction efficiency in data and MC is detailed in Section 7.2.2. These uncertainties are propagated to a systematic uncertainty on the efficiency correction factor used in the analysis by taking the upward systematic variation for both the data and MC (since the variations used to calculate the uncertainty on the efficiencies affect the data and MC in the same way and are not independent) and recalculating the ratio $\epsilon^{\mathrm{data}}/\epsilon^{\mathrm{MC}}$, which is applied to the MC event weights. This process is repeated for the downward variations. The event weights applied to the MC are detailed in Table 9.3. The effects of these uncertainties are displayed in Figure 9.10. The resultant uncertainty is less than 1% per bin.

Armlet	**Nominal**	**Upwards Variation**	**Downwards Variation**
L1U	0.9933	0.9949	0.9917
L1L	0.9941	0.9991	0.9892
R1U	0.9825	0.9812	0.9838
R1L	0.9774	0.9857	0.9695

Table 9.3: Event weights used to correct the MC for differences in ALFA reconstruction efficiency. Values derived in Section 7.2.2.

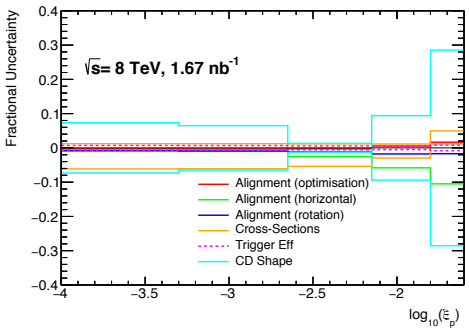

(a) Fractional uncertainty as a function of $\log_{10}(\xi_p)$

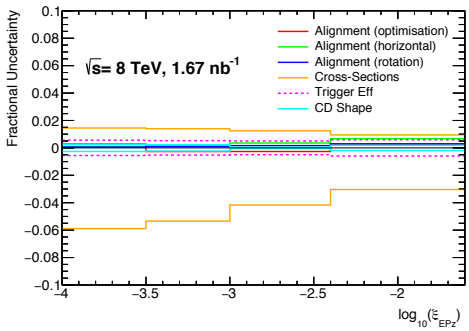

(b) Fractional uncertainty as a function of $\log_{10}(\xi_{EPz})$

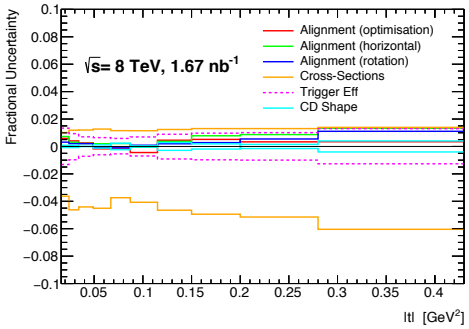

(c) Fractional uncertainty as a function of $|t|$

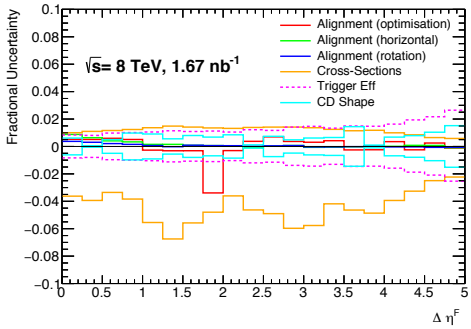

(d) Fractional uncertainty as a function of $\Delta\eta^F$

Figure 9.12: Fractional uncertainties on the measured differential cross-sections stemming from uncertainties on the ALFA alignment, MC cross-sections, trigger efficiency and ξ shape uncertainty on the CD MC sample.

9.2.7 ALFA Alignment

The ALFA alignment parameters used in this analysis were calculated for the total cross-section analysis [73]. This alignment is responsible for accurately determining the position of the ALFA RPs, necessary to determine the x and y coordinates of tracks in ALFA and thus enabling the accurate calculation of t and ξ. Following the method for assessing the alignment uncertainty previously used in the total cross-section analysis [73], where a far more thorough definition of this method is provided, several different sets of ALFA alignment parameterisations are used to calculate the location of track hits in ALFA. The analysis is repeated for each of these different sets and the envelope of the deviations from the nominal for each type of uncertainty

is taken as the systematic uncertainty, as displayed in Figure 9.12. The alignment uncertainty is separated into three categories: 'rotational', 'horizontal offset' and 'optimisation'.

The sets of alignment parameters used in both the ALFA total cross-section analysis and this analysis are:

- Nominal alignment
- Two different fits to the x-y relative rotation of the ALFA Roman pots
- Three different horizontal offsets, one derived from a Gaussian fit to determine the central value in the x-plane (the median value of all events is used in the nominal) and two calculated using a different y-range for the hits in ALFA to assess any bias in the selection of the nominal y-range, which excludes the edges of the detectors.
- Three separate optimisations, which are determined by which ALFA station is used to define the extrapolation to the other stations, using the symmetry of elastic scattering event patterns. Two of these optimisations are performed by fixing the spatial coordinates of the A7L1 and A7R1 stations separately, and the third set is defined by fixing both the A7L1 and A7R1 stations and performing the alignment procedure.

9.2.8 Trigger efficiency

The systematic uncertainty deriving from the trigger efficiency calculation is described in Section 7.1.1. The resulting uncertainties are shown in Figure 9.12 and are small.

9.2.9 MC Background Composition

The cross-sections of the background processes modelled by MC within this analysis are not well constrained. The method for assessing the systematic uncertainty on these cross-sections is based upon that used in the ATLAS $\sqrt{s} = 7\,\text{TeV}$ rapidity gaps analysis [92]. The ratio between the MC cross-sections is varied using constraints measured by the CDF collaboration, which are deemed to be valid at $\sqrt{s} = 8\,\text{TeV}$ as it was for $\sqrt{s} = 7\,\text{TeV}$. The total cross-section is predicted to only vary by approximately 1% between these two centre-of-mass energies, according to Equation 5.11.

The ratio of the SD to the DD cross-section is constrained to be $0.29 < \sigma_{DD}/\sigma_{SD} < 0.68$ [111, 112] when extracted to the full diffractive kinematic range of PYTHIA8 [92]. As the DD contribution to the raw measured data is negligible, the only significant effect of this variation is to the shape of the OB sample in the variables relying on MC for their shape: ξ_{EPz} and $\Delta\eta^F$. As the uncertainty on the OB is assessed separately, the sum of σ_{DD} and σ_{SD} is held constant. The resultant variations in the values of σ_{DD} and σ_{SD} used in the systematic variations are listed in Table 9.4.

The PYTHIA8 default value for the ratio of $\sigma_{CD}/\sigma_{SD} = 0.097$ is held fixed while the σ_{DD}/σ_{SD} ratio is varied. This value is equivalent to the value measured by CDF of $\sigma_{CD}/\sigma_{SD} = 0.194 \pm 0.001 \pm 0.012$ [77][1]. The values of σ_{CD} used in the systematic cross-section variations are also varied by the statistical and systematic uncertainties from the CDF measurement, in addition to the running with σ_{SD}, in the direction that maximises their diference from the nominal value. The resultant upper and lower variations of σ_{CD} are 1.66 mb and 1.12 mb, respectively.

The value of σ_{ND} is not varied as this quantity only impacts upon the OB contribution. The uncertainties on this background contribution are detailed in Section 9.2.4.

[1] Only proton dissociation, and not anti-proton dissociation, was considered in the normalisation of σ_{SD} in this CDF analysis, thus the appropriate ratio for use in this analysis is 0.097.

	Pythia8 nominal	**Systematic variation 1**	**Systematic variation 2**
σ_{SD} [mb]	12.48	16.07	12.34
σ_{DD} [mb]	8.25	4.66	8.39
σ_{CD} [mb]	1.21	1.66	1.12
σ_{ND} [mb]	50.91	50.91	50.91

Table 9.4: Sets of cross-sections used to calculate the systematic uncertainty on the background cross-sections.

The resulting fractional systematic uncertainties on the differential cross-sections are displayed in Figure 9.12. The systematic uncertainty arises from the CD background subtraction and the variation of the relative contributions of each MC sample to the OB. The ID uncertainty distributions are not flat in shape largely due to the mixture of MC that underpins the OB being changed. For example, when σ_{DD} is increased, the OB assumes a more DD-like shape. This effect is not present on the ALFA distributions ($|t|$ and ξ_p) as the shape of the OB in these cases is derived from data and thus is unaffected by the varying of MC cross-sections. The shape of the distributions of uncertainties in the ALFA variables are due to the shape of the CD MC.

9.2.10 CD shape uncertainty

The two significant background sources in this analysis are observed to be CD and the OB. The shape and normalisation uncertainty on the OB is accounted for in section 8.4. The normalisation uncertainty on the MC samples is accounted for in the varying of their cross-section, see section 9.2.9. Additionally, shape uncertainties on the MC samples must be accounted for. The contributions from the ND and DD samples are negligible (outside of their contribution to the OB, which is separately accounted for). The CD shape uncertainty is assessed using a CD-enriched control region, as described in Section 8.5. The resultant uncertainties on the measured differential cross-sections are displayed in Figure 9.12. The CD shape uncertainty is one of the largest sources of uncertainty, particularly in the high-ξ region. The nominal Pythia8 CD shape is retained for used in the main analysis as this uncertainty

is extracted in a control region in the tail of the MBTS multiplicity distribution and any discrepancies may well be exaggerated.

CHAPTER 10

Results

The unfolded SD cross-sections, corresponding to the fiducial region $-4.0 < \log_{10}\xi < -1.6$ and $0.016 < |t| < 0.43\,\text{GeV}^2$, are presented differentially in t, $\log_{10}\xi$ and $\Delta\eta^F$ in Figure 10.1. The t and $\log_{10}\xi$ cross-sections are fully specified by the fiducial range, while the cross-section differential in $\Delta\eta^F$ is further defined as the separation in rapidity between the ID edge on the side of the scattered proton, $|\eta| = 2.5$, and the nearest charged particle with a transverse momentum of at least 200 MeV. The ξ_p variable is unfolded to true ξ. The full uncertainties are shown, with the statistical uncertainty generally being negligible except for regions in which the OB is derived from a small number of events in the ND-enriched sample, see Section 8.2.

The data in Figure 10.1 are compared to predictions from the two SD MC models available within this analysis, the Pythia8 A2 and A3 tunes, using the SS and DL Pomeron flux models, respectively. Both of these predictions are observed to significantly overestimate the measured cross-section within the fiducial region. This is compatible with the previous ATLAS measurement of the rapidity gap spectra

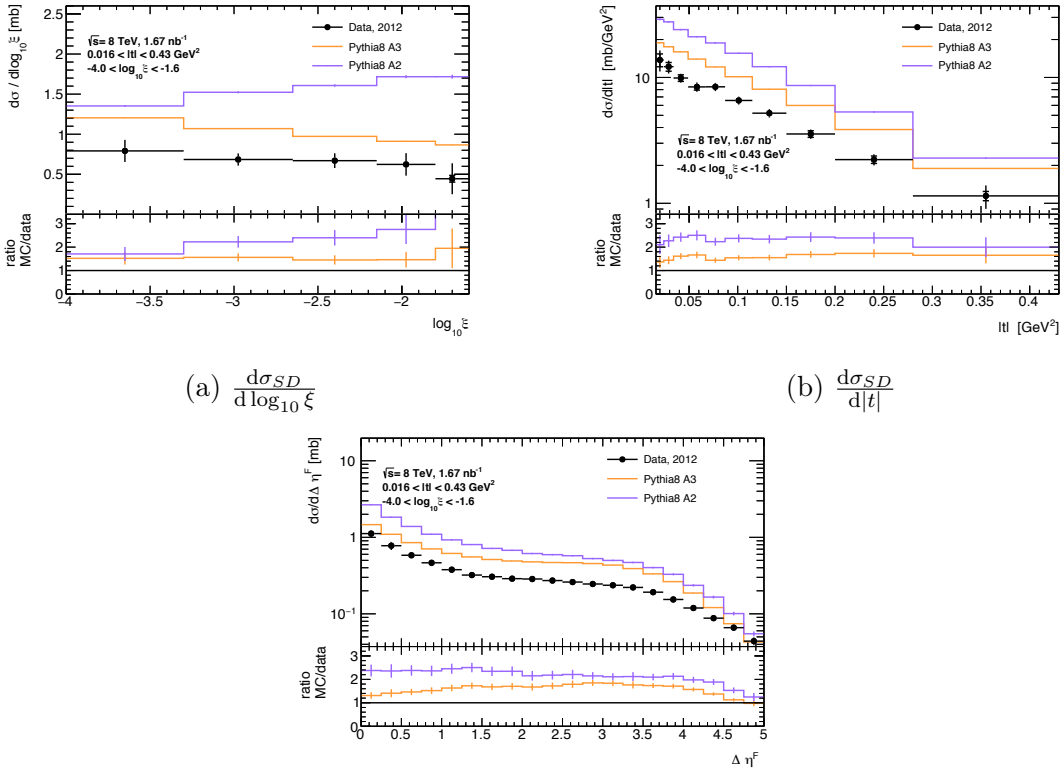

(a) $\frac{\mathrm{d}\sigma_{SD}}{\mathrm{d}\log_{10}\xi}$ (b) $\frac{\mathrm{d}\sigma_{SD}}{\mathrm{d}|t|}$

(c) $\frac{\mathrm{d}\sigma_{SD}}{\mathrm{d}\Delta\eta^F}$

Figure 10.1: Hadron level differential cross-sections as a function of: (a) $\log_{10}\xi$ measured using the scattered proton, (b) |t| and (c) $\Delta\eta^F$. Inner error bars represent only statistical uncertainties while outer error bars display the combination of statistical and systematic uncertainties.

[92] if the DD contribution in the latter is assumed to be correct. The better description of the ξ cross-section shape is provided by the A3 tune of PYTHIA8, which further supports the conclusions of previous ATLAS analyses that the data are best described with a Pomeron intercept significantly above unity [92, 93]. Both models are capable of describing the shapes of the t and $\Delta\eta^F$ distributions with reasonable accuracy.

Considering Equation 5.19, it is expected that the cross-section as a function of $\log_{10}\xi$ is approximately constant. Equation 6.2 expresses the correlation between ξ and the rapidity gap between the proton and the dissociative system, such that the cross-section as a function of this rapidity gap is also expected to be flat. The cross-section differential in $\Delta\eta^F$ is observed to plateau in the region $1.5 < \Delta\eta^F < 3.5$,

as expected. However, deviations from this plateau occur at the extremes of $\Delta\eta^F$ values. The cross-section falls strongly with increasing $\Delta\eta^F$ at the smallest values due to the restricted range of sensitivity of the rapidity gap variable, $\Delta\eta^F$. Events across a wide range of ξ values stack up at low values of $\Delta\eta^F$ due to limited detector coverage. A fall off of the cross-section is observed at large values of $\Delta\eta^F$. This is the result of the definition of the fiducial region of the analysis being at $\log_{10}\xi = -4.0$, which corresponds to a gap size of $\Delta\eta^F \sim 4$, and so values of $\Delta\eta^F$ above this are suppressed. Both MC samples predict these deviations from the plateau at small and large values of $\Delta\eta^F$.

The main ξ cross-section measurement is taken from ALFA and is cross-checked with the ID-based method. This cross-check has a very different background distribution, see Figure 8.1, and a dissimilar response matrix, see Figure 9.1 from the nominal method of ξ reconstruction. To allow a direct comparison, both distributions are unfolded to the true ξ value, defined in 5.15. The comparison is displayed in Figure 10.2. That the results from these two methods are consistent provides strong confidence in the measurement.

Only statistical uncertainties are presented on the ξ_{EPz} cross-check measurement as the systematic uncertainty is very hard to quantify with the available MC samples owing to the method's high sensitivity to hadronisation, which can vary greatly between MC models. The highest ξ_{EPz} bin is not displayed as it is observed to be heavily dominated by background, (see Figure 8.1), such that this region is highly sensitive to the MC prediction used to calculate the bin-to-bin migrations in the unfolding procedure.

10.1 Extraction of Slope Parameter

From Equation 5.17, it is expected that the $|t|$ distribution can be modelled by an exponential shape. Before a fit can be performed to extract B, the slope parameter, the $|t|$ values of the data points are shifted such that they are at the centre of gravity

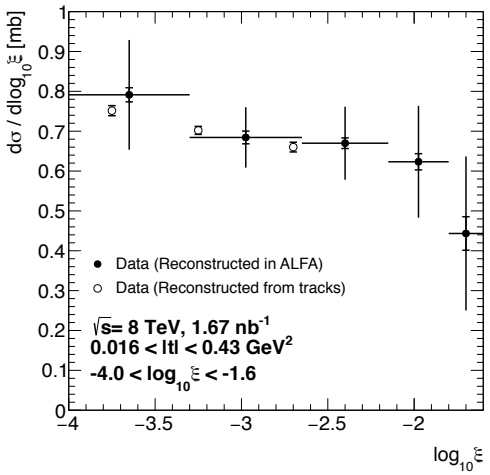

Figure 10.2: Cross-section differential in $\log_{10}\xi$ reconstructed from the proton in ALFA ('Data (Reconstructed in ALFA)'). Additionally, a cross-check of the cross-section is provided ('Data (Reconstructed from tracks)'), representing ξ as calculated from tracks with $p_{\mathrm{T}} > 100\,\mathrm{MeV}$ in the ID, derived from the ξ_{EPz} measurement. Both distributions are unfolded to the true ξ here. The inner error bars represent only statistical uncertainties while the outer error bars display the combination of statistical and systematic uncertainties on Data(ALFA). Only statistical uncertainties are displayed on Data(ID).

of the bin. This is necessitated by the steeply falling shape of the distribution. The Pythia8 A3 tune is used to determine the centre of gravity of each bin at the truth level and the resulting $|t|$ bin values are displayed in Table 10.1.

The t distribution, with corrected bin centres, is subjected to a fit of the form $\mathrm{d}\sigma/\mathrm{d}t = e^{A+Bt}$ [mb GeV^{-2}], with A and B as free parameters, such that A characterises the normalisation and B is the slope parameter. The covariance matrix from the unfolding response is used to obtain the statistical uncertainties in the fit as the raw statistical uncertainties output from the unfolding procedure can be slightly correlated. By performing this fit using the covariance matrix rather than the simple statistical uncertainties on each point, the statistical uncertainty is slightly reduced (by less than 10%), while the central value of the fit is unchanged. The resultant fit is,

$$\frac{\mathrm{d}\sigma}{\mathrm{d}t} = e^{2.65\ +\ 7.60t}\ [\mathrm{mb\ GeV}^{-2}], \tag{10.1}$$

Bin range [GeV^2]	Nominal Centre [GeV^2]	Corrected Centre [GeV^2]
$0.016 < \|t\| \leq 0.024$	0.0200	0.0200
$0.024 < \|t\| \leq 0.034$	0.0290	0.0289
$0.034 < \|t\| \leq 0.049$	0.0415	0.0413
$0.049 < \|t\| \leq 0.067$	0.0580	0.0578
$0.067 < \|t\| \leq 0.087$	0.0770	0.0767
$0.087 < \|t\| \leq 0.115$	0.1010	0.1005
$0.115 < \|t\| \leq 0.150$	0.1325	0.1322
$0.150 < \|t\| \leq 0.200$	0.1750	0.1740
$0.200 < \|t\| \leq 0.280$	0.2400	0.2369
$0.280 < \|t\| \leq 0.430$	0.3550	0.3437

Table 10.1: List of bin centres in $|t|$. The nominal bin centre where no shift is applied is compared to the bin centre determined from the centre of gravity of the bin.

with a χ^2/n.d.f = 8.128/8. The fitted function is overlaid on the data in Figure 10.3. The values of the fitted parameters A and B are compared to those achieved when fitting to the PYTHIA8 A2 and A3 MC samples in Table 10.2, where the full uncertainties are also quoted. The uncertainties are broken down into individual sources in Tables 10.3 and 10.4, in which the OB is observed to be the dominant source of uncertainty. The central value is obtained by fitting with statistical uncertainties only. The uncertainty is obtained by repeating the fit separately for each systematic shift and adding the resulting deviations from the central value in quadrature.

The slope parameter, $B = 7.60 \pm 0.23(\text{stat.}) \pm 0.22(\text{syst.})$ GeV^{-2} corresponds to a value averaged over the fiducial ξ range. Within this region, $< \log_{10}\xi > = -2.88 \pm 0.14$, where the central value is taken from the PYTHIA8 A3 tune and the uncertainty is the difference between the $< \log_{10}\xi >$ values in the A3 and A2 PYTHIA8 tunes. The measured B slope is compatible at the 1σ and 2σ levels with the predictions from the PYTHIA8 A2 and A3 MC models, respectively.

Distribution	A	B [GeV^{-2}]
PYTHIA8A2 (SS)	3.523 ± 0.006 (stat.)	7.82 ± 0.03 (stat.)
PYTHIA8A3 (DL)	3.046 ± 0.001 (stat.)	7.10 ± 0.01 (stat.)
Data	2.65 ± 0.03 (stat.) ± 0.05 (syst.)	7.60 ± 0.23 (stat.) ± 0.22 (syst.)

Table 10.2: Values of the A and B parameters and their uncertainties in fit of $\mathrm{d}\sigma/\mathrm{d}t = e^{A+Bt}$. The MC uncertainties are entirely statistical. The data uncertainties are separated into statistical (stat.) and systematic (syst.) uncertainties.

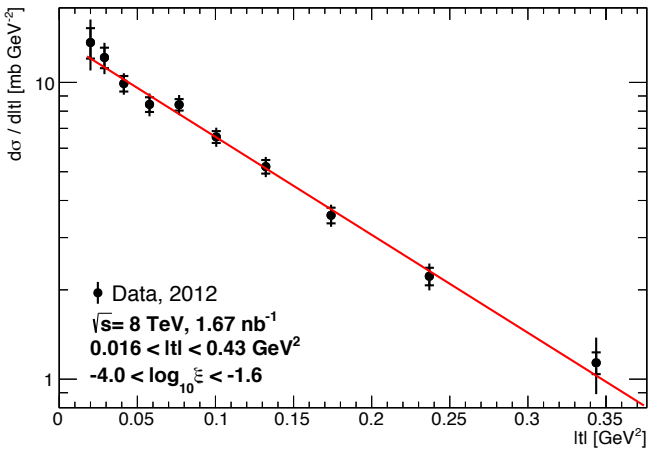

Figure 10.3: $\mathrm{d}\sigma/\mathrm{d}t$ with the fitted line: $\mathrm{d}\sigma/\mathrm{d}t = e^{2.65\ +\ 7.60t}$ superimposed. The inner error bars represent only statistical uncertainties while the outer error bars display the combination of statistical and systematic uncertainties.

Nominally, all bins are used in the exponential fit. The stability of this fit is probed by fitting the distribution independently with the first, the first two, the last and the last two data points removed. The resulting values of the parameters A and B, and their corresponding uncertainties, are displayed in Table 10.5. All variations are consistent within uncertainties.

10.2 Extraction of Pomeron Intercept

As described in Section 5.6, the SD cross-section differential in t and ξ can be constructed within Regge theory using a triple Pomeron amplitude, expressed in Equation 5.19, referred to herein as 'triple Pomeron'. It can also be modelled using a constant proton-Pomeron cross-section, as displayed in Equation 5.23, referred to as herein 'single Pomeron'.

To express the cross-section purely differentially in ξ, one must integrate over the

Uncertainty source	**Absolute uncertainty**
Statistical	0.0300
ALFA Reco Eff Down	0.0028
ALFA Reco Eff Up	-0.0033
Alignment (horizontal)	-0.0004
Alignment (optimisation)	-0.0008
Alignment (rotation)	-0.0015
CD Shape	0.0006
CD Shape Symmetrised	-0.0006
Cross-Sections Down	0.0113
Cross-Sections Up	-0.0389
Luminosity down	0.0275
Luminosity up	-0.0275
Mbts Charge Threshold 3σ	-0.0010
Mbts Charge Threshold 5σ	0.0064
Overlay Background Down	0.0233
Overlay Background Up	-0.0246
Track Reco Eff Down	0.0000
Track Reco Eff Up	0.0001
Trigger Eff Down	0.0061
Trigger Eff Up	-0.0061
Unfolding	0.0062
Unfolding Symmetrised	-0.0062
Total Systematic Uncertainty	+0.0394 -0.0544
Total Uncertainty	0.0621

Table 10.3: Sources of uncertainty in the determination of the A parameter in the fit: $\mathrm{d}\sigma/\mathrm{d}t = e^{A+Bt}$.

fiducial t range, obtaining:

$$\frac{\mathrm{d}\sigma_{SD}}{\mathrm{d}\log_{10}(\xi)} \propto \left(\frac{1}{\xi}\right)^{\alpha(0)-1} \frac{1}{B}\left(e^{Bt_{\mathrm{high}}} - e^{Bt_{\mathrm{low}}}\right) \ , \tag{10.2}$$

and,

$$\frac{\mathrm{d}\sigma_{SD}}{\mathrm{d}\log_{10}(\xi)} \propto \left(\frac{1}{\xi}\right)^{2\alpha(0)-2} \frac{1}{B}\left(e^{Bt_{\mathrm{high}}} - e^{Bt_{\mathrm{low}}}\right) \ , \tag{10.3}$$

for the triple and single Pomeron approaches to expressing the SD cross-section ξ dependency, respectively. The limits from the integration are defined by the fiducial region to be, $t_{\mathrm{high}} = -0.016\,\mathrm{GeV}^2$ and $t_{\mathrm{low}} = -0.43\,\mathrm{GeV}^2$, while $B = B_0 - 2\alpha' \ln\xi$ as in Equation 5.18. The only difference between Equations 10.2 and 10.3 is the power to which the ξ term is raised. Thus, it is possible for both cross-section formalisms

Uncertainty source	**Absolute uncertainty [GeV^{-2}]**
Statistical	0.2264
ALFA Reco Eff Down	0.0035
ALFA Reco Eff Up	-0.0025
Alignment (horizontal)	0.0365
Alignment (optimisation)	0.0149
Alignment (rotation)	0.0297
CD Shape	-0.0068
CD Shape Symmetrised	0.0068
Cross-Sections Down	0.0074
Cross-Sections Up	-0.0610
Luminosity down	-0.0186
Luminosity up	0.0195
Mbts Charge Threshold 3σ	-0.0316
Mbts Charge Threshold 5σ	-0.0307
Overlay Background Down	0.1913
Overlay Background Up	-0.2002
Track Reco Eff Down	0.0000
Track Reco Eff Up	0.0001
Trigger Eff Down	0.0169
Trigger Eff Up	-0.0170
Unfolding	0.0174
Unfolding Symmetrised	-0.0177
Total Systematic Uncertainty	+0.2003 -0.2162
Total Uncertainty	0.3131

Table 10.4: Sources of uncertainty in the determination of the B parameter in the fit: $\mathrm{d}\sigma/\mathrm{d}t = e^{A+Bt}$.

to be described by the fit:

$$\frac{\mathrm{d}\sigma_{SD}}{\mathrm{d}\log_{10}(\xi)} = C \cdot 10^{D\log_{10}\xi} \cdot \frac{1}{B(\xi)} \cdot \left(e^{B(\xi)t_{\mathrm{high}}} - e^{B(\xi)t_{\mathrm{low}}}\right) \ , \tag{10.4}$$

where C and D are free parameters. In the triple Pomeron approach, $D = 1-\alpha(0) \equiv -\epsilon$, while in the single Pomeron formalism, $D = 2 - 2\alpha(0) \equiv -2\epsilon$. The value of B_0 is calculated using the measured value of B within this analysis, $B = 7.60 \pm 0.31$, $\alpha' = 0.25 \pm 0.25\,\mathrm{GeV}^{-2}$ and a mean value of ξ, as previously determined to be $< \log_{10}\xi >= -2.88 \pm 0.14$. The systematic uncertainties are propagated through to the fit in Equation 10.4. The central value of α' used is that which is most compared to in literature, some examples of which can be found in [113, 114][1]. This

[1]The combination $\alpha' = 0.25\,\mathrm{GeV}^{-2}$ and $\alpha(0) = 1.08$ is often referred to as the 'soft Pomeron',

Fit range	$\boldsymbol{A}$	$\boldsymbol{B}[\mathbf{GeV}^{-2}]$
$0.016 < \|t\| \leq 0.430$	2.65 ± 0.06	7.60 ± 0.31
$0.024 < \|t\| \leq 0.430$	2.64 ± 0.07	7.55 ± 0.42
$0.034 < \|t\| \leq 0.430$	2.65 ± 0.05	7.63 ± 0.21
$0.016 < \|t\| \leq 0.280$	2.67 ± 0.08	7.86 ± 0.35
$0.016 < \|t\| \leq 0.200$	2.67 ± 0.09	7.94 ± 0.57

Table 10.5: Values of the A and B parameters and their uncertainties in the fit of $\mathrm{d}\sigma/\mathrm{d}t = e^{A+Bt}$, when fitted over different regions of the data distribution.

value of α' is the default used in the PYTHIA8 MC tunes considered within this analysis. The uncertainty is conservatively taken to be 100% with α' varying from 0 to $0.5\,\mathrm{GeV}^{-2}$. If the analysis were to be performed double differentially it would be possible to constrain α' and significantly reduce this uncertainty. However, this is not within the scope of this analysis. The value of B_0 is varied simultaneously with each variation of α', B and $< \log_{10}\xi >$ to be consistent with the measured B value.

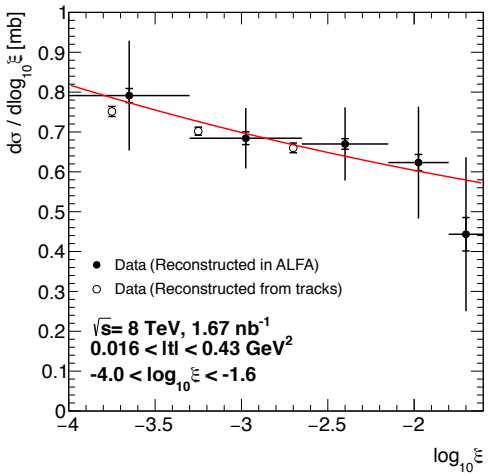

Figure 10.4: Cross-section differential in $\log_{10}\xi$ reconstructed from the proton in ALFA ('Data (Reconstructed from ALFA)') and from the ID tracks with $p_{\mathrm{T}} > 100\,\mathrm{MeV}$ ('Data (Reconstructed from tracks)'). Both distributions are unfolded to the true ξ. The inner error bars represent only statistical uncertainties while the outer error bars display the combination of statistical and systematic uncertainties on Data(ALFA). Only statistical uncertainties are displayed on Data(ID). The fit detailed in Equation 10.4 is overlaid with $C = 2.6\,\mathrm{mb}$ and $D = -0.13$.

or the 'Donnachie-Landshoff' Pomeron owing to their parameterisation which described almost all experimental data in an elegant and economic form [64, 68]. The $\alpha' = 0.25\,\mathrm{GeV}^{-2}$ parameterisation actually predates this [115].

Figure 10.4 displays the fitted form of Equation 10.4 to the measured ξ cross-section using the values of ξ reconstructed from the scattered proton in ALFA. The extracted values of the parameters C and D for both methods of ξ reconstruction and the PYTHIA8 MC samples are displayed in Table 10.6. The ALFA and ID methods of reconstructing ξ are in agreement within statistical uncertainties. Tables 10.7 and 10.8 display the individual sources of uncertainty for the fit to the data from the scattered proton in ALFA. The leading uncertainty on the D parameter (the parameter of interest, as the C parameter just concerns the normalisation) stems from the α' uncertainty. As this is a parameter used in the fits and does not originate from the data points, it is possible for it to be shrunk and the fit performed to re-evaluate the uncertainty if a better constraint on α' becomes available in the future. It is listed as a separate uncertainty category in Table 10.6. The dominant uncertainty contained within the analysis method arises from the unfolding uncertainty, which is due to the relatively poor resolution of the energy reconstruction of the proton in ALFA at low ξ and the large migrations that thus occur.

Distribution	**C [mb]**	**D**
PYTHIA8A2 (SS)	14.0 ± 0.2	-0.005 ± 0.002
PYTHIA8A3 (DL)	3.43 ± 0.01	-0.1408 ± 0.0005
Data(ALFA)	2.6 ± 0.1 (stat.) ± 1.5 (syst.) ± 1.4 (α' uncert.)	-0.13 ± 0.01 (stat.) ± 0.08 (syst.) ± 0.07 (α' uncert.)
Data(ID)	2.8 ± 0.2 (stat.)	-0.12 ± 0.01 (stat.)

Table 10.6: Values of the C and D parameters and their uncertainties in the fit of $\mathrm{d}\sigma/\mathrm{dlog}_{10}\,\xi$ as displayed in Equation 10.4. The MC uncertainties are entirely statistical. The data uncertainties are separated into statistical (stat.), systematic (syst.) and α' uncertainties (α' uncert.) for the Data(ALFA) values, and are purely statistical for Data(ID) values.

Calculating $\alpha(0)$ from the fitted D values in both the single and triple Pomeron approaches results in the values listed in Tables 10.9 and 10.10, respectively. In the single Pomeron approach, which is used in PYTHIA8, the values from the fits to the truth level MC information return the 1.00 and 1.07 values that are input as steering parameters to the A2 and A3 MC tunes, respectively. The data favour the DL Pomeron flux model, although have large systematic uncertainties.

Uncertainty source	**Absolute uncertainty [mb]**
Statistical	0.1439
$< \log_{10}\xi >= -2.74$	0.0677
$< \log_{10}\xi >= -3.02$	-0.0669
$B = 7.29$ [GeV^{-2}]	-0.1280
$B = 7.91$ [GeV^{-2}]	0.1314
α' = 0.0	1.4096
α' = 0.5	-0.9330
ALFA Reco Eff Down	0.0061
ALFA Reco Eff Up	-0.0073
Alignment (horizontal)	-0.2430
Alignment (optimisation)	0.0231
Alignment (rotation)	-0.0623
CD Shape	0.7223
CD Shape Symmetrised	-0.5145
Cross-Sections Down	0.0277
Cross-Sections Up	0.0021
Luminosity down	0.0631
Luminosity up	-0.0613
Mbts Charge Threshold 3σ	0.0102
Mbts Charge Threshold 5σ	-0.0264
Overlay Background Down	0.8688
Overlay Background Up	-0.7148
Track Reco Eff Down	0.0003
Track Reco Eff Up	0.0004
Trigger Eff Down	0.0098
Trigger Eff Up	-0.0098
Unfolding	-0.7743
Unfolding Symmetrised	0.9741
Total Systematic Uncertainty	+2.0591 -1.5278
Total Uncertainty	2.0641

Table 10.7: Sources of uncertainty in the determination of the C parameter in the fit to $d\sigma/d\log_{10}\xi$ displayed in Equation 10.4 of ξ reconstructed from the scattered proton.

Uncertainty source	**Absolute uncertainty**
Statistical	0.0083
$< \log_{10}\xi >= -2.74$	0.0007
$< \log_{10}\xi >= -3.02$	-0.0008
$B = 7.29$ [GeV^{-2}]	-0.0015
$B = 7.91$ [GeV^{-2}]	0.0014
α' = 0.0	0.0648
α' = 0.5	-0.0656
ALFA Reco Eff Down	-0.0001
ALFA Reco Eff Up	0.0001
Alignment (horizontal)	-0.0115
Alignment (optimisation)	0.0016
Alignment (rotation)	-0.0020
CD Shape	0.0415
CD Shape Symmetrised	-0.0372
Cross-Sections Down	-0.0002
Cross-Sections Up	0.0085
Luminosity down	-0.0001
Luminosity up	0.0001
Mbts Charge Threshold 3σ	0.0011
Mbts Charge Threshold 5σ	-0.0018
Overlay Background Down	0.0328
Overlay Background Up	-0.0365
Track Reco Eff Down	0.0000
Track Reco Eff Up	0.0000
Trigger Eff Down	-0.0004
Trigger Eff Up	0.0004
Unfolding	-0.0533
Unfolding Symmetrised	0.0487
Total Systematic Uncertainty	+0.0972 -0.1000
Total Uncertainty	0.1003

Table 10.8: Sources of uncertainty in the determination of the D parameter in the fit to $d\sigma/d\log_{10}\xi$ detailed in Equation 10.4 of ξ reconstructed from the scattered proton.

Distribution	$\boldsymbol{\alpha(0)}$
PYTHIA8 A2 (SS)	1.002 ± 0.001 (stat.)
PYTHIA8 A3 (DL)	1.070 ± 0.000 (stat.)
Data(ALFA)	1.07 ± 0.00 (stat.) ± 0.05 (syst.)
Data(ID)	1.06 ± 0.01 (stat.)

Table 10.9: Values of the Pomeron intercept, $\alpha(0)$, for data and MC, extracted under a constant proton-Pomeron cross-section ('single Pomeron'). The MC uncertainties are entirely statistical and are negligible.The data uncertainties are separated into statistical (stat.) and systematic (syst.) uncertainties for Data(ALFA) and are purely statistical uncertainties for Data(ID).

Distribution	$\boldsymbol{\alpha(0)}$
Data(ALFA)	1.13 ± 0.01 (stat.) ± 0.10 (syst.)
Data(ID)	1.12 ± 0.01 (stat.)

Table 10.10: Values of the Pomeron intercept, $\alpha(0)$, for data extracted under the full triple Pomeron cross-section formalism. The data uncertainties are separated into statistical (stat.) and systematic (syst.) uncertainties for Data(ALFA) and are purely statistical uncertainties for Data(ID).

10.3 Cross-section Measurement

Integrating the cross-section across the fiducial region, $-4.0 < \log_{10}\xi \leq -1.6$ and $0.016 < |t| < 0.43\,\mathrm{GeV}^2$, results in $\sigma_{\mathrm{SD}}^{\mathrm{fiducial}(\xi,t)} = 1.59 \pm 0.13\,\mathrm{mb}$. The full uncertainties on this measurement are listed in Table 10.11. The dominant uncertainty is observed to be the size of the overlay background.

Uncertainty source	**Absolute uncertainty [mb]**
Statistical	0.0332
ALFA Reco Eff Down	0.0054
ALFA Reco Eff Up	-0.0060
Alignment (horizontal)	0.0079
Alignment (optimisation)	0.0031
Alignment (rotation)	0.0045
CD Shape	-0.0002
CD Shape Symmetrised	0.0002
Cross-Sections Down	0.0196
Cross-Sections Up	-0.0735
Luminosity down	0.0413
Luminosity up	-0.0400
Mbts Charge Threshold 3σ	-0.0074
Mbts Charge Threshold 5σ	0.0021
Overlay Background Down	0.0926
Overlay Background Up	-0.0926
Track Reco Eff Down	0.0000
Track Reco Eff Up	0.0001
Trigger Eff Down	0.0142
Trigger Eff Up	-0.0141
Unfolding	0.0140
Unfolding Symmetrised	-0.0140
Total Systematic Uncertainty	+0.1058 -0.1267
Total Uncertainty	0.1310

Table 10.11: Sources of uncertainty in the extraction of the fiducial cross-section.

Under the assumption of an exponential shape of the t distribution for all $|t|$, which is supported by the measurement in this analysis, the cross-section can be extrapolated to cover the full t range through the equation,

$$\sigma_{\mathrm{SD}}^{\mathrm{fiducial}(\xi)} = \frac{\int_{-\infty}^{0} e^{A+Bt}\mathrm{d}t}{\int_{t_{\mathrm{low}}}^{t_{\mathrm{high}}} e^{A+Bt}\mathrm{d}t} \times \sigma_{\mathrm{SD}}^{\mathrm{fiducial}(\xi,t)} = \frac{1}{e^{Bt_{\mathrm{high}}} - e^{Bt_{\mathrm{low}}}} \times \sigma_{\mathrm{SD}}^{\mathrm{fiducial}(\xi,t)} \,. \quad (10.5)$$

This extrapolation results in $\sigma_{\mathrm{SD}}^{\mathrm{fiducial}(\xi)} = 1.88 \pm 0.15\,\mathrm{mb}$, where the uncertainties on $\sigma_{\mathrm{SD}}^{\mathrm{fiducial}(\xi,t)}$, A and B are fully propagated through. This result can be compared with the predicted cross-section within the A3 tune of PYTHIA8, $\sigma_{\mathrm{SD}}^{\mathrm{fiducial}(\xi)} = 2.98\,\mathrm{mb}$ with negligible statistical uncertainty. In Section 10.2 it is observed that the shape of the measured ξ differential cross-section is consistent with that predicted in the PYTHIA8 A3 tune, so an estimate of the total cross-section can crudely be obtained by scaling the predicted total SD cross-section in the A3 tune by the ratio observed within the fiducial region. This simple scaling results in $\sigma_{\mathrm{SD}} = 7.9\,\mathrm{mb}$, where the uncertainties are inestimable due to the poorly constrained low and high ξ behaviour. The cross-sections at all stages of the extrapolation, along with the predictions from the two PYTHIA8 tunes considered, are displayed in Table 10.12.

Distribution	$\boldsymbol{\sigma_{\mathrm{SD}}^{\mathrm{fiducial}(\xi,t)}}$ **[mb]**	$\boldsymbol{\sigma_{\mathrm{SD}}^{\mathrm{fiducial}(\xi)}}$ **[mb]**	$\boldsymbol{\sigma_{\mathrm{SD}}}$ **[mb]**
PYTHIA8 A2 (SS)	3.69 ± 0.00 (stat.)	4.35 ± 0.00 (stat.)	12.48
PYTHIA8 A3 (DL)	2.52 ± 0.00 (stat.)	2.98 ± 0.00 (stat.)	12.48
Data	1.59 ± 0.03 (stat.) ± 0.13 (syst.)	1.88 ± 0.04 (stat.) ± 0.15 (syst.)	7.9

Table 10.12: The SD cross-section within the analysis fiducial region, extrapolated across all t and scaled up to the entire phase space. The MC statistical uncertainties are negligible. The data uncertainties are separated into statistical (stat.) and systematic (syst.) uncertainties. No uncertainty is provided for the full cross-section as it is simply extracted under the assumption of naive scaling of the PYTHIA8 A3 tune.

10.4 Comparisons to Previous Results

This analysis constitutes the first measurement of single dissociative diffractive processes with a tagged forward proton, enabling very strong discrimination between SD and DD, demonstrated by the lack of a significant contribution from DD events in Figure 8.1. A similar, but unpublished, measurement to the one presented here was performed by the TOTEM collaboration. Preliminary results using data collected at $\sqrt{s} = 7\,\mathrm{TeV}$ were obtained [116]. It should be noted that these results were never officially published and the TOTEM collaboration no longer presents them. However, they are included here as they are the only other directly comparable LHC measurement. The measurement was performed in three ξ bins, defined by

the presence or absence of activity in three separate detector components used to identify the dissociative X system, whilst requiring a tagged forward proton. This measurement technique results in three separate values for the B slope, displayed in Figure 10.5 where each value is plotted at the centre of ξ range in which it is quoted. The measured B slope in this analysis of 7.60 ± 0.31 GeV^{-2} is displayed at the mean ξ value, $< \log_{10} \xi > \; = -2.88$. The ATLAS and TOTEM data are consistent with the expected logarithmic fall with ξ. The measurement performed in this analysis is of far higher precision than the TOTEM result.

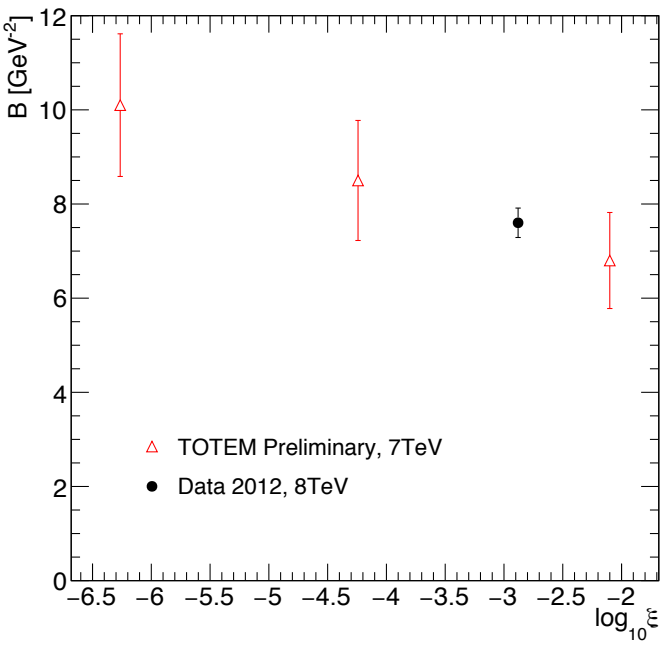

Figure 10.5: B slope as a function of $\log_{10}(\xi)$. Results from the presented are compared with preliminary TOTEM results [116]. Total uncertainties are displayed on all data points.

The TOTEM preliminary results also include integrated cross-sections, extrapolated across all t, for each of the three ξ bins defined by the distinct measurement regions. These values are presented in Figure 10.6 after division by their range in ξ to produce differential cross-sections. The TOTEM results are plotted in the centre of their ξ range. The differential cross-section in ξ as measured within this analysis is presented in the same figure after extrapolation across the whole t range. A good

agreement is observed between the measured differential cross-section in this analysis and the TOTEM preliminary value in the range $-5.9 < \log_{10}(\xi) \leq -2.6$. A 2σ discrepancy is observed in the high ξ region. This analysis is not able to probe the very low ξ region explored by TOTEM.

Figure 10.6 also displays CMS cross-sections obtained from a rapidity gap-based analysis with no proton tagging available [94]. An enriched sample of SD candidates is obtained by requiring a rapidity gap extending through the CASTOR forward calorimeter [17], implying that the mass of the 'Y' system satisfies $\log_{10} M_Y < 0.5$ in DD contributions ($pp \to XY$). It is not possible to say precisely how much DD contamination remains, though it can reasonably be expected to be small. A good agreement is observed between the measurement presented in this analysis and the CMS result without subtracting any DD contribution. Although both the CMS and the TOTEM preliminary results were obtained at $\sqrt{s} = 7\,\text{TeV}$ rather than 7 TeV, the difference in the cross-sections should be at the percent level as $\sigma_{\text{SD}}(s) \propto s^{\epsilon}$.

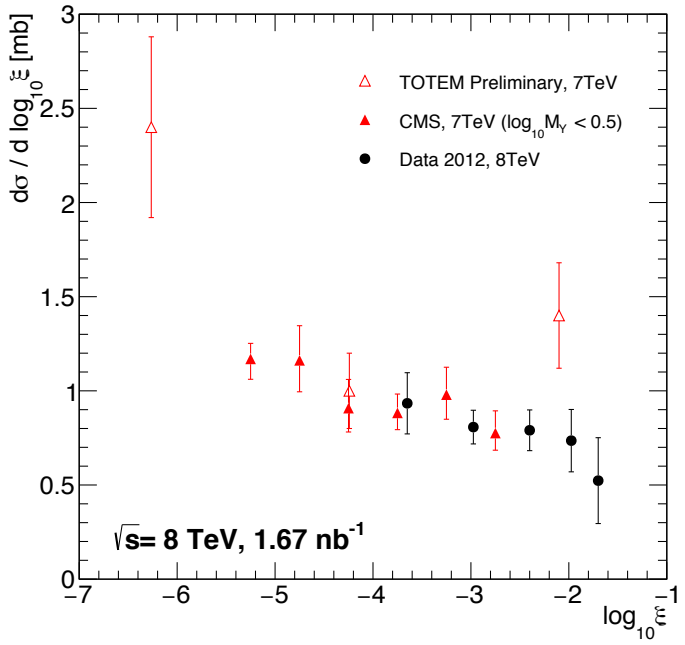

Figure 10.6: $\mathrm{d}\sigma/\mathrm{d}\log_{10}(\xi)$. Comparison of results with preliminary TOTEM results [116] and CMS rapidity gap cross-sections [94]. Total uncertainties are displayed on all data points.

CHAPTER 11

Summary

The first fiducial and differential cross-sections for single dissociative diffraction using forward proton identification are presented. In addition, the forward proton trajectory is reconstructed, providing access to its kinematics. This measurement was performed using a dedicated low pile-up sample collected in 2012 with $\sqrt{s} = 8\,\text{TeV}$ on which the elastic cross-section has already been measured and published [73]. The main MC generator tune used in this analysis is the most recent ATLAS tune to ATLAS inelastic and diffraction measurements, the A3 tune of Pythia8.

Events are selected using a proton tag trigger in the ALFA detectors on one side of the interaction point and a minimum bias scintillator trigger on the other side. In addition to a tighter offline selection in the components used for the triggering, it is required that a track with transverse momentum above 200 MeV is reconstructed in the inner tracking detector. No other selection is applied, to ensure the measurement is as inclusive as possible. This selection defines the fiducial region to be $-4.0 < \log_{10}\xi < -1.6$ (corresponding to $80 < M_X < 1270\,\text{GeV}$) and

$0.016 < |t| < 0.43\,\text{GeV}^2$. Over two thirds of selected events are SD signal according to MC simulation. Background subtraction is performed using MC samples as well as a data-driven technique involving measurement of the rate of protons tagged in the ALFA detectors in a control region that is highly signal-suppressed. This rate is then used to construct a background from uncorrelated signals in the central ATLAS detectors and the ALFA detectors. Small trigger and ALFA reconstruction inefficiencies are accounted for before the background-subtracted data are unfolded to correct for detector effects such as limited acceptance and poor reconstruction resolution. The resulting distributions are corrected for the luminosity and presented as differential cross-sections as a function of: the squared four-momentum transfer, Mandelstam-t; the fractional energy loss of the proton, ξ, and the gap in pseudorapidity between the inner detector edge ($|\eta| = 2.5$) on the proton-tagged side of the interaction point and the nearest charged particle with $p_T > 200\,\text{MeV}$ in the region $|\eta| \leq 2.5$, $\Delta\eta^F$. The dominant sources of uncertainty stem from the unfolding procedure and the background subtraction.

The cross-section differential in $\Delta\eta^F$ displays a plateau in the region $1.5 \lesssim \Delta\eta \lesssim 3.5$ while outside of this region acceptance effects and the fiducial range definition in ξ alter the shape. The plateau is characteristic of diffractive scattering and is observed in previous rapidity gap based analyses. The cross-section is compared to two ATLAS tunes of the Pythia8 generator, both of which over-predict the cross-section across the full range of this measurement. This normalisation discrepancy is consistent with that observed in previous ATLAS analyses which demonstrated that the MC predicted the rapidity gap cross-section to be larger than was observed in the data for a combination of SD and DD events.

The SD cross-section is also presented differentially in t. It is well described by an exponential fit of the form $\mathrm{d}\sigma/\mathrm{d}t \propto e^{Bt}$, where $B = 7.60 \pm 0.31\,\text{GeV}^{-2}$ is extracted. This measurement is consistent with the predicted slopes in the Pythia8 A2 and A3 tunes at the 1σ and 2σ levels, respectively. The high precision on this measurement renders it useful as an input to future models.

Two methods are used to reconstruct the ξ quantity: one from the scattered proton and one from sampling the dissociated 'X'-system in the inner detector. The full systematic uncertainties are evaluated on the proton-based method while only statistical uncertainties are presented on the X-system method which is purely used as a cross-check. The two reconstruction methods have very different backgrounds and response matrices in the unfolding procedure, yet produce fully consistent cross-section results. The results are observed to be in good agreement with the rapidity gap cross-sections presented by the CMS Collaboration, in which the DD contribution was suppressed through a rapidity gap cut, but still provides an unspecified contamination. The cross-section from the proton-tagged method is interpreted in Regge phenomenology, using a triple Pomeron-based description of the cross-section. A fit to the data yields $\alpha(0) = 1.13 \pm 0.10$. The results are also interpreted using a constant proton-Pomeron cross-section, where $\alpha(0) = 1.07 \pm 0.05$ is extracted. Both values of $\alpha(0)$ under different interpretations are well predicted by the PYTHIA8 A3 tune. The uncertainties on the measurements of $\alpha(0)$ are large, although they are dominated by the conservative uncertainty applied to the Pomeron slope, α', in the construction of the fit. The measured cross-section values are still of use in model generation as the value of α' is an input to models, enabling them to be tested against the results of this analysis without the large uncertainty attached to α'.

The cross-section is measured within the fiducial region of this analysis to be $\sigma_{\mathrm{SD}}^{(-4.0<\log_{10}\xi<-1.6\ ,\ 0.016<|t|<0.43)} = 1.59 \pm 0.13\,\mathrm{mb}$. This value is inconsistent with the predicted value in the PYTHIA8 tunes considered in this analysis. The favoured MC sample in this analysis, the PYTHIA8 A3 tune which reproduces the measured shapes of all the analysis variables, predicts the cross-section within the fiducial region to be a factor of 1.58 above that which is measured. The cross-section, fiducial in t and ξ, is extrapolated across all t using the extracted exponential slope parameter, resulting in $\sigma_{\mathrm{SD}}^{(-4.0<\log_{10}\xi<-1.6)} = 1.88 \pm 0.15\,\mathrm{mb}$. Under the assumption that the A3 tune of PYTHIA8 describes the shape of the ξ distribution perfectly outside of the fiducial region, a simple scaling can be performed using the measured normalisation discrepancy within the fiducial region. Under such scaling, the total

SD cross-section is 7.9 mb, although no uncertainties are quoted on this value as the low and high ξ behaviour of the cross-section is not constrained by data in this energy regime.

The author aims for this analysis to be published on behalf of the ATLAS Collaboration early in 2019 as it is currently in the analysis review process. When published it will represent the most precise measurements of the SD process in the LHC era and will directly improve the understanding of the dynamics of soft interactions between protons and challenge model-makers in the tuning of future simulations. Additionally, many other analyses will benefit in the form of a better understanding of their background processes.

The prospects for improvement upon this measurement at ATLAS are high. Several data samples have been collected at $\sqrt{s} = 13\,\text{TeV}$ with both the ALFA and AFP forward detectors. The acceptance of AFP enables the probing of the high ξ region, to which this analysis is insensitive. The analysis of these data samples is already underway at the time of writing and many of the techniques developed within this analysis are being used in these ongoing measurements. Furthermore, the results of this analysis provide a strong motivation for the performance of this measurement double-differentially, enabling the probing of the t and ξ interdependence.

REFERENCES

[1] M. Wessels, "Calibration and Performance of the ATLAS Level-1 Calorimeter Trigger with LHC Collision Data," *Physics Procedia*, vol. 37, pp. 1841 – 1848, 2012.

[2] G. Arnison *et al.*, "Experimental observation of isolated large transverse energy electrons with associated missing energy at $\sqrt{s} = 540$ GeV," *Physics Letters B*, vol. 122, no. 1, pp. 103 – 116, 1983.

[3] M. Banner *et al.*, "Observation of single isolated electrons of high transverse momentum in events with missing transverse energy at the CERN pp collider," *Physics Letters B*, vol. 122, no. 5, pp. 476 – 485, 1983.

[4] G. Arnison *et al.*, "Experimental Observation of Events with Large Missing Transverse Energy Accompanied by a Jet Or a Photon(s) in p anti-p Collisions at $\sqrt{s} = 540$ GeV," *Phys. Lett.*, vol. 139B, p. 115, 1984.

[5] ATLAS Collaboration, "Observation of a new particle in the search for the Standard Model Higgs boson with the ATLAS detector at the LHC," *Phys. Lett.*, vol. B716, pp. 1–29, 2012.

[6] CMS Collaboration, "Observation of a new boson at a mass of 125 GeV with the CMS experiment at the LHC," *Phys. Lett.*, vol. B716, pp. 30–61, 2012.

[7] F. Marcastel, "CERN's Accelerator Complex. La chaîne des accélérateurs du CERN," *OPEN-PHO-CHART-2013-001*, Oct 2013. General Photo.

[8] D. J. Simon, "The CERN PS complex: a versatile particle factory," *CERN-PS-96-0190-DI*.

[9] L. Evans and P. Bryant, "LHC Machine," *JINST*, vol. 3, p. S08001, 2008.

[10] CERN. Geneva, "LEP Design Report: Vol.2. The LEP Main Ring," Tech. Rep. CERN-LEP-84-01, June 1984.

[11] S. van der Meer, "Calibration of the effective beam height in the ISR," Tech. Rep. CERN-ISR-PO-68-31, CERN, Geneva, 1968.

[12] "ATLAS Experiment - Public Results." `https://twiki.cern.ch/twiki/bin/view/AtlasPublic/`. Accessed: 25/04/2018.

[13] A. Hoecker, "Physics at the LHC Run-2 and Beyond," in *2016 European School of High-Energy Physics (ESHEP 2016) Skeikampen, Norway, June 15-28, 2016*, 2016.

[14] ALICE Collaboration, "The ALICE experiment at the CERN LHC," *JINST*, vol. 3, p. S08002, 2008.

[15] J. C. Collins and M. J. Perry, "Superdense Matter: Neutrons Or Asymptotically Free Quarks?," *Phys. Rev. Lett.*, vol. 34, p. 1353, 1975.

[16] N. Cabibbo and G. Parisi, "Exponential hadronic spectrum and quark liberation," *Physics Letters B*, vol. 59, no. 1, pp. 67 – 69, 1975.

[17] CMS Collaboration, "The CMS Experiment at the CERN LHC," *JINST*, vol. 3, p. S08004, 2008.

[18] J. H. Christenson, J. W. Cronin, V. L. Fitch, and R. Turlay, "Evidence for the 2π Decay of the K_2^0 Meson," *Phys. Rev. Lett.*, vol. 13, pp. 138–140, Jul 1964.

[19] A. A. Alves, Jr. *et al.*, "The LHCb Detector at the LHC," *JINST*, vol. 3, p. S08005, 2008.

[20] A. D. Sakharov, "Violation of CP Invariance, C asymmetry, and baryon asymmetry of the universe," *Pisma Zh. Eksp. Teor. Fiz.*, vol. 5, pp. 32–35, 1967.

[21] ATLAS Collaboration, "Studies of the performance of the ATLAS detector using cosmic-ray muons," *The European Physical Journal C*, vol. 71, 2011.

[22] J. Pequenao and P. Schaffner, "An computer generated image representing how ATLAS detects particles," *CERN-EX-1301009*, Jan 2013.

[23] ATLAS Collaboration, "The ATLAS Experiment at the CERN Large Hadron Collider," *JINST*, vol. 3, p. S08003, 2008.

[24] C. Gemme, "The ATLAS upgrade program," in *Proceedings, 2nd Conference on Large Hadron Collider Physics Conference (LHCP 2014): New York, USA, June 2-7, 2014*, 2014.

[25] J. Pequenao, "Computer generated image of the ATLAS inner detector," *CERN-GE-0803014*, Mar 2008.

[26] ATLAS Collaboration, "Performance of the ATLAS Transition Radiation Tracker in Run 1 of the LHC: tracker properties," *Journal of Instrumentation*, vol. 12, May 2017.

[27] B. Dowler *et al.*, "Performance of the ATLAS Hadronic End-Cap Calorimeter in Beam Tests," Tech. Rep. ATL-LARG-2001-019, Max-Planck Inst., München, Oct 2001.

[28] E. Abat *et al.*, "Combined performance studies for electrons at the 2004 ATLAS combined test-beam," *JINST*, vol. 5, p. P11006, 2010.

[29] ATLAS Collaboration, "The ATLAS Data Acquisition and High Level Trigger system," *JINST*, vol. 11, no. 06, p. P06008, 2016.

[30] Atlas Collaboration, "Performance of the ATLAS trigger system in 2015," *The European Physical Journal C*, vol. 77, p. 317, May 2017.

[31] A. Foster, "Low energy observables with the ATLAS experiment," *Nuclear and Particle Physics Proceedings*, vol. 294-296, pp. 37 – 41, 2018.

[32] F. Abe *et al.*, "Observation of top quark production in $\bar{p}p$ collisions," *Phys. Rev. Lett.*, vol. 74, pp. 2626–2631, 1995.

[33] S. Abachi *et al.*, "Observation of the top quark," *Phys. Rev. Lett.*, vol. 74, pp. 2632–2637, 1995.

[34] M. Baak *et al.*, "The global electroweak fit at NNLO and prospects for the LHC and ILC," *Eur. Phys. J.*, vol. C74, p. 3046, 2014.

[35] M. Schioppa, "BSM Higgs Searches with the ATLAS Experiment," *Acta Phys. Polon.*, vol. B47, pp. 1565–1579, 2016.

[36] M. E. Peskin, "Supersymmetry in Elementary Particle Physics," in *Proceedings of Theoretical Advanced Study Institute in Elementary Particle Physics : Exploring New Frontiers Using Colliders and Neutrinos (TASI 2006): Boulder, Colorado, June 4-30, 2006*, pp. 609–704, 2008.

[37] J. R. Ellis, "Dark matter and dark energy: Summary and future directions," *Phil. Trans. Roy. Soc. Lond.*, vol. A361, p. 2607, 2003.

[38] C. Alpigiani, "Searches for Dark Matter in ATLAS," in *5th Large Hadron Collider Physics Conference (LHCP 2017) Shanghai, China, May 15-20, 2017*, 2017.

[39] M. Spousta, "Overview of new results from ATLAS heavy ion physics program," *Nucl. Part. Phys. Proc.*, vol. 23, p. 28, 2016.

[40] U. Amaldi *et al.*, "The energy dependence of the proton-proton total cross-section for centre-of-mass energies between 23 and 53 GeV," *Physics Letters B*, vol. 44, no. 1, pp. 112 – 118, 1973.

[41] ATLAS Collaboration, "Measurement of the total cross section from elastic scattering in pp collisions at $\sqrt{s} = 7$ TeV with the ATLAS detector," *Nucl. Phys.*, vol. B889, pp. 486–548, 2014.

[42] ATLAS Collaboration, "Technical Design Report for the ATLAS Forward Proton Detector," Tech. Rep. CERN-LHCC-2015-009, May 2015.

[43] ATLAS Collaboration, "The ALFA Roman Pot Detectors of ATLAS," *JINST*, vol. 11, no. 11, p. P11013, 2016.

[44] T. Sykora, "Physics program of ALFA and precision luminosity measurement in ATLAS," Tech. Rep. ATL-PHYS-PROC-2011-250, CERN, Geneva, Nov 2011.

[45] H. Stenzel, "Measurement of Single Diffraction in special runs." `http://www.physik.uni-giessen.de/atlas/publications/sdnote.pdf`, 2007. Accessed: 11/07/2018.

[46] ATLAS Collaboration, "Luminosity determination in pp collisions at $\sqrt{s} = 8$ TeV using the ATLAS detector at the LHC," *Eur. Phys. J.*, vol. C76, no. 12, p. 653, 2016.

[47] C.-T. Collaboration, "CMS-TOTEM Precision Proton Spectrometer," Tech. Rep. CERN-LHCC-2014-021, Sep 2014.

[48] TOTEM Collaboration, "The TOTEM Experiment at the CERN Large Hadron Collider," *Journal of Instrumentation*, vol. 3, no. 08, p. S08007, 2008.

[49] E. Fermi, "Sulla quantizzazione del gas perfetto monoatomico," *Rend Lincei*, vol. 3, pp. 145–149, 1926.

[50] P. Dirac, "On the theory of quantum mechanics," *Proceedings of the Royal Society of London A: Mathematical, Physical and Engineering Sciences*, vol. 112, no. 762, pp. 661–677, 1926.

[51] S. N. Bose, "Plancks Gesetz und Lichtquantenhypothese," *Zeitschrift für Physik*, vol. 26, pp. 178–181, 1924.

[52] S. L. Glashow, "Partial-symmetries of weak interactions," *Nuclear Physics*, vol. 22, no. 4, pp. 579 – 588, 1961.

[53] G. Altarelli, "The Standard model of particle physics," *CERN-PH-TH-2005-206*, 2005.

[54] P. Skands, "Introduction to QCD," in *Proceedings, 2nd Asia-Europe-Pacific School of High-Energy Physics (AEPSHEP 2014): Puri, India, November 04–17, 2014*, pp. 341–420, 2013.

[55] B. Andersson, G. Gustafson, and B. Söderberg, "A general model for jet fragmentation," *Zeitschrift für Physik C Particles and Fields*, vol. 20, pp. 317–329, Dec 1983.

[56] A. Ali, E. Pietarinen, and W. Stirling, "Transverse energy-energy correlations: A test of perturbative qcd for the proton-antiproton collider," *Physics Letters B*, vol. 141, no. 5, pp. 447 – 454, 1984.

[57] ATLAS Collaboration, "Determination of the strong coupling constant α_s from transverse energy–energy correlations in multijet events at $\sqrt{s} = 8$ TeV using the ATLAS detector," *Eur. Phys. J.*, vol. C77, no. 12, p. 872, 2017.

[58] G. Altarelli, "Partons in quantum chromodynamics," *Physics Reports*, vol. 81, no. 1, pp. 1 – 129, 1982.

[59] T. Regge, "Introduction to complex orbital momenta," *Il Nuovo Cimento (1955-1965)*, vol. 14, pp. 951–976, Dec 1959.

[60] P. Newman, *A Study of the Dynamics of Diffractive Photoproduction at HERA*. PhD thesis, University of Birmingham, 1996.

[61] P. D. B. Collins, *An Introduction to Regge Theory and High Energy Physics*. Cambridge Monographs on Mathematical Physics, Cambridge University Press, 1977.

[62] S. Donnachie, G. Dosch, P. Landshoff, and O. Nachtmann, *Pomeron Physics and QCD*. Cambridge Monographs on Particle Physics, Nuclear Physics and Cosmology, Cambridge University Press, 2002.

[63] W. Melnitchouk, R. Ent, and C. Keppel, "Quark-hadron duality in electron scattering," *Physics Reports*, vol. 406, no. 3, pp. 127 – 301, 2005.

[64] A. Donnachie and P. Landshoff, "Total cross sections," *Physics Letters B*, vol. 296, no. 1, pp. 227 – 232, 1992.

[65] Pierre Auger Collaboration, "The Pierre Auger Cosmic Ray Observatory," *Nucl. Instrum. Meth.*, vol. A798, pp. 172–213, 2015.

[66] TOTEM Collaboration, "First measurement of the total proton-proton cross-section at the LHC energy of $\sqrt{s} = 7$ TeV," *EPL (Europhysics Letters)*, vol. 96, no. 2, p. 21002, 2011.

[67] I. I. Pomeranchuk, "Equality of the nucleon and antinucleon total interaction cross section at high energies," *Zh. Eksp. Teor. Fiz.*, vol. 34, no. 3, pp. 725–728, 1958.

[68] A. Donnachie and P. Landshoff, "Elastic scattering and diffraction dissociation," *Nuclear Physics B*, vol. 244, no. 2, pp. 322 – 336, 1984.

[69] E. Levin, "An Introduction to pomerons," in *High energy physics. Proceedings, LAFEX International School, Session C, Workshop on Diffractive Physics, LISHEP'98, Rio de Janeiro, Brazil, February 16-20, 1998*, pp. 261–336, 1998.

[70] M. Froissart, "Asymptotic Behavior and Subtractions in the Mandelstam Representation," *Phys. Rev.*, vol. 123, pp. 1053–1057, Aug 1961.

[71] A. Martin, "Proceedings of the 1962 International Conference on High-Energy Physics at CERN," 4-11th July, 1962. Geneva: CERN: European Org. Nuc. Research., 1962.

[72] V. Mathieu, N. Kochelev, and V. Vento, "The Physics of Glueballs," *Int. J. Mod. Phys.*, vol. E18, pp. 1–49, 2009.

[73] ATLAS Collaboration, "Measurement of the total cross section from elastic scattering in pp collisions at $\sqrt{s} = 8$ TeV with the ATLAS detector," *Phys. Lett.*, vol. B761, pp. 158–178, 2016.

[74] P. Newman and M. Wing, "The Hadronic Final State at HERA," *Rev. Mod. Phys.*, vol. 86, no. 3, p. 1037, 2014.

[75] K. A. Goulianos, "Diffraction at the Tevatron in perspective," in *Diffraction 2002: Interpretation of the new diffractive phenomena in quantum chromodynamics and in the S matrix theory. Proceedings, NATO Advanced Research Workshop, Alushta, Ukraine, August 31-September 6, 2002*, pp. 13–21, 2003.

[76] ALICE Collaboration, "Measurement of inelastic, single- and double-diffraction cross sections in proton–proton collisions at the LHC with ALICE," *Eur. Phys. J. C*, vol. 73, p. 2456, 2013.

[77] D. Acosta *et al.*, "Inclusive double pomeron exchange at the Fermilab Tevatron $\bar{p}p$ collider," *Phys. Rev. Lett.*, vol. 93, p. 141601, 2004.

[78] ATLAS Collaboration, "Charged-particle distributions in pp interactions at $\sqrt{s} = 8$ TeV measured with the ATLAS detector," *Eur. Phys. J.*, vol. C76, no. 7, p. 403, 2016.

[79] A. M. Mueller, "O(2, 1) Analysis of Single-Particle Spectra at High Energy," *Phys. Rev. D*, vol. 2, pp. 2963–2968, dec 1970.

[80] A. B. Kaidalov, "Diffractive Production Mechanisms," *Phys. Rept.*, vol. 50, pp. 157–226, 1979.

[81] O. V. Kancheli, "Inelastic Differential Cross Sections at High energies and Duality," *JETP Lett.*, vol. 11, p. 267, 1970.

[82] Q.-D. Zhou, Y. Itow, H. Menjo, and T. Sako, "Monte Carlo study of particle production in diffractive proton–proton collisions at $\sqrt{s} = 13$ TeV with the very forward detector combined with central information," *The European Physical Journal C*, vol. 77, p. 212, Apr 2017.

[83] T. Sjostrand, S. Mrenna, and P. Z. Skands, "PYTHIA 6.4 Physics and Manual," *JHEP*, vol. 05, p. 026, 2006.

[84] T. Sjöstrand, S. Ask, J. R. Christiansen, R. Corke, N. Desai, P. Ilten, S. Mrenna, S. Prestel, C. O. Rasmussen, and P. Z. Skands, "An Introduction to PYTHIA 8.2," *Comput. Phys. Commun.*, vol. 191, pp. 159–177, 2015.

[85] A. Buckley *et al.*, "General-purpose event generators for LHC physics," *Phys. Rept.*, vol. 504, pp. 145–233, 2011.

[86] S. Navin, "Diffraction in Pythia," *arXiv:1005.3894*, 2010.

[87] T. Carli, "Measurement definitions based on truth particles." `https://indico.cern.ch/event/351610/contributions/826556/attachments/695528/955012/TruthParticleSessionSlides.pdf`. Accessed: 27/06/2018.

[88] S. Agostinelli *et al.*, "Geant4 - a simulation toolkit," *Nuclear Instruments and Methods in Physics Research Section A: Accelerators, Spectrometers, Detectors and Associated Equipment*, vol. 506, no. 3, pp. 250 – 303, 2003.

[89] G. Ingelman and P. Schlein, "Jet structure in high mass diffractive scattering," *Physics Letters B*, vol. 152, no. 3, pp. 256 – 260, 1985.

[90] T. Sjostrand, S. Mrenna, and P. Z. Skands, "A Brief Introduction to PYTHIA 8.1," *Comput. Phys. Commun.*, vol. 178, pp. 852–867, 2008.

[91] A. Aktas *et al.*, "Measurement and QCD analysis of the diffractive deep-inelastic scattering cross-section at HERA," *Eur. Phys. J.*, vol. C48, pp. 715–748, 2006.

[92] ATLAS Collaboration, "Rapidity gap cross sections measured with the ATLAS detector in pp collisions at $\sqrt{s} = 7$ TeV," *Eur. Phys. J.*, vol. C72, p. 1926, 2012.

[93] ATLAS Collaboration, "Dijet production in $\sqrt{s} = 7$ TeV pp collisions with large rapidity gaps at the ATLAS experiment," *Phys. Lett.*, vol. B754, pp. 214–234, 2016.

[94] CMS Collaboration, "Measurement of diffraction dissociation cross sections in pp collisions at $\sqrt{s} = 7$ TeV," *Phys. Rev.*, vol. D92, no. 1, p. 012003, 2015.

[95] ATLAS Collaboration, "Luminosity determination in pp collisions at $\sqrt{s} = 8$ TeV using the ATLAS detector at the LHC," *Eur. Phys. J. C*, vol. 76, p. 653. 71 p, Aug 2016.

[96] S. Cavalier, P. Puzo, H. Burkhardt, and P. Grafstrom, "90 m β^* Optics for ATLAS/ALFA," Tech. Rep. CERN-ATS-2011-134, Sep 2011.

[97] ATLAS Collaboration, "A study of the Pythia 8 description of ATLAS minimum bias measurements with the Donnachie-Landshoff diffractive model," Tech. Rep. ATL-PHYS-PUB-2016-017, CERN, Geneva, Aug 2016.

[98] ATLAS Collaboration, "Charged-particle distributions in $\sqrt{s} = 13$ TeV pp interactions measured with the ATLAS detector at the LHC," *Phys. Lett.*, vol. B758, pp. 67–88, 2016.

[99] ATLAS Collaboration, "Measurement of the Inelastic Proton-Proton Cross Section at $\sqrt{s} = 13$ TeV with the ATLAS Detector at the LHC," *Phys. Rev. Lett.*, vol. 117, no. 18, p. 182002, 2016.

[100] ATLAS Collaboration, "Charged-particle multiplicities in pp interactions measured with the ATLAS detector at the LHC," *New J. Phys.*, vol. 13, p. 053033, 2011.

[101] ATLAS Collaboration, "Measurements of the pseudorapidity dependence of the total transverse energy in proton-proton collisions at $\sqrt{s} = 7$ TeV with ATLAS," *JHEP*, vol. 11, p. 033, 2012.

[102] ATLAS Collaboration, "Measurement of the Inelastic Proton-Proton Cross-Section at $\sqrt{s} = 7$ TeV with the ATLAS Detector," *Nature Commun.*, vol. 2, p. 463, 2011.

[103] R. D. Ball *et al.*, "Parton distributions with LHC data," *Nucl. Phys.*, vol. B867, pp. 244–289, 2013.

[104] "Further ATLAS tunes of PYTHIA6 and Pythia 8," Tech. Rep. ATL-PHYS-PUB-2011-014, CERN, Geneva, Nov 2011.

[105] ATLAS Collaboration, "Measurements of underlying-event properties using neutral and charged particles in *pp* collisions at 900 GeV and 7 TeV with the ATLAS detector at the LHC," *Eur. Phys. J.*, vol. C71, p. 1636, 2011.

[106] ATLAS Collaboration, "Measurement of underlying event characteristics using charged particles in pp collisions at $\sqrt{s} = 900GeV$ and 7 TeV with the ATLAS detector," *Phys. Rev.*, vol. D83, p. 112001, 2011.

[107] A. D. Martin, W. J. Stirling, R. S. Thorne, and G. Watt, "Parton distributions for the LHC," *Eur. Phys. J.*, vol. C63, pp. 189–285, 2009.

[108] G. A. Schuler and T. Sjöstrand, "Hadronic diffractive cross sections and the rise of the total cross section," *Phys. Rev. D*, vol. 49, pp. 2257–2267, Mar 1994.

[109] G. D'Agostini, "A multidimensional unfolding method based on Bayes' theorem," *Nuclear Instruments and Methods in Physics Research Section A: Accelerators, Spectrometers, Detectors and Associated Equipment*, vol. 362, no. 2, pp. 487 – 498, 1995.

[110] T. Adye, "Unfolding algorithms and tests using RooUnfold," in *Proceedings, PHYSTAT 2011 Workshop on Statistical Issues Related to Discovery Claims in Search Experiments and Unfolding, CERN,Geneva, Switzerland 17-20 January 2011*, (Geneva), pp. 313–318, CERN, CERN, 2011.

[111] F. Abe *et al.*, "Measurement of $\bar{p}p$ single diffraction dissociation at $\sqrt{s} = 546$ GeV and 1800 GeV," *Phys. Rev.*, vol. D50, pp. 5535–5549, 1994.

[112] T. Affolder *et al.*, "Double diffraction dissociation at the Fermilab Tevatron collider," *Phys. Rev. Lett.*, vol. 87, p. 141802, 2001.

[113] F. J. Llanes-Estrada *et al.*, "QCD glueball Regge trajectory and the pomeron," *Nuclear Physics A*, vol. 710, no. 1, pp. 45 – 54, 2002.

[114] A. Ballon-Bayona, R. Carcassés Quevedo, M. S. Costa, and M. Djurić, "Soft Pomeron in Holographic QCD," *Phys. Rev.*, vol. D93, p. 035005, 2016.

[115] G. A. Jaroszkiewicz and P. V. Landshoff, "Model for Diffraction Excitation," *Phys. Rev. D*, vol. 10, pp. 170–174, Jul 1974.

[116] TOTEM Collaboration, "Soft diffraction and forward multiplicity measurements with TOTEM." `https://indico.cern.ch/event/267509/contributions/1605307/`. Accessed: 23/05/2018.

APPENDIX A

Additional Unfolding Plots

This appendix contains the plots concerning the unfolding procedure for each analysis variable, ξ_p, ξ_{EPz}, $\Delta\eta^F$ and $|t|$. Only the plots for ξ_p are included within the main body of this thesis (Section 9.1), so that they do not interrupt the main discussion of the analysis. Figure A.1 displays the fraction of reconstructed events that are classified as 'fakes'. Figure A.2 displays the fraction of events within the fiducial region that are classified as 'miss' events. Figure A.3 displays the purity for each bin as a function of the reconstructed level variable. Figure A.4 displays the fractional uncertainty in each bin for a range of iterations of the unfolding procedure. Figure A.5 displays the average uncertainty per bin as a function of the number of iterations of the unfolding procedure. Figure A.6 displays the uncertainty on the parameters extracted from fits as a function of the number of iterations of the unfolding procedure.

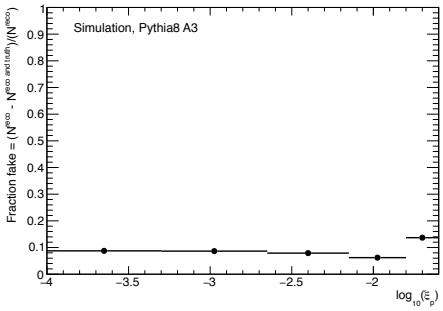

(a) Fake fraction for $\log_{10}(\xi_p)$

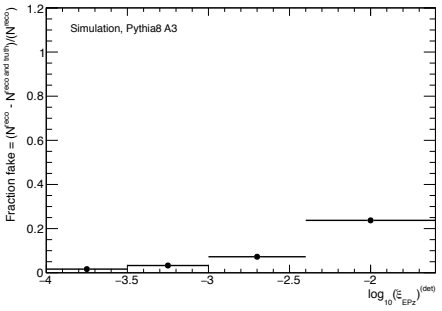

(b) Fake fraction for $\log_{10}(\xi_{EPz})$

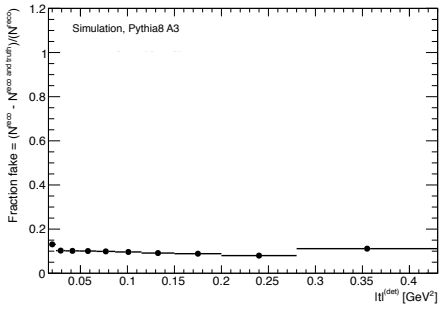

(c) Fake fraction for $|t|$

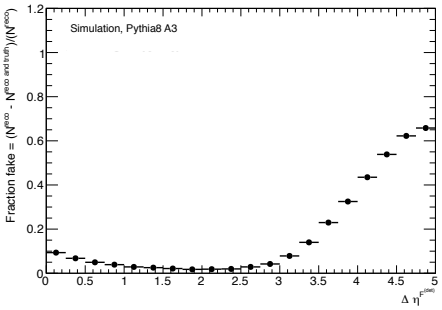

(d) Fake fraction for $\Delta\eta^F$

Figure A.1: Fraction of all events passing the reconstructed level event selection which lie outside of the fiducial region for all studied variables as a function of the truth value for all SD events in the MC. This quantity is referred to as 'fake events'. Statistical uncertainties are displayed.

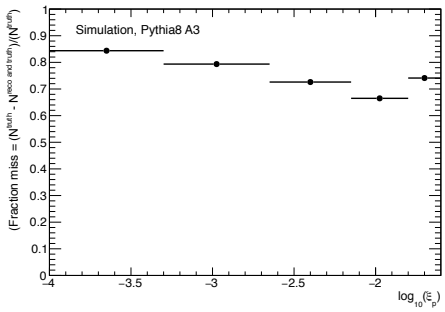

(a) Miss fraction for $\log_{10}(\xi_p)$

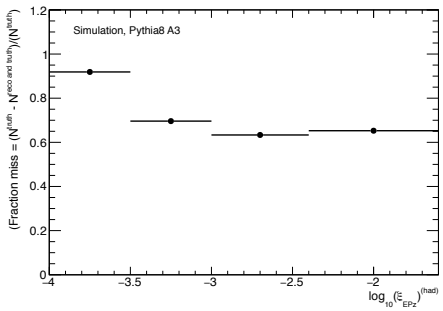

(b) Miss fraction for $\log_{10}(\xi_{EPz})$

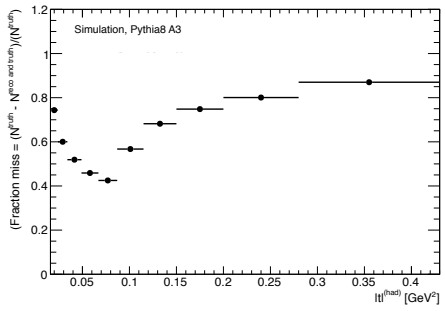

(c) Miss fraction for $|t|$

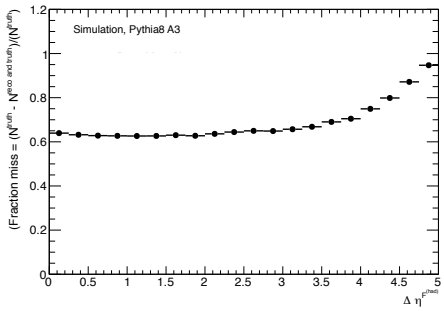

(d) Miss fraction for $\Delta\eta^F$

Figure A.2: Fraction of all events within the fiducial region that fail the reconstructed level event selection for all studied variables as a function of the truth value for SD events in the MC. This quality is referred to as 'miss events'. Statistical uncertainties are displayed.

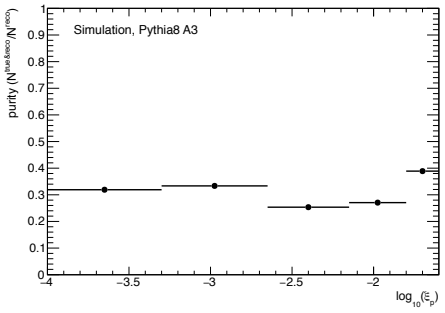

(a) Purity, $\log_{10}(\xi_p)$

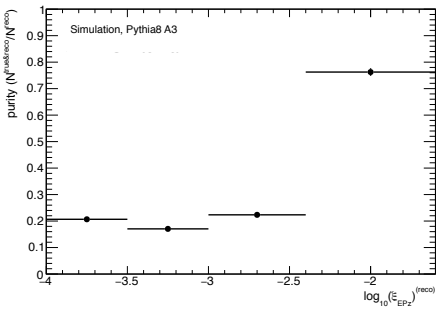

(b) Purity, $\log_{10}(\xi_{EPz})$

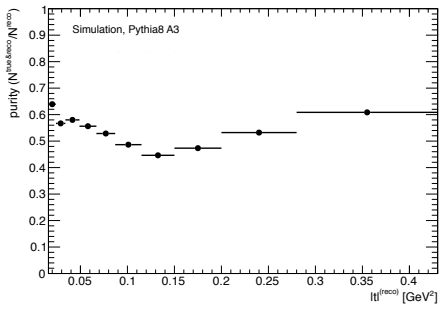

(c) Purity, $|t|$

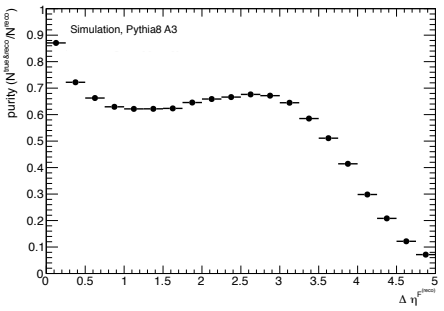

(d) Purity, $\Delta\eta^F$

Figure A.3: The fraction of all events in a specific bin at the reconstructed-level that are in the same bin at the truth-level, for SD events in MC. This quality is referred to as 'purity'. Statistical uncertainties are displayed.

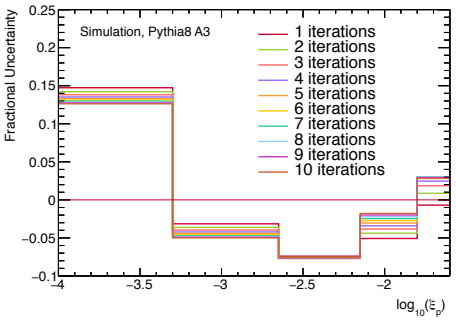

(a) $\log_{10}(\xi_p)$

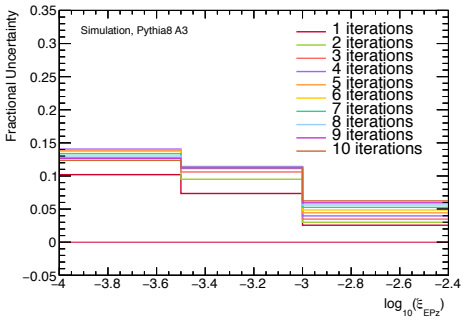

(b) $\log_{10}(\xi_{EPz})$

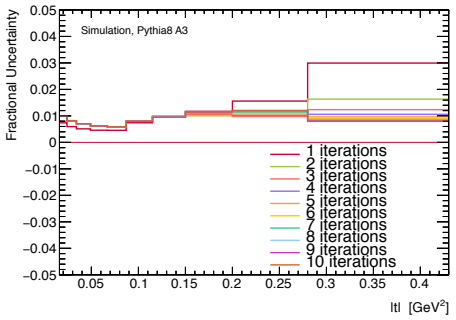

(c) $|t|$

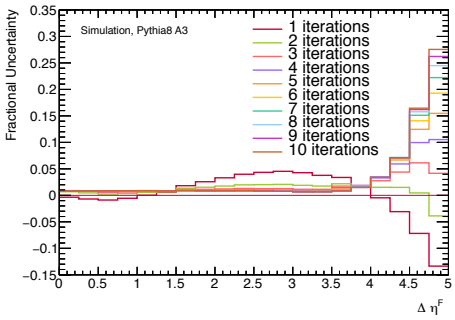

(d) $\Delta\eta^F$

Figure A.4: Fractional unfolding uncertainty as a function of all analysis variables. Results after one to ten iterations of the unfolding procedure are displayed.

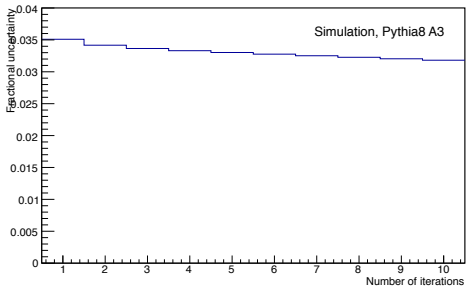

(a) $\log_{10}(\xi_p)$

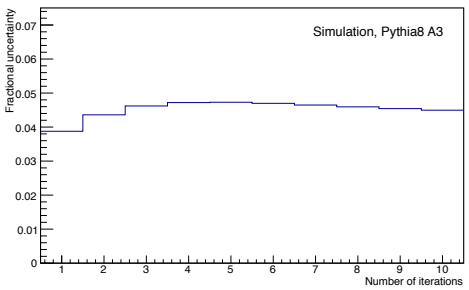

(b) $\log_{10}(\xi_{EPz})$

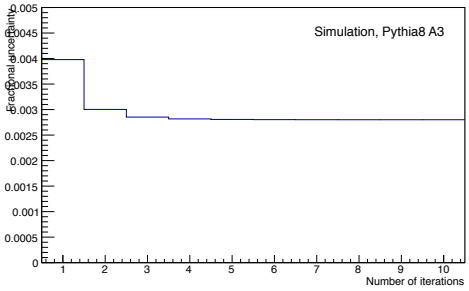

(c) $|t|$

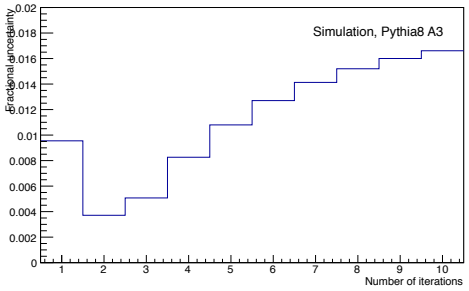

(d) $\Delta\eta^F$

Figure A.5: Mean uncertainty per bin as a function of number of iterations of the unfolding procedure.

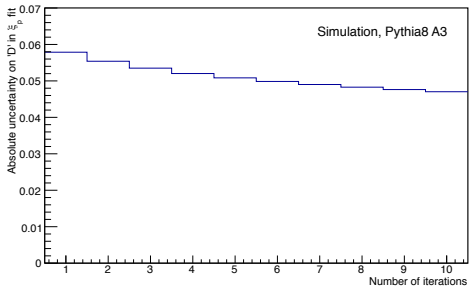

(a) 'D' parameter from $\log_{10}(\xi_p)$

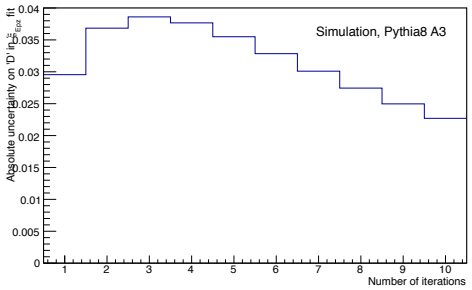

(b) 'D' parameter from $\log_{10}(\xi_{EPz})$

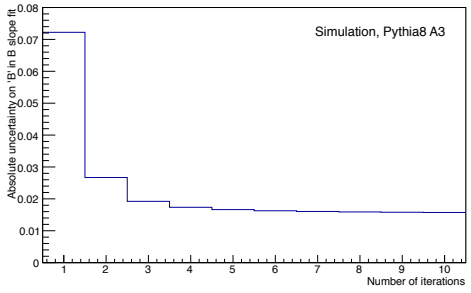

(c) B slope from $|t|$

Figure A.6: Uncertainty on the main fitted parameters as a function of number of iterations of the unfolding procedure.

APPENDIX B

Systematic Checks of Analysis

Several systematic checks were performed to test the stability of the results under variations in the analysis technique and event selection. The resulting extracted fit parameters, defined in Section 10, are compared to the nominal values. Parameters A, C and σ_{fid} pertain to the normalisation of the result while parameters B and D describe the shape of the results. The systematic checks performed are:

- The region of MBTS hit multiplicity in which at least 30 counters are above noise threshold is strongly dominated by background processes with very little signal. It is possible to remove a significant amount of the total background by removing this region from the analysis. This modified selection is applied and propagated through to all relevant aspects of the analysis. No significant deviations are observed from the nominal values, with no fitted parameter varying by more than 0.3σ and most typically varying by approximately 0.1σ. This selection is not applied in the main analysis selection as the MBTS multiplicity

is typically poorly modelled by MC, so it brings in an extra sensitivity to the distribution of charged particles that is unnecessary. The uncertainty on the background is not significantly reduced by applying this selection.

- Similarly to the MBTS hit multiplicity, it is possible to remove almost exclusively background events by requiring that the number of ID tracks detected is not above 35. With this change, no deviations from the nominal fitted values are observed at the 1σ level, however the normalisation is affected by approximately 0.6σ, and this is visible in several variables. This may be a symptom of the previously discussed mismodelling of the charged particle distributions in PYTHIA8, with either some signal events being removed unknowingly, or not enough background being modelled in this region. Thus, it is decided to maintain the current inclusive analysis with no upper selection on the track multiplicity in the ID.

- The lower MBTS multiplicity cut is varied to investigate the analysis' dependence on it. It is nominally applied at ≥ 5 MBTS counters above noise threshold to ensure at least 50% trigger efficiency. For the systematic check, this lower threshold is varied between three and seven counters. The trigger efficiency for three counter events is approximately 25% while it is approximately 90% for seven counter events (see Figure 7.1). No deviations are observed above 0.5σ in the $B, C_{\text{ALFA}}, C_{\text{ID}}, D_{\text{ALFA}}$ and D_{ID} variables, implying that the shapes of the distributions are fairly robust to this change. However, 1σ downwards deviations are observed in the normalisation variables, σ_{fid} and A, in the ≥ 7 MBTS selection. Tighter cuts, such as requiring ≥ 7 MBTS, are not preferred in this analysis as they reduce the inclusivity of the measurement and rely more on an accurate model of the hadronisation process.

- Nominally, at least six U-plane and six V-plane fibers in an ALFA Roman pot are required to be involved in track reconstruction for a track to pass the offline selection. This is varied to be four U-plane and four V-plane fibres to check that the analysis is not dependent upon this selection. This variation is propagated through the rest of the analysis, including the overlay background

rate and ALFA reconstruction efficiency calculations, neither of which vary significantly. It is observed that the normalisation is slightly reduced by this shift, displayed in the A, C and σ_{fid} parameters. However, none of these shifts are larger than 0.5σ, and the shifts to the B and D parameters are all $< 0.25\sigma$.

- The analysis is repeated separately for only A-side and only C-side tagged protons. Both versions of the analysis are consistent with the nominal analysis and this check provides good confidence that the location of the ALFA Roman Pots is well understood. The A and B fitted parameters are observed to vary by approximately 0.4σ in opposite directions about the nominal value, which is not of concern as the analysis is optimised for using both sides of the ALFA detector and thus the nominal measurement can be considered the average of these two single-sided configurations.

The nominal fit parameter value is compared to the altered value for each systematic variation, displayed in Table B.1. The only 1σ deviations stem from increasing the number of MBTS counters used in the analysis selection to identify the diffractive system. This variable is the most susceptible to variations in the distribution of charged particles, which is not well modelled. It is for this reason that the most inclusive selection was applied while maintaining at least 50% trigger efficiency.

Systematic check	A	B [GeV^{-2}]	C_{ALFA}	D_{ALFA}	C_{ID}	D_{ID}	σ_{fid}[mb]
Nominal values	2.65 ± 0.06	7.60 ± 0.31	2.6 ± 1.5	-0.13 ± 0.10	2.8 ± 0.2(stat.)	-0.12 ± 0.01(stat.)	1.59 ± 0.13
$N_{\text{MBTS}} < 30$	2.62	7.55	2.4	-0.14	2.7	-0.12	1.58
$N_{\text{ID tracks}} < 35$	2.60	7.50	2.4	-0.14	2.7	-0.12	1.55
$N_{\text{MBTS}} \geq 3$	2.64	7.61	2.6	-0.13	2.7	-0.12	1.59
$N_{\text{MBTS}} \geq 7$	2.56	7.66	2.5	-0.13	2.5	-0.12	1.46
$N_{\text{U \& V fibres in track}} \geq 4$	2.61	7.55	2.5	-0.13	2.6	-0.13	1.53
Proton tag (A-side)	2.67	7.71	2.6	-0.14	3.0	-0.11	1.62
Proton tag (C-side)	2.62	7.48	2.6	-0.12	2.6	-0.12	1.59

Table B.1: The shifts in all the fitted parameters and the fiducial cross section under all considered systematic checks. The first two rows display the nominal value of the parameters within the main analysis and the absolute uncertainty on them. The remaining rows display by how much each systematic shift varies them. The displayed uncertainties are the combination of the statistical and systematic uncertainties.